Optical and Electronic Studies of New Materials for Perovskite Multijunction Photovoltaics

Suhas Mahesh

Worcester College

A thesis submitted for the degree of
Doctor of Philosophy
at the University of Oxford

Michaelmas Term 2020

Acknowledgements

This thesis has its ultimate cause in a long succession of encouragements from family, friends and teachers stretching all the way back to grade school. This includes many whom I do not know, and who do not know me— such as the owner of Sunny Circulating Library, whose books piqued my interest in science at an early age. I remember each of them with gratitude. Special thanks are due to some teachers: Anand R, Ashok R, Dr. Maigur Raghavendra and Prof. G.K. Ananthasuresh.

I thank the Rhodes Trust for making my DPhil possible. The Rhodes House and the friends I made there will always have a special place in my heart.

I am deeply grateful to my supervisor Prof. Henry Snaith, FRS, for all his ideas, encouragement and support. It has been a privilege to have been moulded in the atmosphere of excellence that he has fostered. I am indebted in equal measure to that exemplar of order and efficiency, Clare Moloney, who not only magicked away countless bureaucratic tangles, but also provided an uncomplaining ear on many an occasion.

I am grateful to all the members of Snaith group, new and old. Maximilian Hörantner gave me some much-needed encouragement as I took my first wobbly steps. Though our paths only crossed for a few brief months, he did some crucial

cheerleading at a time when a terrified first year was feeling quite out of his depth. There was not a day when I did not hover at Pabitra Nayak's desk for his expert input on some matter or the other. I am grateful to him for the patient encouragement, the never-ending stream of ideas, and the vigorous discussions on solar cell physics. I am indebted to many others: Giulia Longo and Laura Schade for initiating me into the cult of double perovskites; Nobuya Sakai, Yen-Hung Lin, and David McMeekin for their godlike powers in the cleanroom; James Ball for his omnipotence; Bernard Wenger for his spectroscopic omniscience; Alex Ramadan for her all-seeing eye that keeps the cogs of the group whirring smoothly; Grey Christoforo for always having something useful to say; Mike Farrar for all the scientific discussions and worldly wisdom; Melissa McCarthy for the frequent lab rescue; and Robbie Oliver for his wizardry with wide bandgap solar cells. Lack of space forces me to only mention others by name: Harry Sansom, Jarla Thiesbrummel, Ashley Marshall, Elisabeth Duijnstee, Augustin Zaininger, Derek Hollman, Kelly Schutt, Spencer Case, Jonny Warby, Olivia Ashton, Jongchul Lim, Philippe Holzhey, Manuel Kober-Czerny, Benny Gallant, Ben Putland, Anna Jungbluth, Andreas Lauritzen, Yun Xiao, Suer Zhou and Sameer Kesava. It has been a pleasure and a privilege to work with this formidably talented bunch.

I have made some wonderful friends while at Oxford. I thank them all—Fellow Rhodies Rishika Sahgal, Bahuli Sharma, Rene Verma and Arijit Patra for the frequent jaunts to G&Ds; Prof. Diwakar Acharya, Prof. Harunaga Isaacson, Yiming

Shen, Pratik Rumde, Sasha Restifo, Gratius Avitus, and the Oxford Centre for Hindu Studies for the pleasant literary distractions; my frequent dinnertime companions Hala, Lakshmisha, Jineshvara, Bhoja, Abhinanda, Someshvara and Nilakantha; my wonderfully warm housemates at 17 Worcester Place—Tati, Zaiba, Julia, Jennifer and Rory; Sandhya Ranganathan and Keshava Shastry, visits to whom felt like home away from home.

Anusha has been with me every step of this journey and has always encouraged me to be the best version of myself. Words are too feeble a medium to adequately capture the debt this thesis owes to her. Jayashree aunty and Sudindra uncle have not only shown me unconditional affection, but also kept me motivated with shipments of homemade goodies. Finally, my heartfelt gratitude to my parents, my sister Chaitra, and my brother-in-law Deepak for all the sacrifices they have made for me over the years. Thank you for giving me the freedom of thought and the unstinting support to pursue my interests. This thesis is dedicated to all of them.

जह जह मणम्मि किज्जइ तह तह गरुएइ विम्हयं अम्ह ।
कव्वं व महाकइणो जं तं *विहि*-णिम्मियं* जयं जयइ ॥
[यथा यथा मनसि क्रियते तथा तथा गुरूकरोति विस्मयमस्माकम् ।
काव्यमिव महाकवेः यत् तद् *विधि*-निर्मितं जगज्जयति ॥]

आज्योतिर्गणमा च सर्षपकणात्सुष्ठु प्रतिष्ठापितं
स्रष्ट! र्विष्टपकाव्यमद्भुतमिदं व्याख्यानशून्यं स्थितम् ।
दुर्भिक्षं व्यपकर्तुमुद्यमवत ष्टीकामिमां कुर्वतः
तस्यैतन्मम सूत्रपातमधुना निर्विघ्नतः पालय ॥

सम्भुग्नपृष्ठतटमुत्कटभालरेख-
माकूणितेक्षणमुपेक्षितकुक्षिशोकम् ।
यैर्निश्चितार्थकमधीयत भौतशास्त्रं
तेभ्यः शिरः प्रणमयामि चिरन्तनेभ्यः ॥

विश्लिष्टेनापि तया मया यदल्पं व्यधायि बहुलं तत् ।
प्राभृतकमिदं तस्यै मद्धृदयैकानुशासिन्यै ॥

---

* ब्रह्मणा निर्मितम् । अथवा भौतिकशास्त्रगतैर्नियमैर्निर्मितम् ।

Contents

List of Figures

List of Tables

List of Publications

1. Schade, L.; Mahesh, S.; Volonakis, Y.; Zacharias, M.; Wenger, B.; Schmidt, F.; Kesava, S. V.; Dharmalingam, P.; Jalebi, M. A.; Lenz, M.; Giustino, F.; Longo, G.; Radaelli, P.; Snaith, H. J. **Crystallographic, Optical and Electronic Properties of Cs2AgBi1-XInxBr6 Double Perovskite and Understanding the Fundamental Photovoltaic Efficiency Challenges.** (under review)
2. Sansom, H. C.; Longo, G.; Wright, A. D.; Buizza, L. R. V.; Mahesh, S.; Zanella, M.; Abdi-Jalebi, M.; Pitcher, M. J.; Dyer, M. S.; Manning, T. D.; Friend, R. H.; Herz, L. M.; Snaith, H. J.; Claridge, J. B.; Rosseinsky, M. J. **Discovery of Stable Semiconductor Cu2AgBiI6 for Use on C-Si to Enable Lead-Free Tandem Photovoltaics with a Modelled Efficiency of 30.2%.** (under review)
3. Mahesh, S.; Case, S.; Snaith, H. J. Infrared Management in Perovskite-Perovskite Multi-junction Photovoltaics (in preparation)
4. Mahesh, S.; Wenger, B. **Multijunction Perovskite Solar Cells (Book Chapter)** In *Perovskite Photovoltaics* (in press); Wiley.
5. Longo, G.; Mahesh, S.; Buizza, L. R. V.; Wright, A. D.; Ramadan, A. J.; Abdi-Jalebi, M.; Nayak, P. K.; Herz, L. M.; Snaith, H. J. **Understanding the Performance-Limiting Factors of $Cs_2AgBiBr_6$ Double-Perovskite Solar Cells.** *ACS Energy Lett.* **2020**, 2200–2207. https://doi.org/10.1021/acsenergylett.0c01020.
6. Lin, Y.-H.; Sakai, N.; Da, P.; Wu, J.; Sansom, H. C.; Ramadan, A. J.; Mahesh, S.; Liu, J.; Oliver, R. D. J.; Lim, J.; Aspitarte, L.; Sharma, K.; Madhu, P. K.; Morales-Vilches, A. B.;

Nayak, P. K.; Bai, S.; Gao, F.; Grovenor, C. R. M.; Johnston, M. B.; Labram, J. G.; Durrant, J. R.; Ball, J. M.; Wenger, B.; Stannowski, B.; Snaith, H. J. **A Piperidinium Salt Stabilizes Efficient Metal-Halide Perovskite Solar Cells.** *Science (80-.).* **2020**, *369* (6499), 96–102. https://doi.org/10.1126/science.aba1628

7. Mahesh, S.; Ball, J. M.; Oliver, R. D. J.; McMeekin, D. P.; Nayak, P.; Johnston, M. B.; Snaith, H. **Revealing the Origin of Voltage Loss in Mixed-Halide Perovskite Solar Cells.** *Energy Environ. Sci.* **2019**, *50* (10), 675. https://doi.org/10.1039/C9EE02162K.
8. Nayak, P. K.; Mahesh, S.; Snaith, H. J.; Cahen, D. **Photovoltaic Solar Cell Technologies: Analysing the State of the Art**. *Nat. Rev. Mater.* **2019**, *4* (4), 269–285. https://doi.org/10.1038/s41578-019-0097-0.
9. McMeekin, D. P.; Mahesh, S.; Noel, N. K.; Klug, M. T.; Lim, J.; Warby, J. H.; Ball, J. M.; Herz, L. M.; Johnston, M. B.; Snaith, H. J. **Solution-Processed All-Perovskite Multi-Junction Solar Cells.** *Joule* **2019**, *3* (2), 387–401. https://doi.org/10.1016/j.joule.2019.01.007.
10. Lim, J.; Hörantner, M. T.; Sakai, N.; Ball, J. M.; Mahesh, S.; Noel, N. K.; Lin, Y. H.; Patel, J. B.; McMeekin, D. P.; Johnston, M. B.; Wenger, B.; Snaith, H. J. **Elucidating the Long-Range Charge Carrier Mobility in Metal Halide Perovskite Thin Films**. *Energy Environ. Sci.* **2019**, *12* (1), 169–176. https://doi.org/10.1039/c8ee03395a.
11. Tainter, G. D.; Hörantner, M. T.; Pazos-Outón, L. M.; Lamboll, R. D.; Āboliņš, H.; Leijtens, T.; Mahesh, S.; Friend, R. H.; Snaith, H. J.; Joyce, H. J.; Deschler, F. **Long-Range Charge Extraction in Back-Contact Perovskite Architectures via**

Suppressed Recombination. *Joule* **2019**, *3* (5), 1301–1313. https://doi.org/10.1016/j.joule.2019.03.010.

12. Alsari, M.; Bikondoa, O.; Bishop, J.; Abdi-Jalebi, M.; Ozer, L. Y.; Hampton, M.; Thompson, P.; Hörantner, M. T.; Mahesh, S.; Greenland, C.; Macdonald, J. E.; Palmisano, G.; Snaith, H. J.; Lidzey, D. G.; Stranks, S. D.; Friend, R. H.; Lilliu, S. **In Situ Simultaneous Photovoltaic and Structural Evolution of Perovskite Solar Cells during Film Formation**. *Energy Environ. Sci.* **2018**, *11* (2), 383–393. https://doi.org/10.1039/c7ee03013d.

List of Patents

Snaith, H. J and Mahesh, S. **Multi-Junction Optoelectronic Device Comprising Device Interlayer**, International Application Number: PCT/GB2019/053550. International Filing Date: 13/12/2019

List of Abbreviations

AM	Atmospheric mass
ARC	Anti-reflection coating
AZO	Aluminium-doped zinc oxide
CBM	Conduction band maximum
CPD	Contact potential difference
EQE	External quantum efficiency
EQE_{EL}	Electroluminescence quantum efficiency
EQE_{PV}	Photovoltaic external quantum efficiency
ESB	Energy selective backscattering
FA	Formamidinium
FF	Fill-factor
FTO	Fluorine-doped tin oxide
FTPS	Fourier transform photocurrent spectroscopy
HIT	Heterojunction with intrinsic thin layer
IBC	Interdigitated Back-contact
IEC	International Electrotechnical Commission
ITO	Indium tin oxide
LCOE	Levelized cost of energy
MA	Methylammonium
NIR	Near infrared
NREL	National Renewable Energy Lab
OPTP	Optical-pump terhertz-probe
OPV	Organic photovoltaics
PCE	Power conversion efficiency
PDS	Photothermal deflection spectroscopy

PERC Passivated emitter and rear contact

PID Potential induced degradation

PL Photoluminesence

PLE Photoluminescence excitation

PLQE Photoluminescence quantum efficiency

PLQY Photoluminescence quantum yield

PV Photovoltaic

PVK Perovskite

QD Quantum dot

SEM Scanning electron microscopy

SHJ Silicon heterojunction

SPV Surface Photovoltage

SQ Shockley-Queisser

SRH Shockley-Read-Hall

TCO Transparent conducting oxide

TMM Transfer matrix method

UPS Ultraviolet photoelectron spectroscopy

UV Ultraviolet

VBM Valence band minimum

XRD X-Ray Diffraction

1

Photovoltaics: A Brief History

1.1 Overview

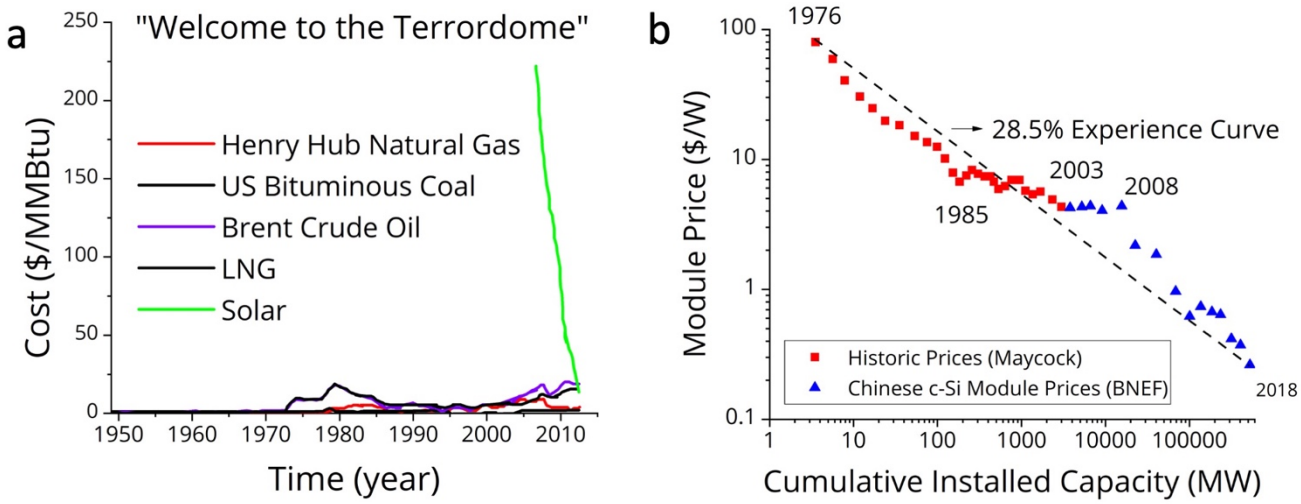

Figure 1.1 | a) The contrasting fortunes of fossil fuels and PV. The y-axis is the cost of energy in USD per million British thermal units. (Adapted from AllianceBernstein[6]) **b)** c-Si PV has a shown a record learning rate: the cost per Watt has dropped by 28.5% for every doubling in cumulative installed capacity. (Adapted from Bloomberg NEF.)

This introductory chapter summarises the history of photovoltaics over the last two centuries, providing context about the ups and downs of the market and the industry in which perovskite multi-junction photovoltaics is out to succeed.

1.2 Introduction

No conference on renewable energy is complete without a speaker noting that about ninety minutes worth of sunlight is enough to fuel mankind's energy consumption for a whole year. With rising standards of living projected to cause a 50% increase in energy consumption by 2050[1], this clean source of power can only be expected to become more and more relevant in coming decades. In its 2019 report, the authoritative global network REN 21 (Renewable Energy Policy Network for the 21st Century) stated that a fourth of the world's electricity was generated from renewables[2]. In the United Kingdom, zero-carbon electricity had a share close to 50%[3]. The same year, renewables received a quarter trillion dollars in investment every year, far exceeding fossil fuel investment[4]. This surge in financing is telling—for over a decade now, renewables have broken away from being subsidy-dependent exploratory technologies and are now firmly entrenched in the mainstream. The price of PV electricity has hit an all-time low of ~30$/MWh and is only expected to drop further[5]. (Adapted from Bloomberg NEF.) The impact of this freefall on the fossil fuel industry is perhaps best demonstrated by AllianceBernstein's famous "Welcome to the Terrordome" plot[6], an adapted version of which is presented in Figure 1.1 (a). The graph is named after a popular rap song from the 90s, and alludes to the sheer terror that a fossil fuel executive should feel upon encountering this graph. It is also no comfort to

them that PV installations can scale by orders of magnitude. The potential solar resource is gigantic—over 90,000 terawatts, and the power available in wind is less than one percent of this. Despite this abundance, solar energy is a much lower density energy resource. Roughly the surface area of Spain or California is required to provide all of humanity's energy needs through 20% efficiency solar panels, assuming an irradiance of 6 kWh/m^2, which is roughly the power incident on southwestern United States[7]. Furthermore, there is significant spatial and temporal variation in the solar resource. However, neither of these are insurmountable barriers to PV adoption. Ultimately, it is the levelized cost of energy (LCOE) from a PV plant that determines its success in the energy market. As cost advantages associated with scale-up have led to a steady decline in the price of c-Si modules. For every doubling in the cumulative installed capacity, the price per watt has dropped by 28.5% (Fig. 1.1 (b)). This trajectory, however, will not continue forever. For Si PV, the phase of diminishing returns is already kicking in. For a step change in the LCOE, an increase in efficiency is necessary, as it slashes a number of costs at once—land acquisition, balance of system, and maintenance. As the next chapter argues, the development of perovskite-based multi-junctions offers the opportunity to raise efficiencies beyond 30%, effecting a major drop in the LCOE, which in turn, will enable multi-terawatt scale PV installations.

This introductory chapter summarises the history of PV over the last two centuries, providing context about the market and the industry in which

perovskite multi-junction photovoltaics is out to succeed. For a technical overview of prevailing PV technologies, the interested reader is directed towards our publication *Photovoltaic solar cell technologies: analysing the state of the art*[8], the contents of which have not been included in this thesis.

1.3 The Spark

Photovoltaics, like many revolutionary technologies, ultimately traces back to serendipity. Willoughby Smith noted in the late 1860s that selenium bars used in transatlantic cable testing performed abysmally in daylight, though they were perfectly functional at night. Some clever experiments led to his 1873 article in the *Journal of the Society of Telegraph Engineers*[9], which sparked tremendous interest across Europe. The link between sunlight and electricity was quickly established, and the term photoelectric coined. James Clerk Maxwell wrote in an 1874 letter to a friend[10]: "I saw conductivity of Selenium as affected by light. It is most sudden. Effect of a copper heater insensible. That of the sun great." On the other side of the Atlantic, Charles Fritts slapped a thin layer of selenium on a metal plate and covered it with semi-transparent gold-leaf film. This was the world's first solar module, already operational in 1884, and sat installed on a New York rooftop[11]. The mechanism of operation, however, puzzled even leading scientists like Maxwell and Siemens. In fact, it would take a century more to provide a mature thermodynamic underpinning to photovoltaics. The first breakthrough came in

1905. One of Einstein's *annus mirabilis* papers introduced the concept of quantized light that successfully explained the intriguing experimental observations of the photoelectric effect[12]. The legitimacy conferred by Einstein's theoretical explanation encouraged further research, and by the 1930s, dreams of a world powered by the sun had entered the public imagination, as evinced by books and magazine articles from the era. "Sooner or later," said an article in *Popular Mechanics*[13], "we shall have to go directly to the sun for our major supply of power." Westinghouse's photoelectric division concluded more soberly[14]: "The photovoltaic cells will not prove interesting to the practical engineer until the efficiency has increased at least fifty times." Both assertions of wild optimism and woebegone pessimism are littered throughout the pages of photovoltaic history. However, Westinghouse had made the correct assessment for his age; the efficiencies were still impractically low—below half a percent.

1.4 Silicon Revolution and the Space Race

The silicon revolution in the 1950s spawned the first truly practical solar cells. As most things semiconductor, this too happened at Bell Laboratories. In 1953, Bell Labs had Daryl Chapin investigate alternative sources of power for remote humid environments, where dry-cell batteries were prone to degradation. Within a year, Chapin drew upon Bell Lab's research into silicon to make a silicon-based solar cell with an unprecedented conversion efficiency of 6%[15]. As Chapin put it,

these were the first photovoltaic cells "intended to be primary power sources."[16] A 21-inch Ferris wheel powered by these cells was exhibited to fawning press reporters, once again sparking public excitement about a solar future[17]. Commercial applications, however, were still a far dream. In the 1950s, the average home-owner would have had to pay millions of dollars to power their house from solar arrays. The Bell photovoltaic cell found its first application in a top secret program of the US government, where cost was no bar—the development of artificial satellites. Battery powered satellites would only work for weeks before they fell silent. In 1958, Vanguard blasted off with six tiny solar panels. The paltry half a watt was enough to beam back data about atmospheric composition for six whole years[18]. With this success, the PV module became the *sine qua non* of satellite technology for both Americans and the Soviets. The arrival of low-power silicon transistors made PV even more attractive. The space race and the silicon revolution had together transformed photovoltaics from an expensive curiosity to a successful commercial enterprise for space applications.

1.5 Early Terrestrial Beginnings

While PV established itself in space fairly early on, solar cells were still too expensive and inefficient to compete with fossil fuels for terrestrial employment. PV took its first terrestrial steps in remote locations where conventional electrical lines could not reach. With the development of silicon transistors, power

consumption was also continually dropping, making this a viable proposition. The first enthusiastic customers, curiously enough, turned out to be oil and gas companies. Exxon was one of the earliest adopters. In the 1970s, they shifted to PV to run the round-the-clock navigational warning systems of their oil platforms in the gulf of Mexico[19]. The expense was offset by the reduced effort and cost of tending to the bulky, expensive and toxic batteries. Within a decade, PV had become extremely popular for powering oil rigs, buoys, lighthouses, well heads and pipelines. Communications become another popular market. Repeaters, which used to pick up and rebroadcast electromagnetic waves, were often a perfect fit for PV owing to their remote and hazardous locations. In the 1970s, Telecom Australia was tremendously successful at providing telephone service to remote locations by pairing a telephone and a transmitter with a solar module.

Starting from the late 1970s, PV attracted the attention of experts seeking to bring the developing world up to the same level of electrification as the developing world[20]. Distributed energy production was seen as a less costly option. With oil production starting to fall by the 1970s, diesel generators in every household were made impractical. Skilled mechanics to maintain such generators were also scarce. Sunlight, however, shines impartially and PV cells, being solid state devices, required little maintenance. There was also the incidental advantage that most developing populations inhabited sunny climes. The first solar powered homes were built in French Polynesia in the late 1970s, funded by the French

Atomic Energy Commission[20]. Amongst the offerings was a 400 Watt module that could power the essential elements of a household. The total cost of the appliances and the PV system came to around ten thousand dollars, the PV modules being the most expensive element. Similar attempts were made in other developing countries— Kenya, India, China, Vietnam, Dominican Republic and more. While they succeeded in bringing electricity to communities for the first time, the quantity and reliability still fell short of conventional grids.

So far, PV was succeeding in those arenas where fossil fuels could not compete. However, it was still too inefficient and expensive to be competitive as a mainstream energy source. Furthermore, the years following the second world war had seen a boom in the production of oil and gas. This glut of energy left PV with little manoeuvring room. The policies of the US government showered billions on "Atoms for Peace," leaving PV development with only scraps. A Nixon era report titled *The Nation's Energy Future* proposed $4 billion for nuclear energy, and doled out a paltry $36 million for solar cells[20]. Through this era, the public eye too was hypnotised by nuclear energy as the energy of the future. As Martin Green has explained: "The commercial industry was not vibrant during the 1980s. A lot of the firms were oil companies doing greenwashing, and just trying not to lose too much money from solar."[21] Nevertheless, as PV efficiencies slowly crept up, and scales of manufacturing increased, the cost of PV electricity was dropping many orders of magnitude— from thousands of dollars per watt in the late 1950s

to $100 a watt by the mid 1970s, eventually reaching today's price of 0.5$/watt. The decline continues—for every doubling in total world solar panel installations, the cost has reliably dropped by twenty percent ("the learning curve"), sometimes called "Swanson's Law" after the founder of the American PV company SunPower.

1.6 Mainstream Entry: The Last Two Decades

With prices dropping, the late 1980s saw interest in solar panels as a source of mainstream power. There were two models of energy production. The first copied the fossil fuels—large solar farms that would export electricity to communities. Others backed an on-site approach with grid integration, saying that centralisation wasted the distributed solar resource. The first revolutionary steps in proving the on-site concept were taken by a Swiss company, Alpha Real[22]. In the late 1980s, they installed a full MW of PV on 333 Swiss domestic rooftops, with complete integration into the regular grid. Consumers could buy electricity from the grid when the generation was down. More interestingly, it introduced the concept of selling to the utility when the panels were over-generating. Not only was this system attractive financially, it also eliminated the need for buying and maintaining batteries. Alpha Real's idea was revolutionary for photovoltaic installations. Consumers loved the idea of reverse billing the utility company. In 1993, Sacramento's municipal utility replicated Alpha Real's work at the scale of two megawatts. But successive snubs to PV by the Carter and Reagan

administrations disrupted the dominance of the United States. The United States has never since regained dominance in PV research, manufacturing, or installation. The baton passed to Japan who offered generous subsidies and installed a gigawatt of grid-connected roof-top solar panels between 1994-2002[22]. Germany enacted a very successful law that required utilities to purchase back electricity from small consumers at €0.50/kWh[22]. This early confidence in PV became a self-fulfilling prophecy, eventually driving up production and driving down costs to the point that the same subsidies were no longer needed.

1.7 Boom and Bust (2005-2008)

Expert opinion about the future of solar has vacillated widely over the last century. Charles Fritts, one of the early pioneers in the 19th century, was optimistic— "We may ere long see the photoelectric plate competing with [coal-fired electrical-generating plants]."[11] But after even a century, progress was still crawling, leading a frustrated MIT solar pioneer Hoyt Hoyle to remark: "The present 'unreserved enthusiasm' about solar energy may be remembered as a period of midsummer madness brought on by the sun."[23] Nevertheless, progress was slow, but steady. By the early 2000s, decades of research had resulted in extremely reliable c-Si modules with lifetimes of 25+ years. Mass-produced module efficiencies had hit 15%, and were inching towards 20%. PV based on c-Si was technologically mature, and ready to be the workhorse of decarbonised

electricity. The market competition and improved confidence from banks, particularly in China, resulted in the price of PV electricity becoming competitive with other sources of energy. By the mid 2000s, prices had fallen to $4/W, making it clear that a switch to PV as a source of electricity was feasible[24].

PV's biggest turning point came in 2005, when Germany set up a fixed "feed-in-tariff" of at least 457 euros/MWh for PV electricity, with no limits. "Feed-in-tariff" refers to 20 years of assured payment for every kWh of energy generated and fed back into the grid. This assured steady return incentivised investors and consumers to finance the large upfront cost. Germany suddenly found itself with a voracious appetite for PV. In a rush, several companies like SolarWorld, SunPower, Energy Conversion devices, Q-Cells, Suntech, REC, Wacker-Chemie completed Initial Public Offerings (IPOs) on stock markets. This surge included thin-film solar cell companies in large numbers. Companies like Trina and Suntech built new factories to respond to the upsurge. China mushroomed countless small-scale module manufacturers. The production volumes grew so large that PV companies started producing their own raw material, polysilicon, slashing costs even further. When the sun was shining right, Germany was able to generate half its electricity from PV. China too offered vigorous support for manufacturing. More players joined the game, and the bubble grew larger. Supply was now outstripping demand. In fact, the industry was being propped up by subsidies and artificially high polysilicon prices.

The stock market crash of 29 September 2008 precipitated the bust. Large volumes of solar cells being produced suddenly had no takers. A great many PV companies folded over the next few years: Suntech, Solyndra, Hanergy, SunEdison. Some of these, like Hanergy, were later found embroiled in murky transactions and unethical fundraising. Dreams of thin-film PV succeeded c-Si were cut short. Investors lost billions, engendering a financial caution towards PV that lingers to this day. The battered German PV collapsed, never to recover again. The baton was taken up by China, which now enjoys an unchallenged monopoly over the production of PV modules.

1.8 Today and Tomorrow

Since 2015, the PV industry has found new equilibrium, and it is now ground reality in some countries that PV is the cheapest way of producing energy. In such countries, PV is a serious competitor in energy auctions where it stands shoulder to shoulder with wind, hydro, and fossil fuels. In August 2020, Portugal's second solar auction drew a record low bid of $13.12/MWh[25]. International Energy Agency's (IEA) prediction that PV will be the largest contributor to the world's electricity by 2050 (with 4.7 terawatts installed) is no longer met with laughter[26]. After all, annual PV installations have consistently overperformed the predictions of pundits for at least two decades. PV installations will continue to boom in regions like India, Latin America and China, which have excellent sunshine and

growing energy demand. On the technology front, the performance of c-Si continues to improve. Manufacturers are slowly shifting from the PERC architecture to the superior HIT architecture which offers higher open-circuit voltages. Bifacial modules, which generate more power by absorbing light incident on both sides, are likely to become standard features of PV farms. PV will also transform the way our power bills are structured. Utilities will bill consumers not just by power consumed, but also by the time of the day, depending on solar and wind production. Grids will made smarter to interface with time-varying sources and sinks. You may be offered a discount for permission to decide when your IoT air conditioner turns on, or your electric car recharges.

1.9 Next Generation PV

For PV researchers, the temptation to paint PV as a panacea for decarbonisation is strong. However, it is vital to remember that only 18% of the world energy usage is currently electric. Only this “shallow” decarbonisation falls within the ambit of current wind and PV technology. The other 82%—heating and transport—pose a far greater challenge (“deep” decarbonisation). If PV has to be the engine of a new decarbonised economy, these two sectors must be electrified with urgency. Ultimately, the cost of energy will be the incentive for such electrification. By making PV significantly cheaper than fossil fuels, new factories and infrastructure can be made to gravitate towards electric power. PV efficiency

is now well-known to be the biggest determinant of cost. Increasing PV efficiency slashes a number of costs at once— land acquisition, maintenance, and balance of systems. Thus, “deep” decarbonisation demands the development of high efficiency next-generation PV technology. While many candidate technologies have been proposed, the multijunction solar cell is the only one that holds commercial promise. Multi-junction PV has been around since 1979, when two epitaxially grown AlGaAs/GaAs junctions were interconnected with an epitaxially grown tunnel junction. While multi-junction technology has been deployed on space-missions since the mid-1990s, the prohibitive cost of epitaxial growth has prevented mass production. The fortuitous discovery of hybrid perovskites now opens up the possibility of mass producing such multijunction solar cells with power conversion efficiencies exceeding 30%. The next chapter explores this theme in some detail.

1.10 Aims of this Thesis

The central aim of this thesis is to understand the electronic and optical loss mechanisms peculiar to perovskite multijunction PV, and present strategies that will enable the 30% power conversion efficiency barrier to be broken.

Chapter 2 provides a detailed overview of perovskite multi-junction photovoltaics. The theory behind multijunction PV, the current state of the field, and the challenges that this thesis aims to resolve are contextualised here.

Chapter 3 provides a brief explanation of some important theoretical concepts that are frequently used in this thesis. This includes an explanation of detailed balance as applied to solar cells, and the transfer matrix method for modelling the optics of solar cells. An undergraduate understanding of semiconductor physics is assumed.

Chapter 4 explains the nitty-gritties of the experiments and modelling presented in chapters that follow.

Chapter 5 demystifies the origin of open-circuit voltage loss in wide-bandgap mixed-halide perovskite PV. Our results indicate that, contrary to popular belief, halide segregation is not the dominant loss mechanism in Br-rich wide bandgap cells. Rather, the loss is dominated by the relatively low initial radiative efficiency of the cells, which arises from both imperfections within the absorber layer, and at the perovskite/charge extraction layer heterojunctions. We thus identify that focusing on maximising the initial radiative efficiency of the mixed-halide films and devices is more important than attempting to suppress halide segregation.

Chapter 6 reveals a hitherto unknown loss mechanism in $Cs_2AgBiBr_6$ based wide bandgap solar cells. The success of perovskite multi-junction PV—particularly of triple junctions and beyond—hinges on the development of such high-quality high-bandgap absorbers. This work combines experiment modelling studies to reveal that short electron diffusion length underpins the limited performance of $Cs_2AgBiBr_6$ solar cells.

Chapter 7 brings to light a hitherto uninvestigated optical loss mechanism in perovskite-perovskite multi-junction PV. We identify that the most commonly used recombination layer, Indium tin oxide, has the unintended consequence of causing a severe refractive index mismatch, resulting in reduced photon conversion external quantum efficiency (EQE) in the near infrared. We perform optical simulations to quantify this loss, and propose a new refractive index matched interlayer that can increase PCE by up to 1% absolute.

Chapter 8 summarises the results presented in this thesis.

1.11 References

1. U.S. Energy Information Administration. *International Energy Outlook 2020*. https://www.eia.gov/outlooks/ieo/pdf/ieo2020.pdf (2020).
2. REN21. RENEWABLES 2019 GLOBAL STATUS REPORT. https://www.ren21.net/gsr-2019/ (2019).
3. National Grid. Britain hits historic clean energy milestone as zero carbon electricity outstrips fossil fuels in 2019. https://www.nationalgrid.com/britain-hits-historic-clean-energy-milestone-zero-carbon-electricity-outstrips-fossil-fuels-2019.
4. World Economic Forum. This is how much was invested in clean energy in 2019. https://www.weforum.org/agenda/2020/06/global-clean-energy-investment-research/ (2020).

5. Lazard. Levelized Cost of Energy and Levelized Cost of Storage 2019. https://www.lazard.com/perspective/lcoe2019/ (2019).

6. Bernstein Research. *Bernstein Energy and Power Blast: Equal and Opposite…If Solar Wins, Who Loses?* https://reneweconomy.com.au/wp-content/uploads/2014/04/Bernstein-solar.pdf (2014).

7. National Renewable Energy Laboratory. Solar Resource Data, Tools, and Maps. https://www.nrel.gov/gis/ solar.html. (2020).

8. Nayak, P. K., Mahesh, S., Snaith, H. J. & Cahen, D. Photovoltaic solar cell technologies: analysing the state of the art. *Nat. Rev. Mater.* **4**, 269–285 (2019).

9. Smith, W. The Action of Light on Selenium. *J. Soc. Telegr. Eng. 2* 32 (1873).

10. James Clerk Maxwell to Peter Guthrie Tate, letter, late April 1874. in *The Scientific Letters and Papers of James Clerk Maxwell (Vol. 3)* 67 (Cambridge University Press, 1995).

11. von Siemens, W. On the Electromotive Action of Illuminated Selenium Discovered by Mr. Fritts of New York. *Van Nostrand's Engineering Magazine 32 (1885)* 392.

12. Einstein, A. Concerning an Heuristic Point of View Toward the Emission and Transformation of Light. *Ann. Phys.* **17**, 132–148 (1905).

13. Coblentz, W. W. Electricity: Scientists Predict New Era of Power Produced Directly from Light. *Popular Mechanics* 418–421 (1932).

14. Wilson, E. D. Power from the Sun. *Power 28* 517 (1935).

15. Martin, D. Daryl Chapin, 88, A Co-Developer Of Solar Energy Cell. *The New York Times* 33 (1995).

16. Perlin, J. From Selenium to Silicon. in *Let It Shine* 313 (New World Library, 2013).

17. Perlin, J. The Invention Of The Solar Cell. *Popular Science* https://www.popsci.com/article/science/invention-solar-cell/ (2014).

18. National Aeronautics and Space Administration. Vanguard 1. https://nssdc.gsfc.nasa.gov/nmc/spacecraft/display.action?id=1958-002B.

19. Hsu, A. How Big Oil Of The Past Helped Launch The Solar Industry Of Today. *NPR* https://www.npr.org/2019/09/30/763844598/how-big-oil-of-the-past-helped-launch-the-solar-industry-of-today?t=1599838580235 (2019).

20. Perlin, J. The First Large-Scale Photovoltaic Applications on Earth. in *Let It Shine* 327–338 (New World Library, 2013).

21. Chase, J. The Magic of the Experience Curve. in *Solar Power Finance Without the Jargon* 47 (World Scientific, 2019).

22. Perlin, J. Photovoltaics for the World. in *Let It Shine* 408–413 (2013).

23. Faltermayer, E. Solar Energy Is Here, But It's Not Yet Utopia. *Fortune* **93**, 68 (1976).

24. Bloomberg NEF & The Business Council for Sustainable Energy. *2019 Sustainable Energy in America Factbook*. (2019).

25. Scully, J. ‘Historic’ result as Portugal claims record-low prices in 700MW solar auction. *PVTECH* https://www.pv-tech.org/news/historic-result-as-portugal-claims-record-low-prices-in-700mw-solar-auction (2020).

26. International Energy Agency. *Technology Roadmap: Solar Photovoltaic Energy*. https://www.webcitation.org/6T92GIRhW?url=http://www.iea.org/publications/freepublications/publication/TechnologyRoadmapSolarPhotovoltaicEnergy_2014edition.pdf (2014).

2

Multijunction Perovskite Photovoltaics

2.1 Overview

This chapter reviews developments in perovskite multi-junction photovoltaics, providing the context which makes the results presented in this thesis relevant. The theory behind multi-junctions is explained, the state of progress in perovskite-silicon and perovskite-perovskite multi-junctions is individually reviewed, and issues that currently limit performance are elucidated. We do not discuss the fundamentals of semiconductor theory and single-junction perovskites cells here, as it is assumed that most readers would be specialised, and already conversant with these topics.

2.2 Perovskite for Photovoltaics

A perovskite is a compound with the structure ABX_3. Lead halide perovskites are a subset of this class of materials. The cation B is lead in the 2+ oxidation state,

and the anion X is a halide, usually iodide, bromide or chloride. The cation A can be Cs^+, methylammonium (MA^+), or formamidinium (FA^+). In all, the structure comprises of corner sharing octahedra of $[PbX_6]^{4-}$, and the cation A filling the spaces between. David Mitzi pioneered extensive research on the semiconducting and opto-electronic properties of organic-inorganic perovskites in the early 1990s[1]. In the late 2000s, the perovskite $CH_3NH_3PbI_3$ was discovered to have remarkable photovoltaic properties, triggering massive research interest. An entire family of photovoltaic perovskites has since been discovered with near textbook PV absorber properties: direct bandgap, short absorption depths (~100 nm)[2], low non-radiative recombination[3], and high diffusion lengths[4]. The best-performing cells, as of October 2020, have a power conversion efficiency of 25.5%[5]. For more detail on the current state of perovskite-based single-junctions, we refer the interested reader to recent reviews[6–9].

2.3 A Case for Multi-junction Photovoltaics

The barrier of 100 GW growth in the installed capacity of photovoltaic modules was crossed during 2019 and two digit growth is forecast over the next decade at the very least.[10] A very large majority (~95%) of these modules use monocrystalline and multi-crystalline silicon[11]. To further facilitate the adoption of solar electricity, the industry and policy makers are counting on a continuous drop in LCOE that has characterised PV since its inception in the 1950s. However,

the analysis of the cost breakdown of a solar module produced in 2019 (see Figure 2.1) shows that a further cost reduction will be extremely challenging. The cost of installed solar panels can be divided into: the solar module itself, the so-called balance of systems (BoS) which encompasses all the costs associated with the installation (mounting frame, trackers, landscaping, etc.), and the operation of the solar panels (inverter, cleaning, etc.). In the module, the costs are distributed between the barrier materials, interconnections, and finally, the solar cell and the base materials. Although the solar industry has championed cost effectiveness at every level of the fabrication chain, there isn't plenty of room left for improvement. BoS and module fabrication costs are likely to reach a plateau within the next decade. As a consequence, the most promising route for further price reduction and faster adoption of solar electricity is to improve the efficiency of the modules, the rationale being that for a given installed area (in m^2), the installation costs will be the same but the energy yield (in kWh/m^2) will continue to increase.

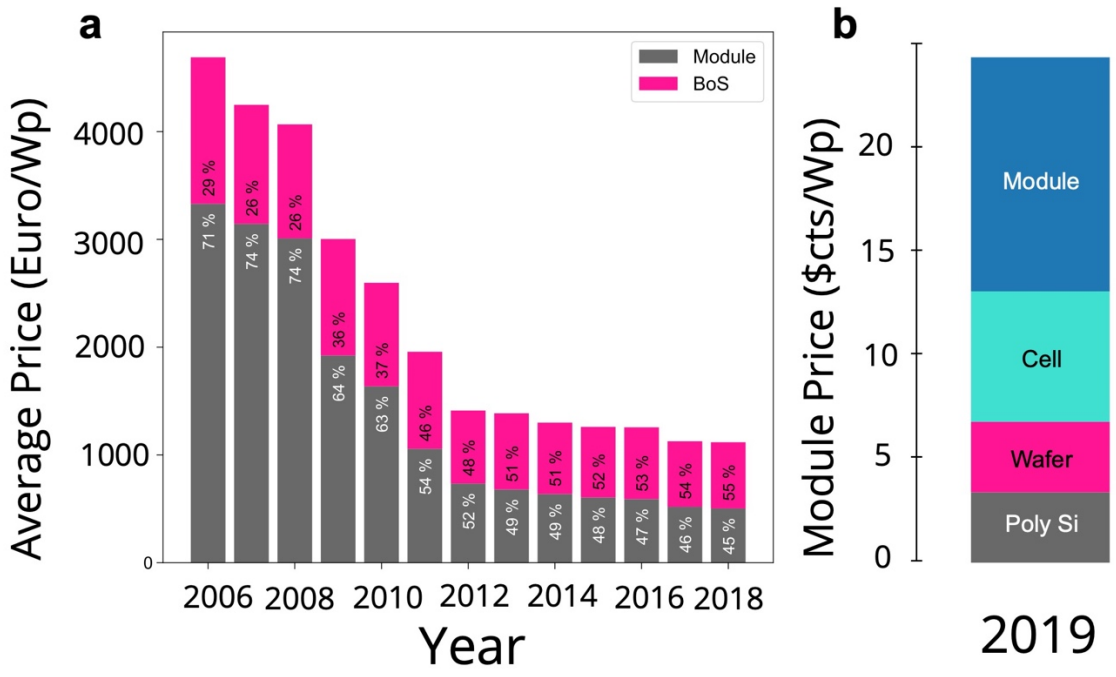

Figure 2.1 | (**a**) Evolution of the average price for a rooftop installation in Germany (10-100 kWp). Since 2013, BoS costs are superior to the module price (adapted from Fraunhofer ISE)[11] (**b**) Cost breakdown of PV module in 2019 (adapted from ITVPR 10th edition)[10]

According to the International Technology Roadmap for Photovoltaics (ITRPV), monocrystalline silicon solar cells will achieve efficiency approaching 25% within 10 years.[10] However, such efficiencies will approach the practical limits of this technology. As is well known, a theoretical efficiency limit for single junction solar cells was proposed by Shockley and Queisser in 1961.[12] According to this model, the maximum efficiency is obtained for a material with a bandgap of E_g = 1.34 eV, where the best compromise is found between thermalisation losses of absorbed photons with energy above bandgap and the number of solar photons available at that bandgap. To date, gallium arsenide (GaAs), $CuIn_xGa_{(1-x)}Se_2$ (CIGS) and perovskites are the only known semiconductors for PV that can be prepared close to this ideal bandgap. Alternatively, several strategies have been proposed to

overcome the Shockley-Queisser limit. These include extracting hot carriers to prevent thermalisation losses, producing multiple carriers per absorption of a photon (by impact ionisation or exciton fission), and multiplying the number of bandgaps in the solar absorbing layers[24]. To date, the last approach is the only practical solution that has been demonstrated and pursued commercially. As we will see below, perovskites, owing to their bandgap tunability and excellent transparency below the band edge, are outstanding candidates for high efficiency multiple-junction (multi-junction) solar cells.

Tandem solar cells, devices comprising a pair of light absorption materials with matched bandgaps stacked on top of each other (see below), have been investigated for many decades. The first demonstration of a tandem solar was already achieved by the Research Triangle Institute in 1979.[13] Compound III-V semiconductors are particularly well suited for such applications due to their bandgap tunability and excellent interfacial properties owing to the epitaxial growth methods developed for these materials. The current world record for the highest solar cell efficiency, an impressive 47.1 %, is held by a 6-junction device under concentrated illumination (143 suns).[14] However, due to their prohibitive fabrication cost, these devices are limited to small area applications such as space (where the efficiency-to-weight ratio is key) and concentrator photovoltaics. Several other absorbing semiconductors have proved to be suitable for use in multi-junction devices. Notably, amorphous silicon could be efficiently combined

with microcrystalline silicon in the 'micromorph' concept proposed by Shah and co-workers in the 1980s.[15] This approach allowed for the scalable fabrication of low cost, moderately efficient solar cells which, before the advent of multi-crystalline silicon in the late 2000s, provided the lowest price-per-watt peak available.[16] Higher efficiencies can be achieved by combining thin film copper chalcopyrite cells such as $CuGaSe_2$ (CGS, E_g~1.7 eV) with $CuInSe_2$ (CIS, E_g~1.05 eV) or Cu(In, Ga)Se_2 (CIGS, E_g~1.15 eV),[17] or as recently demonstrated, III/V semiconductors with c-Si.[18]

In this chapter, we discuss the potential of perovskites for use in multi-junction photovoltaic devices in conjunction with various semiconductors. After briefly explaining the theoretical principles, we discuss the different configurations, challenges, and commercial opportunities, and by reviewing the recent progress in the field.

2.4 How Efficient Can Solar Cells Be?

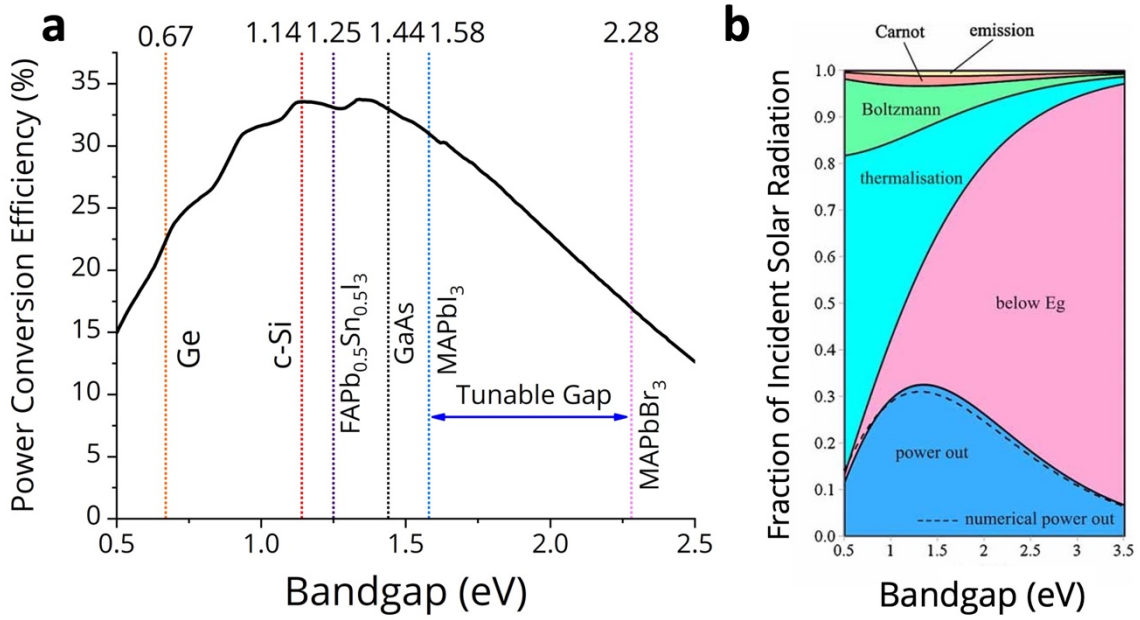

Figure 2.2 | (**a**) The Shockley-Queisser limiting power conversion efficiency for single-junction photovoltaic cells as a function of bandgap. The bandgaps of important solar cell technologies are marked. (**b**) Intrinsic loss mechanisms in a solar cell as a function of bandgap. Reproduced with permission from Hirst L.C. et al (Published by Wiley)[19]

How efficiently can we convert solar energy to work? In the most abstract picture, imagine a solar converter to be a heat engine that circulates a gas of photons between two heat reservoirs, viz. the sun (5800 K) and the earth (300 K). In this picture, thermodynamics allows us to calculate the limiting power conversion efficiency (PCE) of a solar converter to be 93% (Landsberg limit [20]), which is slightly lower than the Carnot limit (95%). Note that this is for a general solar converter whose mechanism of operation is unspecified. If the solar converter at hand is a photovoltaic (PV) cell involving a semiconductor, additional loss mechanisms kick in. Consequently, even the ideal PV cell is much less efficient

than 93%. For a single-junction photovoltaic cell, the theoretically maximum PCE under AM1.5G illumination is 33.7% (Shockley-Queisser Limit[12]) and is achieved at a bandgap of 1.34 eV (Figure 2.2a). At this ideal bandgap, sub-bandgap photon loss and thermalisation loss reach a compromise. Extending the idea slightly to account for non-ideal conditions like non-step function absorptance and auger recombination, the limiting PCE of silicon (29.8%)[21] and ~1.6 eV bandgap perovskite (30.5%)[22] solar cells have also been calculated. The details and assumptions behind the Shockley-Queisser limit are worth examining to understand the loss mechanisms at work. Any strategy to circumvent a loss-mechanism is, in principle, an approach to 'break' the Shockley-Queisser limit.

Several intrinsic losses are at work in the ideal bandgap (1.34 eV) single-junction solar cell: Carnot loss (~2%), emission loss (~1%), Boltzmann loss (~10%), thermalisation loss (~30%), and loss of below bandgap photons (~25%)[23] (Figure 2.2b). Of these, the thermalisation loss is the most prominent and wastes a third of the incident power as heat. When photons of energy greater than the bandgap are absorbed, they excite carriers into higher energy states. Within a nanosecond, these 'hot' carriers cool down (thermalize) to the band-edges, giving away energy as heat. Thus, if any photon has energy in excess of the bandgap, it is quickly dissipated as heat. If this 30% loss can be circumvented, the limiting efficiency can be improved from 33.7% to over 60%. Calculations show that this is indeed the case. Naturally, efforts to develop more efficient photovoltaic cells must find a way

to reclaim this energy. Most proposed third generation technologies[24] attempt to circumvent thermalisation in different ways: spectral splitting, multi-junctions, hot-carrier cells, down-conversion etc. In spectral splitting, different bands of the solar spectrum are guided onto solar cells of different bandgaps, optimised for those wavelengths of light[24]. This is achieved using spectral selective filters. Hot-carrier cells are a hypothetical concept in which excited carriers are extracted before thermalisation can occur[24]. This necessitates the discovery of materials where thermalisation is extremely slow. Secondly, contact materials have to be engineered with a narrow density of states at the appropriate energy level to supress cooling through the contacts. Down-conversion is a process where a high-energy photon is converted into multiple low energy photons, since they are processed more efficiently by the solar cell. This has been demonstrated using quantum cutting[104]. So far, only multi-junction solar cells have been convincingly demonstrated and are industrially scalable.

2.5 How Do Multi-junction Solar Cells Work?

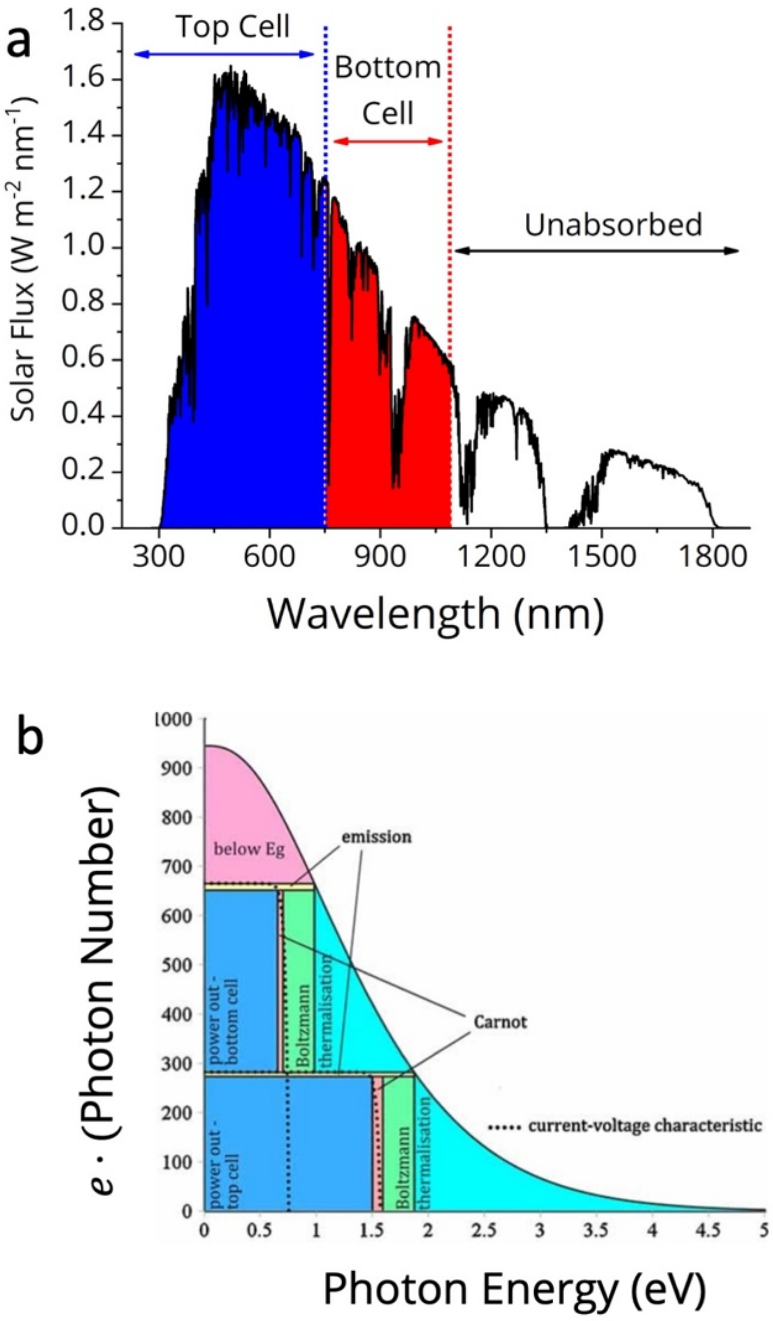

Figure 2.3 | (**a**) Solar irradiance spectrum showing how photons are shared between two absorbers in a perovskite (1.64 eV) on c-Si (1.1 eV) tandem. (**b**) Intrinsic losses in a tandem solar cell with the ideal bandgap combination, 0.98 eV and 1.87 eV. The efficiency gain can be seen to come from the reduced thermalisation. Reproduced with permission from Hirst L.C. et al[19]

As we have discussed, solar cells suffer the largest loss because they waste (as heat) all photon energy in excess of the bandgap. To put it differently, low-bandgap absorbers are inefficient at utilising high-energy photons. This inefficiency can be avoided if we use low-bandgap absorbers for low-energy photons and high-bandgap absorbers for high-energy photons (Figure 2.3a). This is the idea behind the multi-junction solar cell. The multi-junction cells consist of several absorbers with different bandgaps, each specialising in photons of a certain energy range. Each absorber acts like an optical filter for the following one. Light is first incident on the widest-gap absorber, and is successively filtered down to the lowest-gap absorber. Note that light has to be incident on the widest bandgap first for this concept to work. The sub-cells are all connected electrically in series in a 2-terminal multi-junction (see next section for explanation). This results in the V_{OC} being the sum of the sub-cell V_{OC}. In essence, this is akin to stacking many solar cells on top of each other and connecting them electrically in series. Though the current is reduced, the increase in V_{OC} more than makes up for it, increasing the net efficiency. This efficiency gain comes from reduced thermalisation loss (Figure 2.3(b)). Thus, a multi-junction of two cells can reach 42%, a multi-junction of three cells can reach 49%, and so on with diminishing returns. In the limiting case of an infinite stack of sub-cells, the thermalisation loss is eliminated, and an efficiency of 68% can be calculated. The numbers are higher under concentrated sunlight. Solar cells with up to five sub-cells have been

realised so far, yielding a record efficiency of 39% under normal solar irradiance and 46% under concentrated sunlight.

Two-terminal tandems need to be 'current matched'. This means that bandgaps and layer thicknesses have to be chosen such that every sub-cell absorbs the same number of photons and consequently generates the same current. Tandems are at their most efficient when bandgaps are matched.

So far, several kinds of multi-junctions have been demonstrated: III-V, organic-organic, III-V and various multi-junctions involving epitaxially grown III-V semiconductors. These are extremely expensive and have been primarily used for space and concentrator applications.

2.6 2-terminal, 3-terminal and 4-terminal Configurations

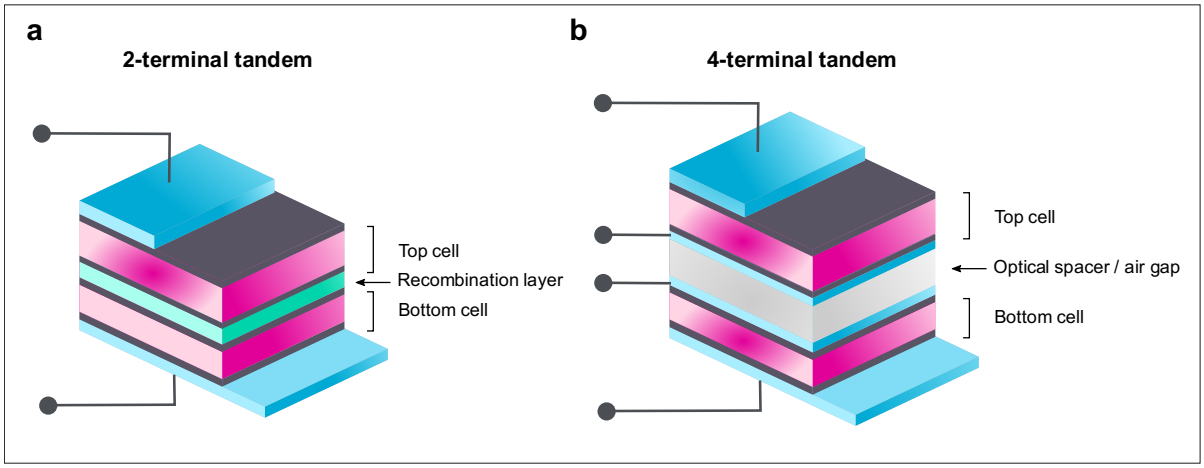

Figure 2.4 | (**a**) Architecture of a 2-terminal tandem, showing the two sub-cells separated by a recombination layer. (**b**) Architecture of a 4-terminal tandem

Two kinds of device configurations are popular for distributing photons between several absorbers. In the case of tandems, they are termed the 2-terminal (2T) and 4-terminal (4T) configurations. The names are derived from the number of electrical contacts emerging from the cell in each configuration. We discuss these with regard to tandems, but they are readily generalisable to more junctions.

In the 4-terminal tandem (Figure 2.4b), two sub-cells are fabricated on separate substrates and mechanically stacked on top of each other such that the narrow bandgap sub-cell receives light filtered through the wide gap sub-cell. Electrically, both the cells are completely independent, yielding four electrical contacts. The sub-cells are biased independently, with their own maximum power point tracking, inverter etc. This can cause a substantial increase in cost, since the balance of system costs form a large fraction of the total cost of producing solar energy. Since the cells are isolated, each cell is also isolated from any problems or degradation that may occur in the other. Of the four electrical contacts, three must be semi-transparent, leading to some resistive and optical losses in 4T tandems. An advantage of 4T compared to monolithic integration is that the current of the sub-cells does not need to be matched. This gives a small increase of energy yield in practical applications, since the efficiency is less dependent on

the solar spectrum, and thus less dependent on changes in irradiation during the day, either due to cloud coverage or the sun's zenith angle.[25]

In the 2-terminal tandem configuration (Figure 2.4a), the two sub-cells are fabricated on top of each other, such that the two are electrically connected in series. Thus, only two electrical contacts are required. This connection between the sub-cells is usually achieved using a tunnel junction or a low resistance recombination layer. As in the 4-terminal tandem, the wide gap cell acts as an optical filter for the narrow gap cell. However, the series connection means that the same current will flow through the two sub-cells (Kirchhoff's law[26]). If the two sub-cells generate different currents, the net current will be determined by the lower of the two. Hence, photocurrents in these cells must be matched to ensure the same photocurrent generation at the maximum power point. This requires careful management of layer thickness and bandgaps. There is no current matching requirement in a 4T terminal tandem since the sub-cells are biased independently. However, current matching is still desirable for best performance.

The 2-terminal multi-junction is more difficult to fabricate than the 4-terminal tandem. However, the 2-terminal multi-junction is less expensive, both in terms of module cost and balance of system costs. There is always the disadvantage of possible catastrophic failure with the 2-terminal multi-junction: if any sub-cell

incurs a problem, the entire cell stops working. All examples of commercially manufactured tandem solar cells are based on a 2-terminal design.

A 3-terminal tandem concept has also been proposed, though not much progress has been made[27]. Its main advantage is that it combines the ease of fabrication of the 2-terminal tandem (requiring wiring only in the front and back of the cell stack), and the flexibility that a 4T tandem offers (more choice of bandgap, less spectral sensitivity)[28].

2.7 Why Perovskites for Multi-junctions?

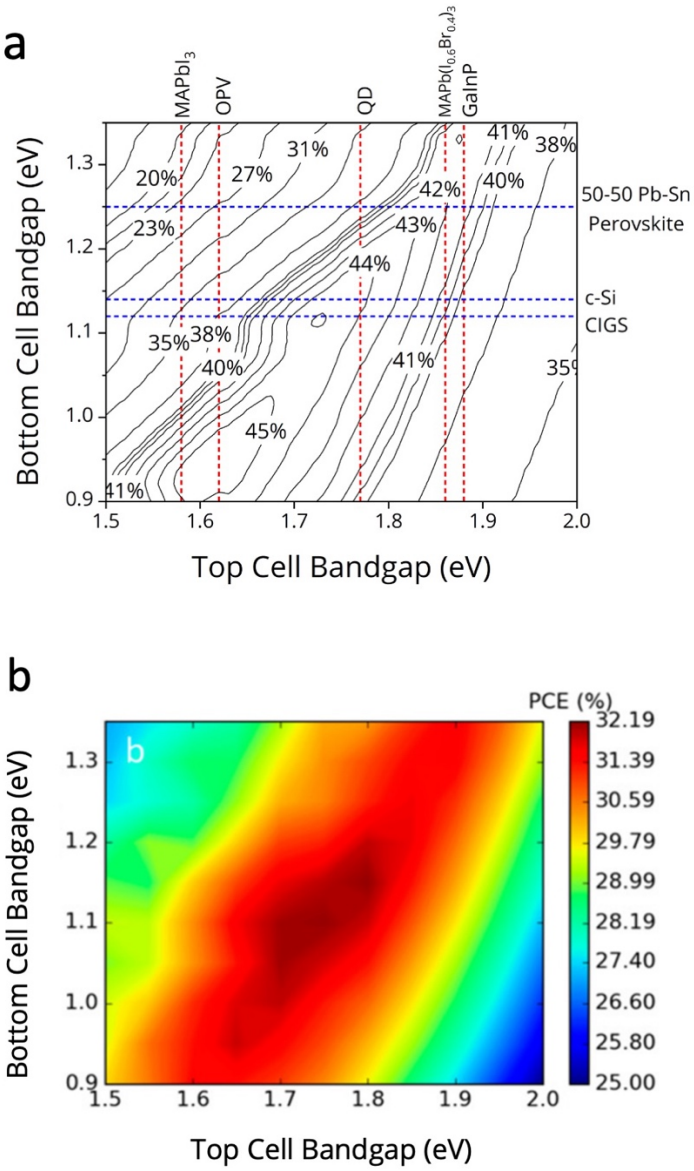

Figure 2.5 | (**a**) Power conversion efficiency of a 2-terminal tandem, as a function of the bandgap, calculated in the radiative limit. The representative bandgaps of some PV technologies are indicated: Organic PV (OPV)[29], $MAPbI_3$ perovskite, $MAPb(I_{0.6}Br_{0.4})_3$ perovskite, $CsPbI_3$ Quantum Dots (QD)[30], GaInP[31], $FA_{0.83}Cs_{0.17}Pb_{0.5}Sn_{0.5}I_3$ (50-50 Pb-Sn Perovskite), crystalline silicon (c-Si), and Copper Indium Gallium Selenide (CIGS)[32]. (**b**) Modelled power conversion efficiency of perovskite-perovskite tandems, as a function of sub-cell bandgaps. Reproduced from the work of Hoerantner et al[33] (Published by the American Chemical Society).

We have already made a case for multi-junctions (including tandem) being the optimal strategy to make solar cells with higher efficiencies. While highly efficient multi-junction efficiency (>40%) solar cells have already been made, these involve epitaxially grown III-V semiconductor junctions, which can be two or three orders of magnitude more expensive per watt. A GaAs based multi-junction cell costs up to 300$/watt[34]. In comparison, a utility scale solar is only 1$/watt. This cost makes epitaxially grown multi-junctions only practical in concentrator PV, or niche applications like space or military. Furthermore, from the established inorganic semiconductors, the choice of bandgaps is limited: Si (1.1eV), CIGS (1.0-1.7 eV), GaAs (1.42 eV), CdTe (1.5 eV), InGaP, etc. Even then, it is not guaranteed that two absorbers with perfectly matched bandgaps can be combined. Furthermore, some of these materials cannot be scaled to terawatt proportions due to elemental scarcity and/or low production capacity.

The bandgap tunability of perovskites provides an answer to this issue by opening up the possibility of creating scalable tandems. The bandgap can be tuned across the visible spectrum simply by ionic substitution and mixing. In the case of ABX_3 perovskites, by selecting suitable cations and halides, the bandgap can be tuned between ~1.24 eV to 3.5 eV. However, to form structurally stable perovskites, the size of the components has to be carefully matched. A reasonably good prediction can be obtained by using Goldschmidt's tolerance factor based only on ionic radii. The following ions are the most popular: A = Cs,

methylammonium (MA), formamidinium (FA), B = Sn^{2+}, Pb^{2+} and X = I^-, Br^-, Cl^-. In particular, the mixed-halide I-Br perovskites $APb(I_xBr_{1-x})_3$ have a bandgap between 1.48-2.35, making them suitable for designing wide gap cells for tandem (Figure 2.5a) and triple junction applications. Perovskite-on-silicon (see section below) and CIGS-perovskite cells[35] have been demonstrated using these materials. The $APb_{0.5}Sn_{0.5}I_3$ perovskites (E_g ~1.2 eV) are suitable as a narrow gap absorber, opening up the possibility of designing all-perovskite multi-junction devices (Figure 2.5b). All the elements in perovskites (with the exception of caesium) are available in great abundance and are already produced in copious quantities. The high power/mass ratio also makes it more attractive than Si based multi-junctions for space applications.

Additionally, high efficiency multi-junctions, which have mostly been epitaxially grown, have been limited to a few niche applications due to high costs. Concentrator PV has been one such application where the expensive cell is kept small and optics is used to gather sunlight over a large area. Perovskite based multi-junction technology, which avoids expensive epitaxy, has the potential to enable concentrators on a large scale. Perovskite cells have been demonstrated to be compatible with concentrated sunlight.[36]

The annual energy yields of photovoltaic arrays can be reliably predicted based on optoelectronic models, which accept irradiance data as input.[25] These predictions are quite crucial in an industry that already runs on razor thin margins.

For thin-film solar cells, the generalised transfer-matrix method is commonly used to simulate the cell optics. The electronics can be handled either by a simple diode-based or drift-diffusion model. Hörantner M.T et al.[25,33] have calculated that tandems have over 30% higher annual energy yields than single junctions. More precisely, efficiencies of 31.8% (perovskite/Si) and 33.4% (perovskite/perovskite) are possible, within practical limits, if all perovskite sub-cells were state-of-the-art. In the triple junction configuration, even higher efficiencies are possible: 36.6% (perovskite/perovskite/perovskite) and 38.8% (perovskite/perovskite/Si).

2.8 Perovskite-Silicon Tandems

In October 2014, the first report of a perovskite containing a multi-junction photovoltaic device was a thin-film, 2-terminal perovskite-kesterite tandem reaching an efficiency of 4.4%.[37] This result was soon overtaken by 4T and 2-T perovskite-silicon tandems, with efficiency exceeding 20% by the end of 2015.[38] Combining perovskite with silicon solar bottom cells is attractive for several reasons. First, silicon PV is the mainstream technology, which has driven the decrease of price over the last decade and accounts for more than 95% of the annual PV production capacity.[39] Next, the bandgap of the most efficient perovskite absorbers (~1.55 eV) is relatively well suited to the bandgap of crystalline silicon (~1.12 eV). In a 2-terminal tandem with such bandgaps, the maximum efficiency is slightly above 30%, mostly limited by the current matching

conditions.[40] However, to achieve higher efficiency, the tunability of the bandgap towards 1.65–1.70 eV presents a substantial advantage, with maximum theoretical efficiency above 40% (Figure 2.5a).[40] Finally, since transparent conduction oxides (TCO) are already in use for heterojunction silicon PV, the latter technology is particularly suitable for tandem devices with perovskites.

Just like in single junction perovskite photovoltaics, research activities in perovskite/silicon tandem solar cells have been flourishing since the first reports in 2014, with more than 80 reports published by the end of 2019 (see Figure 2.6). This topic has already been reviewed several times,[41–46] and efficiency is increasing steadily. Therefore, an exhaustive review of the progress will soon be outdated. We invite the reader to refer to the most recent reviews to learn about the current status of the research, while we concentrate here on the particular challenges needed to be overcome to reach practical power efficiencies above 30%.

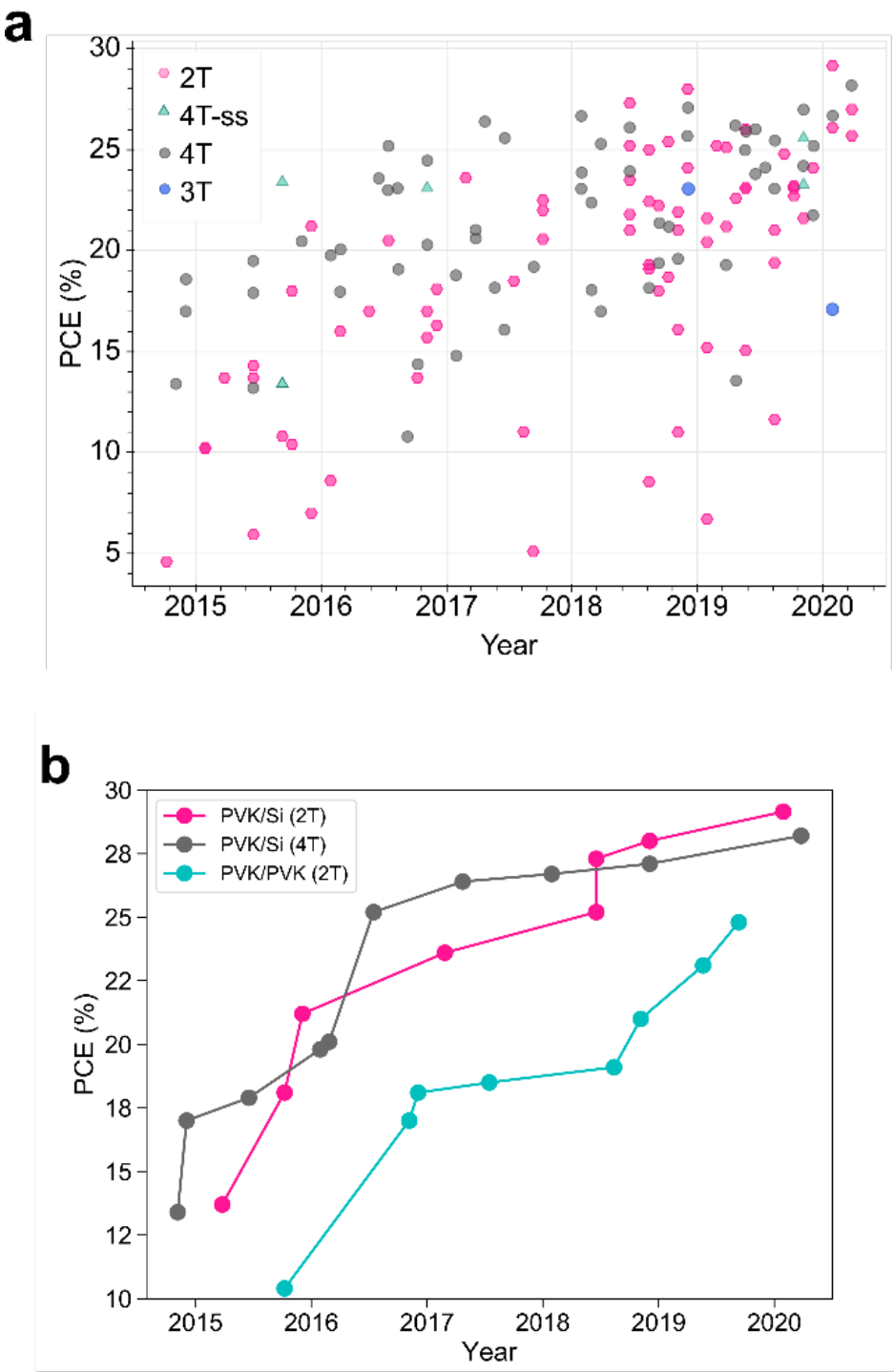

Figure 2.6 | (**a**) Reports of tandem solar cells using at least one perovskite absorber as sub-cell. 2T: 2-terminal, 4T-ss: 4-terminal with spectral splitting, 4T: mechanically stacked 4-terminal, 3T: three-terminal. (**b**) Evolution of record efficiencies of perovskite/silicon 2-T and 4T devices, and all-perovskites 2-T tandems (including press releases from Oxford PV and Helmholtz-Zentrum Berlin).

2.9 Bandgap engineering

If we use the Shockley-Queisser detailed balance model to estimate the maximum theoretical efficiency of a tandem cell based on a silicon bottom cell, the bandgap of the top absorber should be of 1.75 eV. However, when calculating the maximum efficiency using experimental optical constants and reasonable film thicknesses, the optimal bandgap for a 2-terminal device is slightly lower, between 1.65 and 1.70 eV, due to the finite slope of the absorption edge.[25] To achieve such bandgaps, several perovskite compositions can be envisaged. For example, cesium lead iodide ($CsPbI_3$) with a bandgap of 1.73 eV would be highly advantageous.[47] Unfortunately, this composition is metastable in its perovskite black phase, and is promptly converted into a yellow non-perovskite phase upon exposure to ambient air.[48] Nevertheless, several strategies to stabilise $CsPbI_3$ in its perovskite phase have been reported, using layer-by-layer assembly of nanocrystals,[49] preferential crystallisation in its tetragonal β-$CsPbI_3$ polymorph[50], or by adding small amounts of dimethylammonium together with Cs as an A cation.[51,52] However, a tandem device with silicon has yet to be demonstrated.

Alternatively, the bandgap can be widened by mixing bromide with iodide in Pb-based perovskite using organic A cations (*e.g.* MA, FA) or in mixed composition with inorganic cations (Cs, Rb). This approach provides a large combinatorial parameter space which has been and will probably be explored further in the

future. However, a number of limitations need to be considered when designing an optimal perovskite composition. The thermal stability of perovskites using MA as A cation is generally less than those using FA or Cs, due to its higher volatility and chemical reactivity. On the other hand, an FA-based perovskite can turn into a yellow non-perovskite phase, just like the Cs-based analogues. McMeekin et al. discovered that by mixing a small amount of Cs with FA, stable compositions of mixed-halide perovskites could be obtained over a large range of iodide-bromide ratios.[53] Most of the high efficiency perovskite-silicon tandem reported so far (with PCE > 25%, see Figure 2.6) are based on mixed-cation (Cs, MA, FA), mixed-halide (I, Br) perovskites.

Although accurate tuning of the bandgap can be achieved using composition engineering, the efficiency of perovskite solar cells with a significant amount of bromide (typically 40%) is lagging behind that of neat iodide perovskites.[54] This is particularly clear in the increasing V_{OC} loss with higher bromide content.[54] Some authors have attributed this loss to the halide segregation effect observed with mixed anion composition. This effect is clearly demonstrated by the reversible shift of the photoluminescence peak towards a lower bandgap under constant illumination. This has been imputed to the migration of ions giving rise to iodide-rich regions, but the actual mechanism is currently still under debate, despite extensive research effort.[55,56] However, a careful analysis of the effect of halide segregation on the V_{OC} deficit revealed that the dominant contribution to this loss

was non-radiative recombination, and segregation actually played a relatively minor role.[57]

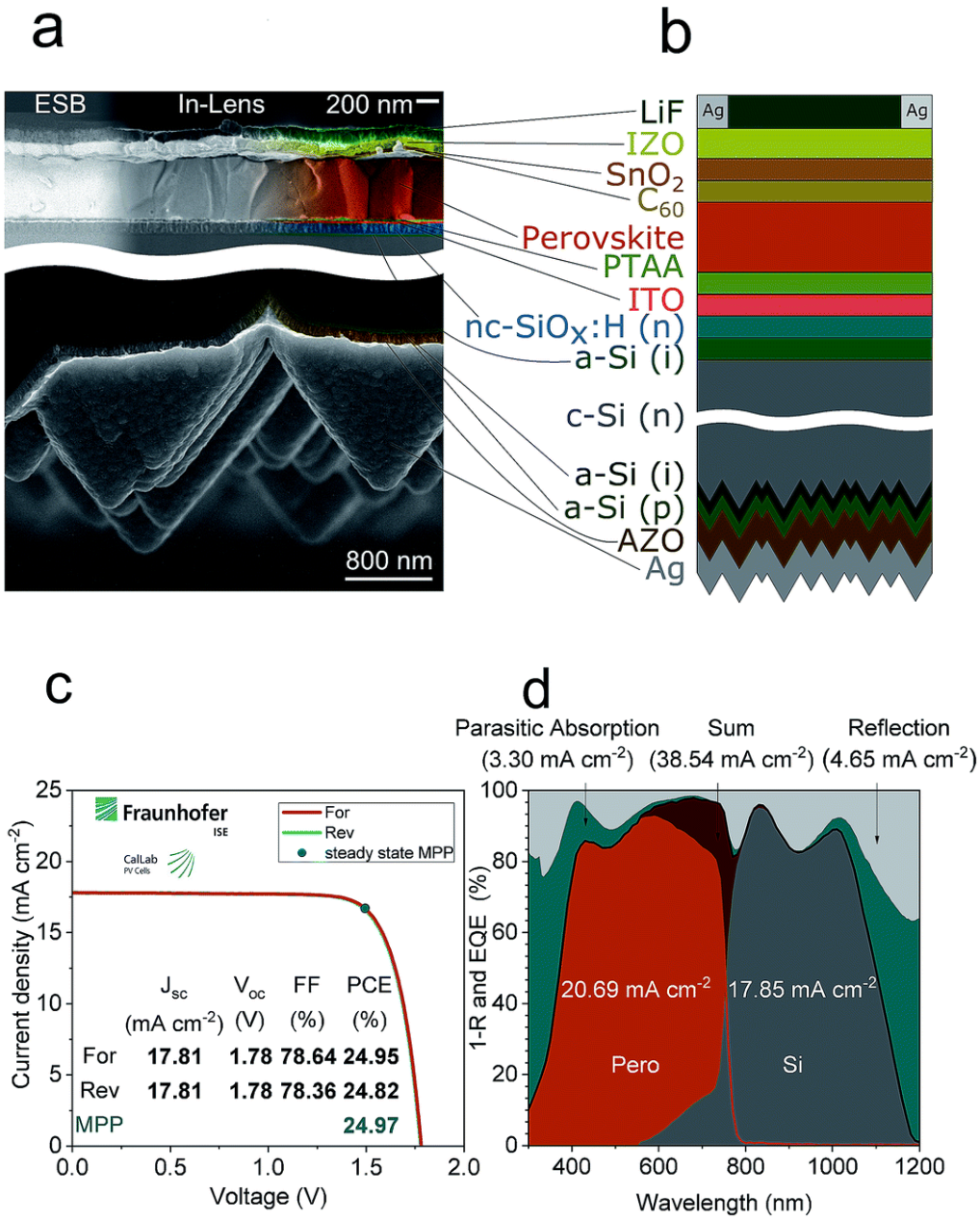

Figure 2.7 | Architecture and performance of a 2-terminal perovskite on a back-textured silicon heterojunction sub-cell. Reproduced from Köhnen et al.[58] (Published by The Royal Society of Chemistry) (**a**) Coloured cross sectional SEM image of the top cell (upper panel) and back side of the bottom cell (lower panel) of a typical monolithic tandem solar cell. The left side of the top cell is recorded with an energy selective backscattered (ESB) detector, the right side with an in-lens detector (b) schematic device layout of the tandem architecture. (c) Certified current density–voltage (J–V)-characteristics (d) Measured external quantum efficiency and reflection spectra with integrated current densities and their sum as indicated. Additionally, the loss in current density due to parasitic absorption (as the difference between sum of the EQE and 1-reflectance) and reflection are shown.

2.10 Parasitic absorption

In common with all types of multi-junctions, the optical quality of the perovskite-silicon tandem stack needs to be carefully optimised. In Figure 2.7d, we show a plot of the external quantum efficiency illustrating various loss mechanisms limiting the maximum current that can be extracted from the device.

First, we discuss the sources of parasitic absorption in a common tandem architecture. In an ideal device, high-energy photons are only and totally absorbed into the top-cell—in this case the perovskite, and the lower-energy photons into the silicon sub-cell. This requires all the other layers in the stack to be transparent in a given range of the solar spectrum. Materials used in contacts and recombination layers are usually selected to be transparent over the whole spectral range, although this is not strictly required in the blue range for materials in the bottom cell.

With the exception of the interdigitated back contact (IBC) architecture, incident solar light has to be transmitted first through a transparent electrode on top of the photovoltaic device. This is inevitably at the cost of parasitic absorption losses and unwanted reflection, which we will discuss later. The transparent electrode needs to be highly transmissive over the majority of the visible spectral range, as well as in the near-infrared region for the silicon cell below. In addition, low sheet resistance is required to maintain the fill factor, most critically when the

device area increased. The vast majority of 2T and 4T perovskite/silicon tandem devices use indium-tin oxide (ITO) as the transparent conducting oxide (TCO). However, ITO sputtering can damage the organic charge selective layer, and normally requires an annealing step above 200°C. Alternative TCOs have been proposed such as IZO[59], AZO,[60] or hydrogenated indium oxide (IO:H).[61] Another approach is to use transparent metallic electrodes such as silver nanowires[62] or ultrathin evaporated metals such as Au sandwiched between MoO_x.[63]

Most importantly, the top absorber needs to be highly absorbing above bandgap but completely transparent below bandgap. This is one of the major advantages of perovskites which, being high quality direct gap semiconductors, have absorption coefficients to the order of 10^4 cm^{-1} near band edge. Moreover, they are highly transparent below bandgap, which is illustrated by a low Urbach energy—the characteristic energy associated with the exponential tail of the absorption spectrum, and the absence of absorbing sub-gap defect states. However, complete absorption of high energy photons in the perovskite sub-cell is limited by the thickness of the film, which must be consistent with the photo-generated charge diffusion lengths. By improving the quality of the perovskites, the thickness of the absorber layer is steadily increasing up to 1 μm and above.[59] We note that while incomplete absorption in the top-cell can be compensated by absorption in the silicon, it still has a cost in terms of maximum power due to the loss in voltage.

All efficient perovskite sub-cells are based on a heterojunction architecture, and thus use p and n selective layers on each side of the absorber. Although they can be very thin, parasitic absorption in these layers can play a significant role. There is a relatively large choice of organic p-type selective layers that fulfil these conditions, including polymers (*e.g.* PTAA, pTPD, PEDOT:PSS) and small molecules (spiro-MeOTAD, spiro-TTB). There are currently fewer candidates for inorganic p-type selective layers, with the notable exception of NiO.[64] Interestingly, the current world record device used an ultra-thin self-assembled monolayer as a p-type contact with negligible parasitic absorption.[65] On the other hand, although there is a wider choice of inorganic n-type contacts (*e.g.* SnO_2, ZnO, TiO_2), highest efficiency devices usually include a fullerene selective layer (C_{60}, PCBM). Due to a non-negligible parasitic absorption in the fullerenes and evidence for non-radiative recombination at this interface,[3] an alternative material would be desirable. In a tandem device using a silicon heterojunction bottom cell, parasitic absorption in the doped hydrogenated amorphous silicon (a-Si:H) carrier selective layers is a significant source of current losses. For a single junction silicon cell, this can correspond to up to 2 mA/cm^2.[66] One way to mitigate this parasitic absorption is to replace the p-type amorphous silicon layer with nanocrystalline silicon oxide[67] or transition metal oxides, like MoO_x.[66] We note also that, due to the effusion of hydrogen from the amorphous silicon layers, the processing temperature of such devices is limited to ≈ 200°C. This precludes the use of

charge-selective layers that require higher temperature annealing or sintering, like mesoscopic TiO_2 which is usually sintered at 450-500°C.

Another notable source of parasitic absorption is the recombination layer, which is required to electrically connect the two sub-cells by recombining the hole current from the p-type contact of one cell to the electron current from the n-type contact of the other cell. Ideally, the recombination should be transparent below the bandgap of the top-cell and have a very low electrical resistance. The recombination layer can either be achieved with a tunnel junction consisting of a highly doped p-n junction,[68,69] or with a low-resistance conducting transparent oxide, such as ITO or IZO.

2.11 Optical management

In addition to parasitic absorption losses, reflections play a major role in the efficiency of the tandem stack, in both 2-terminal and 4T configurations. Reflections from the front surface can be reduced relatively easily by the deposition of an anti-reflection coating (ARC), such as a thin dielectric layer (*e.g.* LiF or MgF_2). However, accurate optical management is required in order to optimise the reflections at each interface, so as to design devices with appropriate absorber layer thicknesses. The two main constraints governing the choice of the perovskite layer thickness are: (i) the photogenerated carrier diffusion lengths, and (ii) the current matching conditions between the sub-cells in a 2T device. To

optimise a full device stack, optical modelling is usually performed using well-established techniques such as the transfer matrix method.

Although all layers of the stack need to be included to optimise the optical properties of the device, some interfaces play a predominant role. First, when using a TCO as the intermediate recombination layer, strong reflections are generated due to the low refractive index of the oxide (n_{ITO} ≈ 1.4-2) and the strong contrast between the indices of the perovskite (n_{PVK} ≈ 2.6) and silicon (n_{Si} ≈ 3.6). This effect can be reduced with the use of nanocrystalline silicon junctions with higher refractive index (n_{ncSi} ≈ 2.6).[67,69] Secondly, polished silicon surfaces are strongly reflective, and therefore the vast majority of commercial silicon solar cells are textured on both sides via a KOH-etching process. The pyramids generated by this process are typically a few microns high (Figure 2.7a), and therefore pose a major challenge in the deposition of the sub-μm continuous layers required for the perovskite sub-cells. Sahli et al.,[70] demonstrated an efficient tandem on a fully-textured silicon cell using a combined vapour and solution processing method. This problem can be mitigated by using back-only textured silicon wafers, and/or with the use of antireflection textured foils deposited on top of the device.[71]

Top cell	Eg (eV)	Bottom cell	Eg (eV)	Recombination layer	Area (cm^2)	J_{SC} ($mA \cdot cm^{-2}$)	V_{OC} (V)	FF (%)	PCE (%)	Year/ref.
$MAPbI_3$	1.55	CZTSSe	1.1	ITO	0.45	5.6	1.35	60	4.6	2014/[72]
$MAPbI_3$	1.55	Polymer	≈1.3	PEDOT:PSS	0.1	10.1	1.52	67	10.2	2015/[73]
$MAPbI_3$	1.55	Homojunction	1.1	n^{++}/p^{++} Si	1	11.5	1.58	75	13.7	2015/[62]
$FAMAPbI_{3-x}Br_x$	1.57	SHJ	1.1	ITO	0.16	14.0	1.78	79	18.1	2015/[74]
$MAPbI_3$	1.55	SHJ	1.1	IZO	0.17	15.9	1.69	78	21.2	2015/[75]
$MAPbI_3$	1.55	SHJ	1.1	IZO	1.43	16.4	1.72	73	20.5	2016/[61]
$FA_{0.83}Cs_{0.17}Pb(I_{0.5}Br_{0.5})_3$	1.8	$FA_{0.75}Cs_{0.25}Sn_{0.5}Pb_{0.5}I_3$	1.2	ITO/IZO	0.2	14.5	1.66	70	17.0	2016/[76]
$FA_{0.85}Cs_{0.15}Pb(I_{0.7}Br_{0.3})_3$	≈1.7	$MAPbI_3$	1.55	TaTm:F_6-TCNNQ/C_{60}:PhIm	0.03	10.1	2.28	76	17.4	2016/[77]

$FA_{0.83}Cs_{0.17}Pb(Br_{0.17}I_{0.83})_3$	1.63	SHJ	1.1	ITO	1	18.1	1.65	79	23.6	2017/[64]
$Cs_xFA_{1-x}Pb(I,Br)_3$	1.6	SHJ	1.1	nc-Si tunnel	1.42	19.5	1.79	73	25.2	2018/[70]
$Cs_{0.09}FA_{0.77}MA_{0.14}Pb(I_{0.86}Br_{0.14})_3$	1.64	CIGS	1.0	BZO/ITO	0.04	17.3	1.77	73	22.4	2018/[78]
$Cs_{0.15}(FA_{0.83}MA_{0.17})_{0.85}Pb(I_{0.8}Br_{0.2})_3$	1.64	SHJ	1.1	ITO	0.42	17.8	1.80	79	25.4	2018/[79]
$Cs_{0.05}(FA_{0.83}MA_{0.17})_{0.95}Pb(I_{0.8}Br_{0.2})_3$	1.63	SHJ	1.1	ITO	1.1	19.0	1.79	74	25.4	2019/[67]
$Cs_{0.05}FA_{0.8}MA_{0.15}PbI_{3-x}Br_x$	1.75	$(FASnI_3)_{0.6}(MAPbI_3)_{0.4}$	1.25	(ITO)	0.11	15.0	1.94	80	23.1	2019/[80]
$FA_{0.78}Cs_{0.22}Pb(I_{0.82}Br_{0.15}Cl_{0.03})_3$	1.67	SHJ	1.1	ITO	1	19.1	1.89	75	27.0	2020/[71]

Table 2.1 | Notable reported 2-terminal tandem solar cells that include perovskites in at least one sub-cell.

2.12 Perovskite-Perovskite Tandems

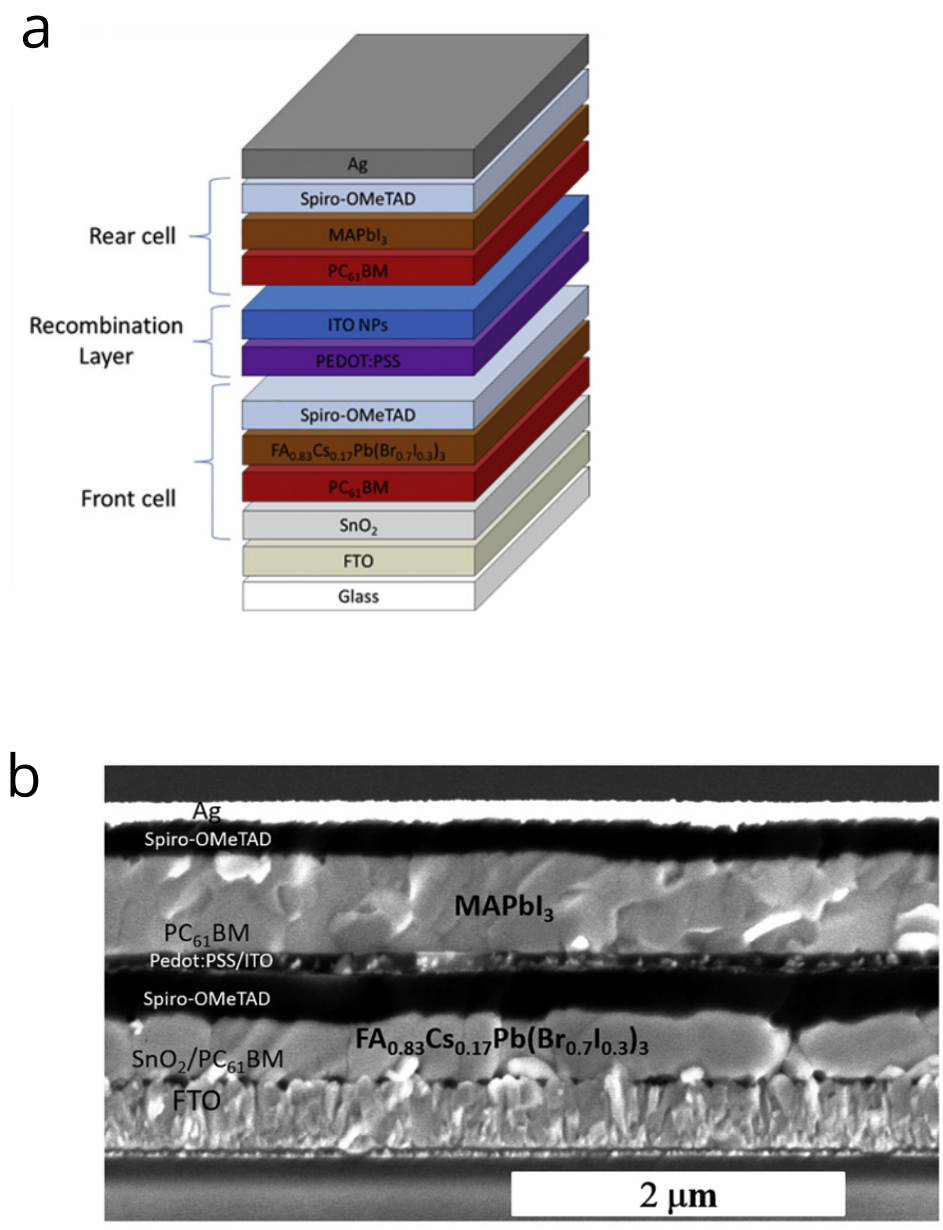

Figure 2.8 | Architecture and cross-sectional scanning electron microscopy on a typical 2-terminal perovskite-perovskite tandem solar cell. Reproduced from McMeekin et al.[81] (Published by Cell Press) (a) Tandem cell architecture (b) Cross sectional scanning electron microscopy on the tandem.

The idea of an all-perovskite multi-junction solar cell is attractive since these devices would enable over 30% PCE (over 40% in the theoretical limit), while having the advantage of low-temperature processing, high manufacturing throughput, and the ability to use flexible and lightweight substrates. The first 2-terminal all-perovskite tandem (7% PCE) was realised in 2015, and the current (and rapidly moving) record is 25% PCE, published by Tan H. and co-workers[82] in October 2019 . This cell exhibits a V_{OC} of 1.93 V, J_{SC} of 15.8 mA/cm^2, and a fill-factor of 81%. All the perovskite-perovskite cells made so far have followed the template of using a Sn-Pb based perovskite for the low gap cell, and a neat lead mixed-halide perovskite for the wide-gap cell. The maximum possible short-circuit current for the perovskite-perovskite tandem is set by the low bandgap sub-cell, which is 1.22 eV for the lowest bandgap perovskite ($FAMAPb_{0.5}Sn_{0.5}I_3$). The ideal companion sub-cell for this would be 1.80 eV[33], which is approximately achieved by a perovskite with 40:60 Br to I ratio. We note, however, that 1.22 eV is still a larger bandgap than ideal (Figure 2.5b). If a perovskite with a bandgap smaller than 1.22 eV could be found, it would have the dual advantage of moving closer to the thermodynamic optimum and allowing for decreasing the bandgap of the wide gap cell. This is a natural advantage enjoyed by perovskite-on-Si tandems.

The most serious barrier towards 30% PCE is the poor performance of mixed-halide perovskites. Perovskite compositions with higher bromide contents have, so far, failed to achieve the same excellent device efficiencies that distinguish their

iodide-rich counterparts. The best iodide-rich perovskites have voltage losses of ~60 mV from the radiative limit.[83] In comparison, bromide rich cells show hundreds of millivolts of voltage loss. The bulk of this loss arises from high trap densities in the absorber and the perovskite-charge transport layer interfaces.[84] This is further exacerbated by the photo-instability of these phases: they are prone to segregating into iodine-rich and bromide-rich phases upon illumination.[85] This is a secondary but significant, contributor to the voltage loss.

Electronically, lead-tin perovskites perform extremely well, reaching open-circuit voltages higher than 0.85 V[86–88] from a bandgap ~1.2 eV. The V_{OC} loss from the thermodynamic limit is even smaller than in c-Si cells. However, they present optical challenges: Lead-tin perovskites do not absorb as strongly as lead perovskites, especially close to the bandgap. The reasons for this are not fully clear. The performance of these cells has been limited by poor absorption in the NIR, which reduces available photo-current by as much as 3 mA/cm^2. Tan H. and his/her co-workers have shown that this current can be recovered by fabricating thick films (860 nm) with large diffusion lengths.[82] McGehee and co-workers have passed the IEC 61646 standard test (damp heat aging for 1000 h at 85°C with 85% relative humidity) on encapsulated Pb-Sn solar cells that replace MA by Cs and use ITO as the electron blocking layer.[89] These developments should lead to significantly improved tandem cell performances when implemented in cells.

Optical challenges become more severe in perovskite multi-junctions. Layer thicknesses have to be chosen carefully. This is due to optical interference effects, which become very important in thin-film devices. Reflections at various interfaces in the cell interfere to create dips and valleys in light intensity within the stack. The large numbers of layers (>10) in multi-junctions can make this effect prominent. In ideal circumstances, we would want maximum light intensity with the absorber, and minimum light intensity within layers that absorb parasitically. This can be achieved by carefully tuning the layer thicknesses with the aid of optical simulations (typically a Transfer Matrix model). Layer thicknesses have to also be carefully selected to meet the current matching condition, i.e. both sub-cells must generate the same short-circuit current. The challenges discussed above for perovskite-Si tandems are also applicable here.

In 2-terminal multi-junctions, the sub-cells are electrically connected in series. This is usually achieved through a recombination layer that is sandwiched between the charge transport layers of successive sub-cells. For perovskites, this is most commonly chosen to be ITO, for the ease of solution processing succeeding layers. This deposition is made complicated, however, by the possibility of damaging the underlying layers during the sputtering process. Several groups have developed protective buffer layers to protect from sputter damage[64,74,76,90]. MoO_x, NiO, VO_x, AZO, SnO_2 are some materials that have been used previously. These are typically thin (5-20nm) to not impede transport. There

is also the constraint of low temperature processing (< 150°C) due to the presence of organic selective layers. An organic p-n junction using highly doped n and p organic materials has also been demonstrated in fully evaporated tandems[91]. However, this does not ensure good long-term stability, as the thin organic layers cannot prevent the release and migration of metal and halide ions. In short, the field faces the challenge of developing a stable interlayer with good vertical and poor horizontal conductivity, so that it does not damage underlying layers and remains suitable for low temperature deposition.

2.13 Characterising Tandems

The characterisation of tandem solar cells is notably less straightforward than for single junction devices. In this section, we discuss the concepts and techniques required for accurate and reproducible determination of photovoltaic device performance. For JV curves and steady-state efficiencies, the spectral mismatch between the calibrated reference diode and the device under investigation can be difficult to determine accurately, as we discuss below. In addition, the measurement of EQE of the independent sub-cells is challenging, especially when the absorption spectra of the active layers overlap. These issues, as well as best measurement practices, have been reported previously for III-V multi-junction devices[92–94] and for organic PV cells.[95] In principle, the methods developed for these technologies are applicable and should be accurately followed, considering

the particularities of perovskite solar cells when acquiring JV curves for the calculation of the mismatch factors.

Hereafter, we briefly describe the recommended procedure to obtain reliable performance characterisation of 2-terminal multi-junction solar cells. In order to determine the performance of the device under standard test conditions (i.e. AM1.5G, 100 mW/cm^2), the spectrum of the solar simulator has to be adjusted so that each sub-cell generates the same photocurrent as under the AM1.5G reference spectrum. This can be achieved with a dual or multi-zone solar simulator, with each zone chosen to match the spectral response of each sub-cell. Each sub-spectrum can then be adjusted mathematically with a spectral mismatch correction that requires the knowledge of the solar simulator spectrum and the spectral response of each sub-cell.

Therefore, the first stage consists in the accurate measurement of the spectral response (or external quantum efficiency, i.e., EQE) for each sub-cell. In practice, this can be achieved for a given sub-cell by saturating all other sub-cells with monochromatic bias illumination so that the photocurrent of the full stack is limited by the response of the sub-cell under test. In case of an overlap of the sub-cells' spectral range, as commonly observed in organic solar cells, optical modelling is required to determine their relative contributions to the photocurrent. In addition, voltage biasing needs to be applied so that the sub-cell under test runs at near short-circuit conditions, and also to prevent artefacts

appearing in the case of low shunt resistance or low reverse breakdown voltage.[92] Such artefacts can be identified by performing a dark spectral response (i.e. when no bias light is applied) measurement on the multi-junction device.[96] Once the spectral responses have been obtained, a mismatch factor can be calculated for each sub-cell. Then, in order to generate the required photocurrent in each sub-cell, the spectrum of the solar simulator can be adjusted and tested by measuring the J_{SC} of a reference solar cell under the new spectral conditions. New mismatch factors can then be calculated. This process must be run iteratively until a consistent photocurrent is obtained for the reference solar cell. This process is only achievable by using a multi-source solar simulator, dual-source for tandem cells, in which the spectra of the light sources are fixed but the intensities can be adjusted independently.[93] If the overall spectrum of the light source is fixed, then although the mismatch factor can be applied to an accurate estimate of the J_{SC}, it is highly likely that the current density will be mismatched between the multi-junctions, and the *FF* of the multi-junction solar cell will be overestimated, in comparison to what would be obtained under true AM1.5G.

2.14 Commercialisation

As mentioned in the introductory section of this chapter, the contribution of the balance of system costs (BoS), including the inverter, construction, installation and mounting structure, now accounts for more than 50% of the levelized cost of

electricity (LCOE).[11] Therefore, the best way to further decrease LCOE is to improve the module power conversion efficiency since all other costs scale with the installed area. The cost of the module itself will continue to go down, mostly due to cost savings as the silicon technology is reaching its practical efficiency limits. Recently, the solar industry widely adopted the PERC (Passivated Emitter and Rear Cell) silicon technology, in part due to its relatively low upgrade cost. In 2019, commercial PERC cells reached up to 22% efficiency, with the best estimates forecast approaching 24.1% by late 2020.[97] The world record is currently 26.7%,[98] but this seems out of reach for commercial application, given that the fundamental thermodynamic limit is 29.4%.[99] Therefore, the potential for significant efficiency increase with silicon technologies is relatively limited. In this context, the prospect of very high efficiencies offered by tandem solar cells including perovskite sub-cells is highly attractive for the industry. In 2018, Oxford PV demonstrated a perovskite-Si tandem cell with 28.0% efficiency, and claim to have a roadmap to achieve a practical limit ~33%.[100] One of the appealing features of the perovskite-Si tandem approach is that, instead of competing with cost-effective, well-established technologies, it can be made compatible with existing production lines. Therefore, companies like Oxford PV design their tandem cells to be built on top of commercial 156x156 mm^2 solar cells. The success of the manufacturing challenge will depend on the ability to devise processes using available tools and compatibility with existing module productions processes.

Therefore, partnerships with established production line equipment manufacturers, as well as joint development agreements with leaders in the solar industry will be important enablers in the commercialisation of perovskite/silicon tandem modules.

2.15 Reliability

To achieve the reliability required to enter a mature market like silicon PV, perovskite tandem technology faces a number of challenges, which are not dissimilar to those that this industry had to overcome in the last decades. The stability of silicon modules has progressed to the level that today's manufacturers offer typically 25 years warranties, which means that the solar modules will still generate about 80-85% of their initial power output after 25 years. To qualify modules, standardised accelerated aging tests have been developed, like the IEC61215 tests which are widely adopted by the industry. Built on silicon solar cells, current standardized test protocols also apply to perovskite/Si tandem modules, but further research is still required to identify degradation modes that may be specific to perovskites. If these are not revealed by the current accelerated testing standards, additional tests should be included, following the example of the potential induced degradation (PID) probing tests that were introduced in 2015 in IEC protocols. It is worth noting that silicon manufacturers often set their

internal targets to higher stress levels (typically 2-3 times) than the requirements for standard certification.

2.16 Scalability

The other major challenge that commercialisation contenders face is scalability. Even for non-utility applications, solar cells need to be integrated into modules which can take very different shapes depending on the fabrication techniques and end use. For example, flexible and lightweight modules carry potential for new applications in portable devices, transport or building-integrated PV, but come with additional constraints such as the mechanical properties of the substrates and, in most cases, preventing the use of glass which is an outstandingly low cost, transparent encapsulation material. For perovskite/Si tandems, the most obvious approach, which is adopted by the current commercialisation contenders, is to achieve compatibility with the silicon solar cells format (~156x156 cm^2, 'M2'). This strategy has the advantage of building on decades of optimisation of interconnection and encapsulation processes and materials, and the availability of large-scale production tools. The choice of the right materials and technologies is crucial for a fast market entry. Since 2016, Oxford PV has been converting a former thin-film manufacturing facility in Germany into a pilot line for the fabrication of perovskite/silicon modules following this general approach.[100]

Technical challenges associated with the increase of the solar cell area are mostly due to the homogeneity of the thin films, and are likely to be solved by engineering appropriate deposition processes. A variety of large-area coating techniques have been demonstrated, including solution phase (slot-die coating, ink-jet printing, etc.) and gas phase deposition method. The latter are usually favoured for perovskite/silicon monolithic tandems, since they are compatible with the fully textured wafers usually required for efficient light absorption in the silicon cell.

Thin-film multi-junction modules (*e.g.* PVK/PVK, PVK/CIGS, PVK/PVK/PVK) face scalability challenges from a slightly different perspective. While they carry the potential for much higher efficiencies than perovskite/Si tandems, they also offer more flexibility in terms of module design. However, for an early entry into the market, adoption of manufacturing tools and processes developed for the silicon PV industry will be of high importance. It is worth noting that series resistance can be a major challenge for thin-film modules, while perovskite/Si monolithic tandems benefit from an excellent back contact (the silicon cell), established TCO materials, and deposition processes for the front contact adopted from heterojunction silicon cell technology.

2.17 Cost

Perovskite multi-junction technology will only be adopted at the utility scale if it delivers its promise of reduced LCOE via increased energy yields. As of 2020, all companies with activities towards the commercialisation of such technologies are pre-revenue, and therefore need to propose a viable business model to secure capital investment. In a recent review, Ballif et al. discussed technoeconomic aspects of the commercialisation of monolithic perovskite/silicon tandem cells.[101] They considered the number of process steps required in addition to the fabrication of the bottom silicon cell, which excludes, for example, metallisation and encapsulation steps, assumed to be common to both technologies. Considering investment depreciation, consumables and operational costs, they estimate that, for instance, with a 4% increase in absolute efficiency requiring 4 additional processing steps, the total additional cost of processing is about 10.4 €/m^2. In this scenario, the total tandem module production costs are almost on par with a crystalline silicon module. In addition, the corresponding area-related BoS savings with respect to an 18% efficient silicon module are 2.7 €-cents/W_p and 6.4 €cts/W_p for utility scale and roof top installations respectively. This shows that even if in the short-term it will be difficult to compete with the steadily decreasing production costs of crystalline silicon modules, the additional savings on area-

related BoS costs will allow a considerably lower cost of ownership, particularly when BoS costs are high, such as in roof top installations.

Detailed cost analyses have been carried out for mechanically-stacked 4T perovskite/silicon modules[102] as well as thin-film perovskite multi-junction modules,[103] and all highlight great commercial potential. Therefore, it is not surprising that several companies (*e.g* Oxford PV, TandemPV, Swift Solar) and industrial/academic initiatives (*e.g.* Solliance) are currently actively attempting to bring perovskite tandem modules to the market in the near future.

2.18 Outlook

In this section, we provide some brief suggestions on avenues of priority that will enable the creation of tandems of over 30% efficiency. Perovskite-on-silicon tandems have already reached 29% PCE, and 30% is not much farther. The tandem current densities predicted by optical simulations for untextured substrates (~19.5 mA/cm^2) have already been achieved. Keeping the short-circuit current from a high-performance silicon cell as the benchmark (42.3 mA/cm^2)[98], we can estimate 21.1 mA/cm^2 as a safe upper limit for achievable tandem current. We suggest that the main gains to be made are in the voltage. The 1.65 eV bandgap mixed halide composition are relatively photo-stable (with respect to halide segregation). Unlike higher bromide compositions, they also show low trap densities, as illustrated by high photoluminescence quantum yields. If

recombination is further reduced via passivation, or the right choice of transport materials, this represents the most straightforward way to break the 30% barrier.

Perovskite-perovskite tandems are limited by the current poor performance of both wide bandgap (> 1.65 eV) and low bandgap (< 1.35 eV) absorber materials. To increase the efficiency of all-perovskite tandems, the open-circuit voltage of the wide-gap cell needs to be improved as a matter of urgency (see chapter 5 and chapter 6). High bromide (>40%) mixed-halide thin-films have high trap densities, which causes a large bulk of the recombination loss. The loss is further aggravated by interfacial recombination at the perovskite-transport layer heterojunctions. Improved deposition techniques need to be found, and new charge transport materials with low interfacial recombination and high selectivity need to be investigated. The goal should be to make the 1.8 eV bandgap cell electronically on par with the best 1.6 eV bandgap cells (~100 mV loss), yielding a V_{OC} of >1.4 V. Lead-tin cells already perform well electronically (V_{OC} > 0.85 V), but waste significant amounts of photons due to shallow absorption onset of the lead-tin perovskite. Thicker layers (~1000 nm) with suitable diffusion lengths are required to achieve a steep absorption onset. Layer thicknesses also need to be carefully tuned to avoid the omnipresent reflection losses due to the large number of layers (see chapter 7). With such improvements, a current of 34 mA/cm^2 is within reach, allowing a matched tandem current of 17 mA/cm^2. A combination of these two improvements—wide-bandgap cell V_{OC} > 1.4 V and low bandgap cell J_{SC} > 34

mA/cm^2 —will allow the 30% barrier to be broken for perovskite-perovskite tandems.

2.19 References

1. Mitzi, D. B. Synthesis, Structure, and Properties of Organic-Inorganic Perovskites and Related Materials. in 1–121 (2007). doi:10.1002/9780470166499.ch1.
2. Xing, G. *et al.* Long-Range Balanced Electron- and Hole-Transport Lengths in Organic-Inorganic CH3NH3PbI3. *Science (80-.).* **342**, 344–347 (2013).
3. Stolterfoht, M. *et al.* Visualization and suppression of interfacial recombination for high-efficiency large-area pin perovskite solar cells. *Nat. Energy* **3**, 847–854 (2018).
4. Stranks, S. D. *et al.* Electron-Hole Diffusion Lengths Exceeding 1 Micrometer in an Organometal Trihalide Perovskite Absorber. *Science (80-.).* **342**, 341–344 (2013).
5. Best Research-Cell Efficiency Chart. https://www.nrel.gov/pv/cell-efficiency.html.
6. Li, Z. *et al.* Scalable fabrication of perovskite solar cells. *Nat. Rev. Mater.* **3**, 18017 (2018).
7. Fu, Y. *et al.* Metal halide perovskite nanostructures for optoelectronic applications and the study of physical properties. *Nat. Rev. Mater.* **4**, 169–188

(2019).

8. Brenner, T. M., Egger, D. A., Kronik, L., Hodes, G. & Cahen, D. Hybrid organic—inorganic perovskites: low-cost semiconductors with intriguing charge-transport properties. *Nat. Rev. Mater.* **1**, 15007 (2016).
9. Xiang, W. & Tress, W. Review on Recent Progress of All-Inorganic Metal Halide Perovskites and Solar Cells. *Adv. Mater.* **31**, 1902851 (2019).
10. ITRPV. *International Technology Roadmap for Photovoltaic (10th edition)*. (2019).
11. Fraunhofer Institute for Solar Energy Systems ISE. Photovoltaics Report. https://www.ise.fraunhofer.de/content/dam/ise/de/documents/publications/studies/Photovoltaics-Report.pdf (2019).
12. Shockley, W. & Queisser, H. J. Detailed Balance Limit of Efficiency of p-n Junction Solar Cells. *J. Appl. Phys.* **32**, 510–519 (1961).
13. Bedair, S. M., Lamorte, M. F. & Hauser, J. R. A two-junction cascade solar-cell structure. *Appl. Phys. Lett.* **34**, 38–39 (1979).
14. Geisz, J. F. *et al.* Six-junction III–V solar cells with 47.1% conversion efficiency under 143 Suns concentration. *Nat. Energy* (2020) doi:10.1038/s41560-020-0598-5.
15. Shah, A. . *et al.* Material and solar cell research in microcrystalline silicon. *Sol. Energy Mater. Sol. Cells* **78**, 469–491 (2003).
16. Schmidtke, J. Commercial status of thin-film photovoltaic devices and

materials. *Opt. Express* **18**, A477 (2010).

17. Nishiwaki, S., Siebentritt, S., Walk, P. & Ch. Lux-Steiner, M. A stacked chalcopyrite thin-film tandem solar cell with 1.2 V open-circuit voltage. *Prog. Photovoltaics Res. Appl.* **11**, 243–248 (2003).

18. Essig, S. *et al.* Raising the one-sun conversion efficiency of III–V/Si solar cells to 32.8% for two junctions and 35.9% for three junctions. *Nat. Energy* **2**, 17144 (2017).

19. Hirst, L. C. & Ekins-Daukes, N. J. Fundamental losses in solar cells. *Prog. Photovoltaics Res. Appl.* **19**, 286–293 (2011).

20. Markvart, T. From steam engine to solar cells: can thermodynamics guide the development of future generations of photovoltaics? *Wiley Interdiscip. Rev. Energy Environ.* **5**, 543–569 (2016).

21. Tiedje, T., Yablonovitch, E., Cody, G. D. & Brooks, B. G. Limiting efficiency of silicon solar cells. *IEEE Trans. Electron Devices* **31**, 711–716 (1984).

22. Pazos-Outón, L. M., Xiao, T. P. & Yablonovitch, E. Fundamental Efficiency Limit of Lead Iodide Perovskite Solar Cells. *J. Phys. Chem. Lett.* **9**, 1703–1711 (2018).

23. Nayak, P. K., Mahesh, S., Snaith, H. J. & Cahen, D. Photovoltaic solar cell technologies: analysing the state of the art. *Nat. Rev. Mater.* **4**, 269–285 (2019).

24. Green, M. A. Third Generation Photovoltaics : Advanced Solar Energy

Conversion. (2006).

25. Hörantner, M. T. & Snaith, H. J. Predicting and optimising the energy yield of perovskite-on-silicon tandem solar cells under real world conditions. *Energy Environ. Sci.* **10**, 1983–1993 (2017).

26. Warren, E. L. *et al.* A Taxonomy for Three-Terminal Tandem Solar Cells. *ACS Energy Lett.* **5**, 1233–1242 (2020).

27. Warren, E. L. *et al.* A Taxonomy for Three-Terminal Tandem Solar Cells. *ACS Energy Lett.* **5**, 1233–1242 (2020).

28. Warren, E. L. *et al.* Maximizing tandem solar cell power extraction using a three-terminal design. *Sustain. Energy Fuels* **2**, 1141–1147 (2018).

29. Green, M. A., Emery, K., Hishikawa, Y., Warta, W. & Dunlop, E. D. Solar cell efficiency tables (Version 45). *Prog. Photovoltaics Res. Appl.* **23**, 1–9 (2015).

30. Sanehira, E. M. *et al.* Enhanced mobility CsPbI 3 quantum dot arrays for record-efficiency, high-voltage photovoltaic cells. *Sci. Adv.* **3**, eaao4204 (2017).

31. Green, M. A., Emery, K., Hishikawa, Y., Warta, W. & Dunlop, E. D. Solar cell efficiency tables (version 47). *Prog. Photovoltaics Res. Appl.* **24**, 3–11 (2016).

32. Green, M. A. *et al.* Solar cell efficiency tables (version 52). *Prog. Photovoltaics Res. Appl.* **26**, 427–436 (2018).

33. Hörantner, M. T. *et al.* The Potential of Multijunction Perovskite Solar Cells. *ACS Energy Lett.* **2**, 2506–2513 (2017).

34. Meehan, C. NREL Developing Improved Tech to Lower Costs for Multi-Junction Solar Cells. https://www.solarreviews.com/news/Nrel-developing-tech-lower-cost-multi-junction-solar-cells-071918/ (2018).

35. Guchhait, A. *et al.* Over 20% Efficient CIGS-Perovskite Tandem Solar Cells. *ACS Energy Lett.* **2**, 807–812 (2017).

36. Wang, Z. *et al.* High irradiance performance of metal halide perovskites for concentrator photovoltaics. *Nat. Energy* (2018) doi:10.1038/s41560-018-0220-2.

37. Todorov, T. *et al.* Monolithic Perovskite-CIGS Tandem Solar Cells via In Situ Band Gap Engineering. *Adv. Energy Mater.* **5**, 1500799 (2015).

38. Werner, J. *et al.* Efficient Monolithic Perovskite/Silicon Tandem Solar Cell with Cell Area >1 cm 2. *J. Phys. Chem. Lett.* **7**, 161–166 (2016).

39. www.ise.fraunhofer.de. Fraunhofer Institute for Solar Energy Systems ISE. *Fraunhofer Ist. Sol. energy Syst. ISE* 1–42 (2014).

40. Yu, Z., Leilaeioun, M. & Holman, Z. Selecting tandem partners for silicon solar cells. *Nat. Energy* **1**, 16137 (2016).

41. Eperon, G. E., Horantner, M. T. & Snaith, H. J. Metal halide perovskite tandem and multiple-junction photovoltaics. *Nat. Rev. Chem.* **1**, (2017).

42. Werner, J., Niesen, B. & Ballif, C. Perovskite/Silicon Tandem Solar Cells: Marriage of Convenience or True Love Story? - An Overview. *Adv. Mater. Interfaces* **5**, 1700731 (2018).

43. Wang, Z., Song, Z., Yan, Y., Liu, S. (Frank) & Yang, D. Perovskite—a Perfect Top Cell for Tandem Devices to Break the S–Q Limit. *Adv. Sci.* **6**, 1801704 (2019).

44. Song, Z. *et al.* Wide-bandgap, low-bandgap, and tandem perovskite solar cells. *Semicond. Sci. Technol.* **34**, (2019).

45. Lal, N. N. *et al.* Perovskite Tandem Solar Cells. *Adv. Energy Mater.* **7**, 1602761 (2017).

46. Torabi, N. *et al.* Progress and challenges in perovskite photovoltaics from single- to multi-junction cells. *Mater. Today Energy* **12**, 70–94 (2019).

47. Ahmad, W., Khan, J., Niu, G. & Tang, J. Inorganic CsPbI 3 Perovskite-Based Solar Cells: A Choice for a Tandem Device. *Sol. RRL* **1**, 1700048 (2017).

48. Eperon, G. E. *et al.* Inorganic caesium lead iodide perovskite solar cells. *J. Mater. Chem. A* **3**, 19688–19695 (2015).

49. Swarnkar, A. *et al.* Quantum dot-induced phase stabilization of -CsPbI3 perovskite for high-efficiency photovoltaics. *Science (80-.).* **354**, 92–95 (2016).

50. Wang, Y. *et al.* Thermodynamically stabilized β-CsPbI 3 –based perovskite solar cells with efficiencies >18%. *Science (80-.).* **365**, 591–595 (2019).

51. Ke, W., Spanopoulos, I., Stoumpos, C. C. & Kanatzidis, M. G. Myths and reality of HPbI3 in halide perovskite solar cells. *Nat. Commun.* **9**, 4785 (2018).

52. Palmstrom, A. F. *et al.* Enabling Flexible All-Perovskite Tandem Solar Cells. *Joule* **3**, 2193–2204 (2019).

53. McMeekin, D. P. *et al.* A mixed-cation lead mixed-halide perovskite absorber for tandem solar cells. *Science (80-.).* **351**, 151–155 (2016).

54. Yang, T. C.-J., Fiala, P., Jeangros, Q. & Ballif, C. High-Bandgap Perovskite Materials for Multijunction Solar Cells. *Joule* **2**, 1421–1436 (2018).

55. Hoke, E. T. *et al.* Reversible photo-induced trap formation in mixed-halide hybrid perovskites for photovoltaics. *Chem. Sci.* **6**, 613–617 (2015).

56. Brennan, M. C., Draguta, S., Kamat, P. V. & Kuno, M. Light-Induced Anion Phase Segregation in Mixed Halide Perovskites. *ACS Energy Lett.* **3**, 204–213 (2018).

57. Mahesh, S. *et al.* Revealing the origin of voltage loss in mixed-halide perovskite solar cells. *Energy Environ. Sci.* **13**, 258–267 (2020).

58. Köhnen, E. *et al.* Highly efficient monolithic perovskite silicon tandem solar cells: analyzing the influence of current mismatch on device performance. *Sustain. Energy Fuels* **3**, 1995–2005 (2019).

59. Hou, Y. *et al.* Efficient tandem solar cells with solution-processed perovskite on textured crystalline silicon. *Science (80-.).* **367**, 1135–1140 (2020).

60. Fu, F. *et al.* High-efficiency inverted semi-transparent planar perovskite solar cells in substrate configuration. *Nat. Energy* **2**, 16190 (2017).

61. Werner, J. *et al.* Efficient Near-Infrared-Transparent Perovskite Solar Cells Enabling Direct Comparison of 4-Terminal and Monolithic Perovskite/Silicon Tandem Cells. *ACS Energy Lett.* **1**, 474–480 (2016).

62. Mailoa, J. P. *et al.* A 2-terminal perovskite/silicon multijunction solar cell enabled by a silicon tunnel junction. *Appl. Phys. Lett.* **106**, 121105 (2015).

63. Yang, Y. *et al.* Multilayer Transparent Top Electrode for Solution Processed Perovskite/Cu(In,Ga) (Se,S)(2) Four Terminal Tandem Solar Cells. *ACS Nano* **9**, 7714–7721 (2015).

64. Bush, K. A. *et al.* 23.6%-efficient monolithic perovskite/silicon tandem solar cells with improved stability. *Nat. Energy* **2**, 17009 (2017).

65. World Record: Efficiency of perovskite silicon tandem solar cell jumps to 29.15 per cent. *Helmholtz Zentrum Berlin* https://www.helmholtz-berlin.de/pubbin/news_seite?nid=21020;sprache=en;seitenid=72384.

66. Dréon, J. *et al.* 23.5%-efficient silicon heterojunction silicon solar cell using molybdenum oxide as hole-selective contact. *Nano Energy* **70**, 104495 (2020).

67. Mazzarella, L. *et al.* Infrared Light Management Using a Nanocrystalline Silicon Oxide Interlayer in Monolithic Perovskite/Silicon Heterojunction Tandem Solar Cells with Efficiency above 25%. *Adv. Energy Mater.* **9**, 1803241 (2019).

68. Mailoa, J. P. *et al.* A 2-terminal perovskite/silicon multijunction solar cell enabled by a silicon tunnel junction. *Appl. Phys. Lett.* **106**, (2015).

69. Sahli, F. *et al.* Improved Optics in Monolithic Perovskite/Silicon Tandem Solar Cells with a Nanocrystalline Silicon Recombination Junction. *Adv. Energy Mater.* **8**, 1701609 (2018).

70. Sahli, F. *et al.* Fully textured monolithic perovskite/silicon tandem solar cells with 25.2% power conversion efficiency. *Nat. Mater.* **17**, 820–826 (2018).

71. Xu, J. *et al.* Triple-halide wide–band gap perovskites with suppressed phase segregation for efficient tandems. *Science (80-.).* **367**, 1097–1104 (2020).

72. Todorov, T., Gershon, T., Gunawan, O., Sturdevant, C. & Guha, S. Perovskite-kesterite monolithic tandem solar cells with high open-circuit voltage. *Appl. Phys. Lett.* **105**, (2014).

73. Chen, C.-C. *et al.* Perovskite/polymer monolithic hybrid tandem solar cells utilizing a low-temperature, full solution process. *Mater. Horizons* **2**, 203–211 (2015).

74. Albrecht, S. *et al.* Monolithic perovskite/silicon-heterojunction tandem solar cells processed at low temperature. *Energy Environ. Sci.* **9**, 81–88 (2016).

75. Werner, J. *et al.* Efficient Monolithic Perovskite/Silicon Tandem Solar Cell with Cell Area >1 cm 2. *J. Phys. Chem. Lett.* **7**, 161–166 (2016).

76. Eperon, G. E. *et al.* Perovskite-perovskite tandem photovoltaics with optimized band gaps. *Science (80-.).* **354**, 861–865 (2016).

77. Forgács, D. *et al.* Efficient Monolithic Perovskite/Perovskite Tandem Solar Cells. *Adv. Energy Mater.* **7**, 1602121 (2017).

78. Han, Q. *et al.* High-performance perovskite/Cu(In,Ga)Se 2 monolithic tandem solar cells. *Science (80-.).* **361**, 904–908 (2018).

79. Chen, B. *et al.* Grain Engineering for Perovskite/Silicon Monolithic Tandem

Solar Cells with Efficiency of 25.4%. *Joule* **3**, 177–190 (2019).

80. Tong, J. *et al.* Carrier lifetimes of >1 μs in Sn-Pb perovskites enable efficient all-perovskite tandem solar cells. *Science (80-.).* **364**, 475–479 (2019).

81. McMeekin, D. P. *et al.* Solution-Processed All-Perovskite Multi-junction Solar Cells. *Joule* **3**, 387–401 (2019).

82. Lin, R. *et al.* Monolithic all-perovskite tandem solar cells with 24.8% efficiency exploiting comproportionation to suppress Sn(ii) oxidation in precursor ink. *Nat. Energy* **4**, 864–873 (2019).

83. Liu, Z. *et al.* Open-Circuit Voltages Exceeding 1.26 v in Planar Methylammonium Lead Iodide Perovskite Solar Cells. *ACS Energy Lett.* **4**, 110–117 (2019).

84. Mahesh, S. *et al.* Revealing the Origin of Voltage Loss in Mixed-Halide Perovskite Solar Cells. *Energy Environ. Sci.* **50**, 675 (2019).

85. Hoke, E. T. *et al.* Reversible photo-induced trap formation in mixed-halide hybrid perovskites for photovoltaics. *Chem. Sci.* **6**, 613–617 (2015).

86. Li, C. *et al.* Reducing Saturation-Current Density to Realize High-Efficiency Low-Bandgap Mixed Tin-Lead Halide Perovskite Solar Cells. *Adv. Energy Mater.* **9**, 1803135 (2019).

87. Zhao, D. *et al.* Low-bandgap mixed tin–lead iodide perovskite absorbers with long carrier lifetimes for all-perovskite tandem solar cells. *Nat. Energy* **2**, 17018 (2017).

88. Xu, G. *et al.* Integrating Ultrathin Bulk-Heterojunction Organic Semiconductor Intermediary for High-Performance Low-Bandgap Perovskite Solar Cells with Low Energy Loss. *Adv. Funct. Mater.* **28**, 1804427 (2018).

89. Prasanna, R. *et al.* Design of low bandgap tin–lead halide perovskite solar cells to achieve thermal, atmospheric and operational stability. *Nat. Energy* **4**, 939–947 (2019).

90. Werner, J. *et al.* Efficient Monolithic Perovskite/Silicon Tandem Solar Cell with Cell Area >1 cm 2. *J. Phys. Chem. Lett.* **7**, 161–166 (2016).

91. Ávila, J. *et al.* High voltage vacuum-deposited CH3NH3PbI3-CH3NH3PbI3 tandem solar cells. *Energy Environ. Sci.* **11**, 0–8 (2018).

92. Meusel, M. *et al.* Spectral response measurements of monolithic GaInP/Ga(In)As/Ge triple-junction solar cells: Measurement artifacts and their explanation. *Prog. Photovoltaics Res. Appl.* **11**, 499–514 (2003).

93. Meusel, M., Adelhelm, R., Dimroth, F., Bett, A. W. & Warta, W. Spectral mismatch correction and spectrometric characterization of monolithic III-V multi-junction solar cells. *Prog. Photovoltaics Res. Appl.* **10**, 243–255 (2002).

94. *Test Methods for Measurement of Electrical Performance and Spectral Response of Nonconcentrator Multijunction Photovoltaic Cells and Modules*. *ASTM International* doi:10.1520/E2236-10R19.

95. Timmreck, R. *et al.* Characterization of tandem organic solar cells. *Nat.*

Photonics **9**, 478–479 (2015).

96. Pravettoni, M. & Mullejans, H. A method for the detection and quantitative estimation of low shunt resistances via the dark spectral response measurement of multijunction photovoltaic cells: Theory and results. in *2011 37th IEEE Photovoltaic Specialists Conference* 001726–001730 (IEEE, 2011). doi:10.1109/PVSC.2011.6186287.

97. LONGi Solar sets new bifacial mono-PERC solar cell world record at 24.06 percent. https://en.longi-solar.com/home/events/press_detail/id/89.html (2019).

98. Yoshikawa, K. *et al.* Silicon heterojunction solar cell with interdigitated back contacts for a photoconversion efficiency over 26%. *Nat. Energy* **2**, 17032 (2017).

99. Richter, A., Hermle, M. & Glunz, S. W. Reassessment of the Limiting Efficiency for Crystalline Silicon Solar Cells. *IEEE J. Photovoltaics* **3**, 1184–1191 (2013).

100. Case, C., Beaumont, N. & Kirk, D. Industrial Insights into Perovskite Photovoltaics. *ACS Energy Lett.* **4**, 2760–2762 (2019).

101. Werner, J., Niesen, B. & Ballif, C. Perovskite/Silicon Tandem Solar Cells: Marriage of Convenience or True Love Story? - An Overview. *Adv. Mater. Interfaces* **5**, 1700731 (2018).

102. Mathews, I. *et al.* Economically Sustainable Growth of Perovskite Photovoltaics Manufacturing. *Joule* (2020) doi:10.1016/j.joule.2020.01.006.

103. Li, Z. *et al.* Cost Analysis of Perovskite Tandem Photovoltaics. *Joule* **2**, 1559–1572 (2018).

104. Yu. D. *et al.* Multi-photon quantum cutting in $Gd_2O_2S:Tm^{3+}$ to enhance the photo-response of solar cells. *Light Sci Appl* **4**, e344 (2015)

3

Thermodynamics and Optical Modelling

3.1 Overview

A full appreciation of the working of a non-ideal solar cell requires a great deal of physics that can deal with the complex processes of generation, transport, and recombination of carriers. This is often simulated numerically by combining an optical generation model (often the transfer matrix method for thin-film solar cells) with drift-diffusion equations for transport. A drift-diffusion model requires detailed information about material properties— mobilities, energy levels, doping densities, recombination rate constants, trap densities, interface recombination velocities and more. This is not a luxury usually available to incipient PV technologies. The situation, however, is not so complicated for ideal solar cells, where thermodynamics is sufficient to entirely predict performance. After a decade of development, the flagship 1.6 eV bandgap perovskite solar cells now exhibit radiative efficiencies $\sim 1 - 10\%$, a regime which opens up the possibility of

using thermodynamics as a powerful probe of cell physics. As perovskite solar cells are planar thin-film stacks, their optical response can be modelled quite well using the transfer matrix method. As these topics are frequently referred to in this thesis, a concise exposition is provided here, assuming knowledge of undergraduate optics and semiconductor physics. The interested reader is referred to the publications of Tom Markvart[1–3], Thomas Kirchartz[4–11], Uwe Rau[4,5,7–14], Peter Wurfel[15] and Martin Green[16–23] for more detailed discussion on solar cell thermodynamics.

3.2 Solar Cell Thermodynamics

3.2.1 The Solar Spectrum

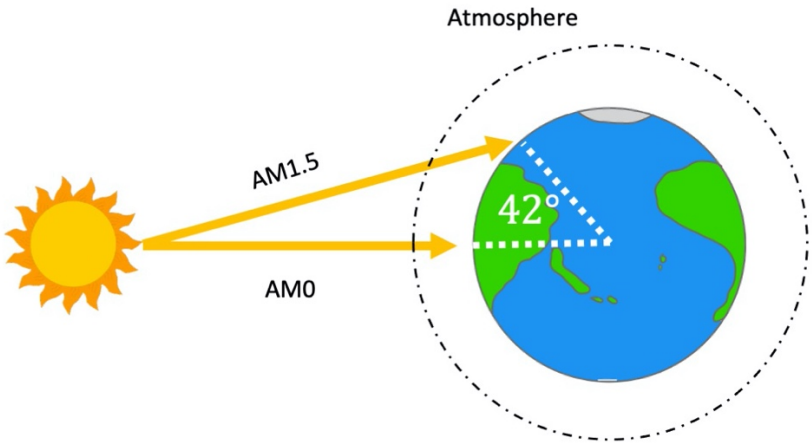

Figure 3.1 | The concept of Air Mass.

Power conversion efficiency is not an intrinsic property of a photovoltaic cell. This is because it depends on the incident light spectrum. Photovoltaic cells, being subject to thermalisation loss, do not convert all wavelengths with the same efficiency. The multi-junction PV concept attempts to correct this inequity by introducing multiple absorbers, each specialising in a range of wavelengths. Because of this spectral dependence, a full characterisation of the solar spectrum is important before a thermodynamic analysis of PV cells can be taken up.

The radiation from the sun closely resembles a perfect blackbody radiator at a temperature $T_S = 6000K$, i.e. it follows the Planck distribution:

$$n_s(E) = \frac{2}{h^3 c^2} \frac{E^2}{exp(E/k_B T_s) - 1} \qquad 3.1$$

Here n_s is the flux of photons emitted by the blackbody per energy interval and k_B is the Boltzmann constant. When measured on earth, however, the solar spectrum is found superposed with the absorption features of molecules in the sun, and in the earth's atmosphere. For instance, much of the UV spectrum is filtered by the ozone layer. Furthermore, the absorption peaks of water and carbon dioxide can be seen dips in the infrared region. Hence, this attenuation is quantified by defining the air mass factor (AM), as the ratio of the path length taken by sunlight through to the atmosphere, to the path length if the sun were to be directly overhead. In other terms:

$$AM = cosec\ (\psi_{sun}) \qquad 3.2$$

Here, ψ_{sun} is the solar elevation angle (see figure 3.1). The National Renewable Energy Lab (NREL) provides a standard spectrum[24], the Air Mass 1.5 spectra (AM1.5), which is widely used in the PV community. The AM1.5 spectrum is based on terrestrial radiation measured at an angle equivalent to central United States ($\cos\theta = \frac{1}{1.5}$). For convenience, the power in this standardised AM1.5 spectrum has been set to 1000W/m^2. While the Planck black-body spectrum allows convenient analytical solutions to thermodynamic models, it introduces significant error in the current calculated by optical models. All the simulations presented in this text use the AM1.5 spectrum.

3.2.2 Detailed Balance Calculations

How efficient can a photovoltaic cell be? Shockley and Queisser answered this question conclusively by applying the concept of detailed balance to PV cells[9,25]. According to detailed balance, at thermal equilibrium, every photon absorption event must be balanced by a photon emission event, with this balance valid at every energy and solid angle. Photovoltaic cells in operation are clearly not in thermal equilibrium. However, Shockley and Queisser realised that thermal emission away from equilibrium only differs from equilibrium emission by a scaling factor that scales exponentially with the quasi fermi level splitting. This insight is the cornerstone of the thermodynamics of photovoltaic cells. With this insight, Shockley and Queisser calculated the limiting thermodynamic efficiency

for PV cells, assuming a step function absorption ("Shockley Quiesser limit"). SQ analysis reveals that PV cells can be at best 33% efficient (under unconcentrated light), and that this efficiency occurs at a bandgap of 1.33 eV. At this bandgap, thermalisation loss and below-bandgap photon loss reach a compromise, yielding the highest efficiency. Here, we briefly derive and explain a modified version of the Shockley-Queisser (SQ) calculation that also accepts non-step function absorption spectra. Such calculations are said to be performed in the "radiative limit", since all the electrons and holes are assumed to recombine radiatively.

Consider a solar cell at equilibrium with its surroundings at temperature T. We made the following assumptions:

1. The active layer of the solar cell is a single semiconductor layer sandwiched between contacts that perfectly select electrons and holes respectively.
2. A single e-h hole pair is created for each absorbed photon.
3. Each e-h pair contributes to the short-circuit current of the solar cell.
4. The mobility of the carriers is infinite. In other words, there is no spatial gradient in the chemical potentials of electrons and holes.
5. Electrons and holes can only recombine radiatively.

Note that despite being in the "dark," every unit area of the semiconductor is still absorbing $\phi_{abs}(E)$ blackbody photons every second from an energy interval of dE around E:

$$\phi_{abs}(E) = \phi_{BB}(E) \cdot A(E) = \frac{2\pi}{c^2 h^3} \frac{A(E) \cdot E^2 dE}{exp(E/k_B T) - 1} \quad 3.3$$

Here, $A(E)$ is the absorptance of the active layer. Since the cell is in thermal equilibrium with its surroundings, the same flux is also continuously re-emitted, per the dictate of detailed balance. Once the cell is irradiated with sunlight, the thermal equilibrium is disturbed. The electron and hole quasi fermi levels are now separated by a chemical potential qV. In this scenario, the generalised Planck's law, which was rigorously established by Wurfel[26,27], predicts the re-emitted photon flux:

$$\phi_{em}(E) = \frac{2\pi}{c^2 h^3} \frac{A(E) \cdot E^2 dE}{exp\big((E - qV)/k_B T\big) - 1} \quad 3.4$$

As we noted previously, when illuminated, the cell emission is approximately equal to the equilibrium black-body emission times a scaling factor $e^{\frac{qV}{k_B T}}$. With this idea in place, it is now a straightforward task to derive the current voltage characteristic of the cell. The idea underpinning the derivation is this: any electron-hole pairs that do not contribute to current must be re-emitted out of the cell, since there is only radiative recombination in the cell.

Let the cell have an absorptance $A(E)$, which results in a short-circuit current density J_{SC} under AM1.5 illumination. If the cell is now kept at a bias voltage V, the extracted current density will be a value $J(V) < J_{SC}$. By the previously explained idea, the "deficit" current density $J_{SC} - J(V)$ will have to be emitted out to the ambient as photons. Therefore, using generalised Planck's law:

$$J_{SC} - J(V) = q \int_0^\infty \phi_{em}(E) \cdot dE \tag{3.5}$$

In the visible spectrum, $E \gg kT$. Hence, this can be simplified to:

$$J_{SC} - J(V) = e^{\frac{qV}{k_B T}} \int_0^\infty q \cdot \phi_{BB}(E) \cdot A(E) \cdot dE \tag{3.6}$$

The integral is none other than the dark saturation current J_0 which appears in the Shockley diode equation. In fact, we have managed to recover the Shockley diode equation via detailed balance:

$$J(V) = J_{SC} - J_0 e^{\frac{qV}{k_B T}} \tag{3.7}$$

The term $J_0 e^{\frac{qV}{k_B T}}$ is the photon "current" being emitted to the ambient. With this derivation, the strong temperature dependence $\left(\propto T^3 e^{\frac{qE_g}{kT}}\right)$ of the dark saturation current also stands clarified: it is rooted in the Planck equation. By writing the short-circuit current density J_{SC} in terms of the AM1.5 photon flux $\phi_{AM1.5}(E)$ and the absorptance $A(E)$, we can arrive at:

$$J(V) = \int_0^\infty q \cdot \phi_{AM1.5}(E) \cdot A(E) \cdot dE \; - e^{\frac{qV}{k_B T}} \int_0^\infty q \cdot \phi_{BB}(E) \cdot A(E) \cdot dE \tag{3.8}$$

Therefore, when the previously delineated assumptions hold, the solar cell characteristics are completely determined once the active layer absorptance $A(E)$ is known.

3.2.3 Intrinsic Loss Mechanisms

The photovoltaic cell is only one of the many possible machines for converting solar energy into work. How efficient can the abstract solar converter be? The

answer lies in the realisation that solar converters are essentially heat engines with the sun ($T_S = 6000K$) and the solar converter ($T_A = 300K$) as the source and the sink respectively. In this case, we could expect solar converters to be limited by the Carnot efficiency[34]:

$$\eta_{\text{carnot}} = 1 - \frac{\mathrm{T_A}}{T_S} = 95\% \qquad 3.9$$

However, there is additional complexity at work here—since radiative transfer is involved, the cell too emits back blackbody photons towards the sun. Thus, there is also an efficiency of energy transfer to be included. After including all these effects, Landsberg showed that the upper limit to efficiency occurs in conversion devices that absorb radiation from the sun without creating entropy[28]. A Landsberg engine gives off the entropy absorbed with solar radiation in two ways. A part is emitted back to the sun together with blackbody radiation. The remaining entropy goes to a heat reservoir at the ambient temperature, also losing some energy in the process. With these assumptions, we can derive the Landsberg efficiency by balancing the energy and entropy currents[28]:

$$\eta_L = 1 - \frac{T_A^4}{T_S^4} - \frac{4}{3}\frac{T_0}{T_S}\left(1 - \frac{T_A^3}{T_S^3}\right) \qquad 3.10$$

Here, T_A, T_0 and T_S are the temperatures of the converter, the ambient and the sun respectively. This yields a maximum conversion efficiency of 93.3%. This is the absolute upper bound efficiency for solar energy conversion.

As we have seen, detailed balance predicts much lower limiting efficiencies for photovoltaic converters: 33% for unconcentrated sunlight, and 41% under

concentration[9,25]. This arises from the semiconducting nature of the photovoltaic absorber, which introduces several new entropy generating mechanisms. If the SQ calculation is performed analytically by modelling solar emission as Planckian, the penalties from each loss mechanism can be separately quantified[29,30]. This can inform us about the relative contributions of each mechanism and provide insight into the design of new converters that circumvent one or more of these losses.

We start by calculating the short-circuit current density that that absorbed solar photons can generate on earth. If we assume Planckian emission from the Sun ($T_S = 6000K$), and a step-function absorptance at $E = E_g$, we can perform the following integral to calculate J_{SC} [25]:

$$J_{SC} = q \int_{E_g}^{\infty} \frac{2\Omega_{in}}{h^3 c^2} \frac{E^2 \cdot dE}{e^{\left(\frac{E}{k_B T_S}\right)} - 1} \qquad 3.11$$

Here, $\Omega_{in} (= 6.807 \times 10^{-5}\ sr)$ is the solid angle subtended by the sun on the earth's surface. To calculate the photon current emitted by a cell in operation, we integrate generalised Planck's law[26,27]:

$$J_{em} = q \int_{E_g}^{\infty} \frac{2\Omega_{out}}{h^3 c^2} \frac{E^2 \cdot dE}{e^{\left(\frac{E-qV}{k_B T_A}\right)} - 1} \qquad 3.12$$

Here T_A is the ambient temperature, $\Omega_{out} (= 2\pi)$ is the solid angle of the hemispherical re-emission from the cell, and qV is the quasi fermi level splitting in the absorber. According to detailed balance, when $V = V_{OC}$, the number of photons absorbed must be equal to the number of photons emitted. Therefore:

$$J_{SC} = q\int_{E_g}^{\infty} \frac{2\Omega_{in}}{h^3c^2}\,\frac{E^2\cdot dE}{e^{\left(\frac{E}{k_BT_S}\right)}-1} = q\int_{E_g}^{\infty} \frac{2\Omega_{out}}{h^3c^2}\,\frac{E^2\cdot dE}{e^{\left(\frac{E-qV_{OC}}{k_BT_A}\right)}-1} = J_{em} \qquad 3.13$$

The -1 in the denominators can be neglected since $e^{\frac{E_g}{kT_S}} \gg 1$ for most solar cell materials, yielding:

$$e^{\left(\frac{qV_{OC}}{k_BT_A}\right)} = \frac{\Omega_{in}\int_{E_g}^{\infty} E^2 e^{\left(\frac{-E}{k_BT_S}\right)}\,dE}{\Omega_{out}\int_{E_g}^{\infty} E^2 e^{\left(\frac{-E}{k_BT_A}\right)}\,dE} \qquad 3.14$$

Integrating the numerator and denominator using integration by parts gives us[29]:

$$exp\,(\frac{qV_{OC}}{k_BT_A}) = \frac{\Omega_{in}\left(E_g^2k_BT_se^{\left(\frac{-E_g}{k_BT_S}\right)} - 2E_gk_B^2T_S^2e^{\left(\frac{-E_g}{k_BT_S}\right)} - 2k_B^3T_S^3e^{\left(\frac{-E_g}{k_BT_S}\right)}\right)}{\Omega_{out}\left(E_g^2k_BT_Ae^{\left(\frac{-E_g}{k_BT_A}\right)} - 2E_gk_B^2T_A^2e^{\left(\frac{-E_g}{k_BT_A}\right)} - 2k^3T_A^3e^{\left(\frac{-E_g}{k_BT_A}\right)}\right)} \qquad 3.15$$

$$e^{\left(\frac{qV_{OC}}{k_BT_A}\right)} = \left(\frac{\Omega_{in}}{\Omega_{out}}\right)\frac{\left(E_g^2 - 2E_gk_BT_S - 2k_B^2T_S^2\right)k_BT_s}{\left(E_g^2 - 2E_gk_BT_A - 2k_B^2T_A^2\right)k_BT_A}\left(e^{\left(\frac{E_g}{k_BT_A}-\frac{E_g}{k_BT_S}\right)}\right) \qquad 3.16$$

$$e^{\left(\frac{qV_{OC}}{k_BT_A}\right)} = \left(\frac{\Omega_{in}}{\Omega_{out}}\right)\frac{\left(E_g^2 - 2E_gk_BT_S - 2k_B^2T_S^2\right)k_BT_s}{\left(E_g^2 - 2E_gk_BT_A - 2k_B^2T_A^2\right)k_BT_A}\left(e^{\frac{E_g}{k_BT_A}\left(1-\frac{T_A}{T_S}\right)}\right) \qquad 3.17$$

$$qV_{OC} = kT_Aln\left(\frac{\Omega_{in}}{\Omega_{out}}\right) + k_BT_Aln\frac{k_BT_s\left(E_g^2 - 2E_gk_BT_S - 2k_B^2T_S^2\right)}{k_B\,T_A\left(E_g^2 - 2E_gk_BT_A - 2k_B^2T_A^2\right)} + E_g\left(1-\frac{T_A}{T_S}\right) \qquad 3.18$$

$$qV_{OC} = E_g\left(1-\frac{T_A}{T_S}\right) - k_BT_Aln\left(\frac{\Omega_{out}}{\Omega_{in}}\right) + k_BT_Aln\frac{T_s\left(E_g^2 - 2E_gk_BT_S - 2k_B^2T_S^2\right)}{T_A\left(E_g^2 - 2E_gk_BT_A - 2k_B^2T_A^2\right)} \qquad 3.19$$

This finally yields an equation that expresses the open-circuit voltage as a function of various physical quantities[29]:

$$qV_{OC} = E_g\left(1-\frac{T_A}{T_S}\right) + k_BT_Aln\left(\frac{\gamma\left(E_g,T_s\right)}{\gamma\left(E_g,T_A\right)}\right) - k_BT_Aln\left(\frac{\Omega_{out}}{\Omega_{in}}\right) \qquad 3.20$$

Here $\gamma = T(E^2 - 2kTE - 2k^2T^2)$. Loss mechanisms can be individually identified in this expression for the open circuit voltage[29,30]. The term E_g is the

result of the limitation imposed by carrier thermalisation to the band-edge. The term $\left(1-\frac{T_A}{T_S}\right)$ represents the Carnot loss[34]. The term $k_B T_A ln\left(\frac{\Omega_{out}}{\Omega_{in}}\right)$ arises from the étendue expansion between the incident sunlight and photon re-emission from the solar cell[35]. The term $k_B T_A ln\left(\frac{\gamma(E_g,T_S)}{\gamma(E_g,T_A)}\right)$ describes an increase in the free energy per carrier as a result of the mismatch between the temperatures of the absorbed and emitted photon distributions[29]. The SQ treatment also assumes a step-function bandgap. However, the absorption tails of real cells have a finite slope, which increases the thermalisation loss. This is termed *radiative loss* and can be quantified as the difference of the SQ and radiative open-circuit voltages[30].

Taken together, these (thermalisation loss, Carnot loss, étendue expansion loss and radiative loss) represent the intrinsic loss mechanisms at work in single-junction photovoltaic devices. They cannot be overcome without breaking the assumptions of the detailed balance calculation. The multijunction PV cell reduces thermalisation loss by breaking the SQ assumption of a single absorbing layer.

3.2.4 Importance of Luminescence Extraction

In real solar cells, only a small fraction (<10%) of the total recombination is radiative. To account for this, we correct the previously calculated radiative limit J_0 by defining a scaling factor called the external electroluminescence efficiency EQE_{EL}. $EQE_{EL}$is defined as the probability that an e-h pair injected into the device that will result in the external emission of a photon. In other words, it is the

fraction of the total recombination in the device that results in photon emission to the ambient:

$$EQE_{EL} = \frac{J_{0,rad}}{J_{0,rad} + J_{non-rad}} \quad 3.21$$

Here, $J_{0,rad}$ is the dark saturation current calculated in the radiative limit. Naturally, EQE_{EL} is dependent on the hole and electron concentrations. This definition allows us to write the recombination current J_0 in terms of the calculable radiative recombination current $J_{0,rad}$[37]:

$$J_0 = \frac{J_{0,rad}}{EQE_{EL}} \quad 3.22$$

The EQE_{EL} of a solar cell can easily be measured in an integrating sphere by injecting a current density comparable to the short-circuit current density under AM1.5 illumination. In summary, we have arrived at the following equations for the JV response of a PV cell:

$$J_{SC} = q \int_{E_g}^{\infty} EQE_{PV}(E) \cdot \phi_{AM1.5}(E) \cdot dE \quad 3.23$$

$$J_{0,rad} = q \int_{E_g}^{\infty} EQE_{PV}(E) \cdot \phi_{BB}(E) \cdot dE \quad 3.24$$

$$J(V) = J_{SC} - \frac{J_{0,rad}}{EQE_{EL}} e^{\frac{qV}{k_B T}} \quad 3.25$$

Under open-circuit, the following relationship is obtained[36]:

$$V_{OC} = V_{OC,rad} + \frac{k_B T}{q} ln\,(EQE_{EL}) \quad 3.26$$

Here, $V_{OC,rad}$ is the open-circuit voltage calculated in the radiative limit, i.e. the thermodynamically limiting V_{OC}, given a certain active layer absorptance. This

relationship tells us that the EQE_{EL} is a measure of the V_{OC} loss arising from non-radiative recombination. In quantitative terms, every order of magnitude drop in the EQE_{EL} corresponds to a V_{OC} penalty of $\frac{k_B T}{q}\ln(10) = 59.5\, mV$. In qualitative terms, this suggests that more photoluminescent a cell is, higher the V_{OC}, and better the PV performance. In other words, the better a cell is at emitting photons, the better its PV performance. In some ways, this is a paradox, as emitted photons cannot contribute to PV performance. This paradox is resolved by noting that the though emitted photons are lost, they serve as a gauge of the electronic and optical losses in the system. High luminescence from a cell suggests a high-carrier density inside the cell, which results in a high open-circuit voltage. The AltaDevices GaAs solar cell that currently holds the single-junction efficiency record (29.1%)[31] was made possible by this idea. Both non-radiative recombination and parasitic absorption were nearly eliminated by using luminescence as a probe of cell quality. However, achieving near-unity external luminescence efficiency is not easy. Maximising external emission requires the simultaneous optimisation of both electronics (i.e. non-radiative recombination) and optics (i.e. light trapping and parasitic absorption). Consider a photon that has been re-emitted in a random direction inside the semiconductor absorber. Because the semiconductor typically has a high refractive index, the photon will undergo a series of re-absorptions and total internal reflections ("photon recycling") before it may acquire the right orientation to escape the semiconductor. For the relatively

large refractive indices typically found in solar cell absorbers ($n{\sim}3-4$), the probability of avoiding total internal reflection is given by $1/2n^2$, i.e. less than 5%. After each re-absorption, there is still the possibility of Auger or Shockley-Read-Hall recombination bringing an end to the existence of the photon. Even if a lucky photon manages to escape the semiconductor, it still has to contend with the danger of being parasitically absorbed by one of the intervening layers. Thus, every photon generated by radiative recombination has to meet one of three fates: escape into the external world, re-absorption by the semiconductor, or parasitic absorption. Since these are independent events, the probabilities must sum to 1. If we assign probabilities p_e, p_r and p_a to these respectively, we can arrive at an expression for the EQE_{EL} in terms of the internal quantum efficiency (IQE_{EL})[5]:

$$EQE_{EL} = \frac{p_e IQE_{EL}}{1 - p_r IQE_{EL}} \qquad 3.27$$

Here, IQE_{EL} is the probability that an absorbed photon will undergo radiative recombination, and is given by the ratio of the radiative and the total recombination rate in the absorber:

$$IQE_{EL} = \frac{k_2 np}{k_2 np + R_{SRH}} \qquad 3.28$$

Where k_2 is bimolecular recombination rate constant, R_{SRH} is the Shockley-Read-Hall rate constant, and n, p are the free electron and hole densities

respectively. It may be noted from the quoted expression for EQE_{EL}, that for 100% external luminescence, two criteria need to be satisfied:

1. $IQE_{EL} = 1$, which means that the internal luminescence quantum efficiency has to be 100%, i.e. no non-radiative recombination

2. $p_e + p_r = 1$, which implies $p_a = 0$ ($p_e + p_r + p_a = 1$). This means that should be no parasitic absorbance in the system.

In particular, it can be noted that the EQE_{EL} falls rapidly with even very small changes in IQE_{EL}[5]. As a result, high luminescence efficiencies are remarkably difficult to achieve, and demand stringent control over both the optics and the electronics of the cell.

3.3 Optical Modelling: Transfer Matrix Method

Optical modelling has proven to be an indispensable tool for the design and optimisation of photovoltaic cells. Optical modelling refers to the development of models that can predict the optical response— mainly reflection, transmission and absorption— of the solar cell structures under consideration. Such modelling helps design structures to maximise photon absorption in the active layer(s) and minimise it in layers with parasitic absorption. This is especially important for indirect semiconductors like silicon, where the absorption co-efficient is very low near the band edge. Current matching considerations make such modelling also

extremely important for multijunction cell development, as has been explained in the previous chapter.

The choice of optical model depends on the dimensions and optical properties of the layers, the properties of the light source, and the available computational power. If the dimensions of the optical structure are much larger than the wavelength of light (like the pyramids on black silicon), geometrical optics is applicable. When the system contains structures comparable to the wavelength of light, solving Maxwell's equations from first-principles ("rigorous models") is a possible approach. There are several numerical methods available: finite difference time-domain, finite element method, finite integration technique etc. However, these methods are computationally expensive, since they perform a very dense discretization (at the sub-wavelength length scale) of the problem.

The situation in thin-film PV is much simplified due to the planarity of the layers. In this case, a 1D model based on classical wave optics is sufficient for an accurate prediction of the optical response. This is usually implemented by solving the Fresnel equations in a formalism that uses matrices and, hence, is called the Transfer Matrix Method (TMM). TMM is extensively used in this thesis, and a concise explanation of the calculations is presented below, following the approach of Steven J. Byrnes[32].

Consider a stack made up of a series of smooth planar layers, such as a perovskite solar cell. We define the direction normal to be the plane to be $\hat{\boldsymbol{z}}$**.** The

plane is encompassed by $\hat{\boldsymbol{x}}$ and $\hat{\boldsymbol{y}}$**.** We assume that the wave-vector is in the x-z plane, forming an angle θ with the normal. In this case, the incident wave-vector $\boldsymbol{k}$ is given by:

$$\boldsymbol{k} = \frac{2\pi\tilde{n}}{\lambda}(\hat{\boldsymbol{z}}\cos\theta + \hat{\boldsymbol{x}}\sin\theta) \tag{3.29}$$

Here, $\tilde{n}$ is the complex refractive index, and λ is the wavelength in vacuum. We can represent the electric field at any point as a sum of forward-propagating and backwards-propagating waves:

$$\boldsymbol{E}(\boldsymbol{r}) = \boldsymbol{E}_{\boldsymbol{f}}^{\boldsymbol{0}} e^{i\boldsymbol{k}_f\cdot\boldsymbol{r}} + \boldsymbol{E}_{\boldsymbol{b}}^{\boldsymbol{0}} e^{i\boldsymbol{k}_b\cdot\boldsymbol{r}} \tag{3.30}$$

At interfaces, waves are reflected and transmitted according to the Fresnel equations. The reflection co-efficient r is the ratio of the reflected amplitude to the incident amplitude. The transmission co-efficient t is the ratio of the transmitted amplitude to the incident amplitude. The co-efficient are different for s and p polarised light. If a wave meets the interface between medium 1 (of refractive index $\tilde{n}_1$) and medium 2 (of refractive index $\tilde{n}_2$), and the incident angle is θ_i and the transmitted angle is θ_t, the Fresnel co-efficients are given by:

$$r_s = \frac{\tilde{n}_1\cos\theta_i - \tilde{n}_2\cos\theta_t}{\tilde{n}_1\cos\theta_i + \tilde{n}_2\cos\theta_t} \tag{3.31}$$

$$r_p = \frac{\tilde{n}_2\cos\theta_i - \tilde{n}_1\cos\theta_t}{\tilde{n}_2\cos\theta_i + \tilde{n}_1\cos\theta_t} \tag{3.32}$$

$$t_s = \frac{2\tilde{n}_1\cos\theta_t}{\tilde{n}_1\cos\theta_i + \tilde{n}_2\cos\theta_t} \tag{3.33}$$

$$t_p = \frac{2\tilde{n}_1\cos\theta_t}{\tilde{n}_1\cos\theta_i + \tilde{n}_2\cos\theta_t} \tag{3.34}$$

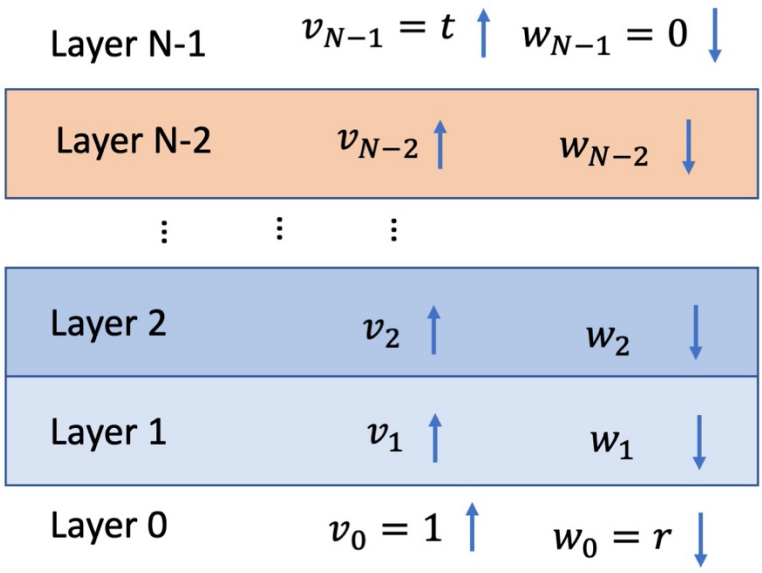

Figure 3.2 | Sample stack with N layers depicting the forward and backward moving waves considered in the transfer matrix formalism.

Consider that the optical stack has N materials numbered $0,1,\ldots N-1$, where the first and the last are semi-infinite. Light starts off with amplitude 1 in layer 0, and heads towards layer 1. Let v_n be the amplitude of the forward moving wave in the nth material. Let w_n be the amplitude of the backwards moving wave in the nth material. By this definition, $v_0 = 1$, $w_0 = r$, $v_{N-1} = t$, and $w_{N-1} = 0$. Now by superposition, we get:

$$v_{n+1} = \left(v_n e^{i\delta_n}\right) t_{n,n+1} + w_{n+1} r_{n+1,n} \qquad 3.35$$

$$w_n e^{-i\delta_n} = w_{n+1} t_{n+1,n} + \left(v_n e^{i\delta_n}\right) r_{n,n+1} \qquad 3.36$$

Where $r_{n,m}$ and $t_{n,m}$ are the Fresnel co-efficients for a wave heading from layer n to layer m. The Fresnel equations obey the follow identities: $r_{n,m} = -r_{m,n}$ and

$t_{n,m}t_{m,n} - r_{n,m}r_{m,n} = 1$. This allows us to write the superposition equations in terms of matrices:

$$\begin{pmatrix} v_n \\ w_m \end{pmatrix} = M_n \begin{pmatrix} v_{n+1} \\ w_{m+1} \end{pmatrix} \quad 3.37$$

Where,

$$M_n = \begin{pmatrix} e^{-i\delta_n} & 0 \\ 0 & e^{i\delta_n} \end{pmatrix} \begin{pmatrix} 1 & r_{n,n+1} \\ r_{n,n+1} & 1 \end{pmatrix} \left(\frac{1}{t_{n,n+1}}\right) \quad 3.38$$

By successive multiplication of these matrices, a relationship between $w_0 = r$ and $v_{N-1} = t$ can be derived:

$$\begin{pmatrix} v_0 \\ w_0 \end{pmatrix} = \begin{pmatrix} 1 \\ r \end{pmatrix} = \widehat{M} \begin{pmatrix} v_{N-1} \\ w_{n-1} \end{pmatrix} = \widehat{M} \begin{pmatrix} t \\ 0 \end{pmatrix} \quad 3.39$$

Here $\widehat{M}$ is given by:

$$\widehat{M} = \frac{1}{t_{0,1}} \begin{pmatrix} 1 & r_{0,1} \\ r_{0,1} & 1 \end{pmatrix} M_1 M_2 \cdots M_{N-2} \quad 3.40$$

So, r and t for any multi-layer thin film can now be calculated as $t = 1/\widehat{M}_{00}$ and r $= \widehat{M}_{10}/\widehat{M}_{00}$. This is sufficient to calculate the transmitted and reflected electric fields. For evaluating power flows, we need to evaluate the Poynting vector $\boldsymbol{S} = \boldsymbol{E} \times \boldsymbol{H}$**.** Hence, we evaluate the Poynting vector as a fraction of the incoming power. For s-polarisation, we obtain:

$$\boldsymbol{S} \cdot \hat{\boldsymbol{z}} = \frac{Re\left[\tilde{n}\, cos\, \theta\, (E_f^* + E_b^*)(E_f - E_b)\right]}{Re[\tilde{n}_0\, cos\, \theta_0]} \quad 3.41$$

The expression for p-polarisation is analogous. To evaluate the reflectance R and transmittance T, the values of E_f and E_b need to be plugged in. They can be calculated using the previously described matrix approach. To evaluate T, we plug

in $E_f = t$, $E_b = 0$. To find R, we plug in $E_f = 1$, $E_b = r$. The absorption A in a layer can calculated as the difference between $\boldsymbol{S} \cdot \hat{\boldsymbol{z}}$ at the start and end of a layer. Thus, TMM allows us to calculate the reflection, transmission, and layer absorptions of a multi-layer thin-film stack. For incoherent layers, a generalised TMM has been developed by Centurioni[33], which the interested reader is referred to for a fuller explanation.

3.4 References

(1) Markvart, T. Thermodynamics of Losses in Photovoltaic Conversion. *Appl. Phys. Lett.* **2007**, *91* (6), 7–9. https://doi.org/10.1063/1.2766857.

(2) Markvart, T. From Steam Engine to Solar Cells: Can Thermodynamics Guide the Development of Future Generations of Photovoltaics? *Wiley Interdiscip. Rev. Energy Environ.* **2016**, *5* (5), 543–569. https://doi.org/10.1002/wene.204.

(3) Markvart, T.; Bauer, G. H. What Is the Useful Energy of a Photon? *Appl. Phys. Lett.* **2012**, *101* (19), 2012–2015. https://doi.org/10.1063/1.4766177.

(4) Rau, U.; Paetzold, U. W.; Kirchartz, T. Thermodynamics of Light Management in Photovoltaic Devices. *Phys. Rev. B - Condens. Matter Mater. Phys.* **2014**, *90* (3), 1–16. https://doi.org/10.1103/PhysRevB.90.035211.

(5) Kirchartz, T.; Staub, F.; Rau, U. Impact of Photon Recycling on the Open-Circuit Voltage of Metal Halide Perovskite Solar Cells. *ACS Energy Lett.* **2016**, *1* (4), 731–739. https://doi.org/10.1021/acsenergylett.6b00223.

(6) Kirchartz, T. Photon Management in Perovskite Solar Cells. *J. Phys. Chem. Lett.* **2019**, 5892–5896. https://doi.org/10.1021/acs.jpclett.9b02053.

(7) Kirchartz, T.; Rau, U. What Makes a Good Solar Cell? *Adv. Energy Mater.* **2018**, *1703385*, 1703385. https://doi.org/10.1002/aenm.201703385.

(8) Kirchartz, T.; Staub, F.; Rau, U. Impact of Photon Recycling on the Open-Circuit Voltage of Metal Halide Perovskite Solar Cells. *ACS Energy Lett.* **2016**. https://doi.org/10.1021/acsenergylett.6b00223.

(9) Guillemoles, J. F.; Kirchartz, T.; Cahen, D.; Rau, U. Guide for the Perplexed to the Shockley–Queisser Model for Solar Cells. *Nature Photonics*. 2019, pp 501–505. https://doi.org/10.1038/s41566-019-0479-2.

(10) Kirchartz, T.; Rau, U. Detailed Balance and Reciprocity in Solar Cells. *Phys. Status Solidi Appl. Mater. Sci.* **2008**, *205* (12), 2737–2751. https://doi.org/10.1002/pssa.200880458.

(11) Rau, U.; Blank, B.; Müller, T. C. M.; Kirchartz, T. Efficiency Potential of Photovoltaic Materials and Devices Unveiled by Detailed-Balance Analysis. *Phys. Rev. Appl.* **2017**, *7* (4), 1–9. https://doi.org/10.1103/PhysRevApplied.7.044016.

(12) Rau, U. Reciprocity Relation between Photovoltaic Quantum Efficiency and Electroluminescent Emission of Solar Cells. *Phys. Rev. B - Condens. Matter Mater. Phys.* **2007**, *76* (8), 1–8. https://doi.org/10.1103/PhysRevB.76.085303.

(13) Blank, B.; Kirchartz, T.; Lany, S.; Rau, U. Selection Metric for Photovoltaic

Materials Screening Based on Detailed Balance Analysis. **2017**, *068701* (2012), 1–31. https://doi.org/10.1103/PhysRevApplied.8.024032.

(14) Abou-Ras, D.; Kirchartz, T.; Rau, U. *Advanced Characterization Techniques for Thin Film Solar Cells*; 2011. https://doi.org/10.1002/9783527636280.

(15) Würfel, P. Thermodynamic Limitations to Solar Energy Conversion. *Phys. E Low-Dimensional Syst. Nanostructures* **2002**, *14* (1–2), 18–26. https://doi.org/10.1016/S1386-9477(02)00355-7.

(16) Green, M. A. Accuracy of Analytical Expressions for Solar Cell Fill Factors. *Sol. Cells* **1982**, *7* (3), 337–340. https://doi.org/10.1016/0379-6787(82)90057-6.

(17) Green, M. A. General Temperature Dependence of Solar Cell Performance and Implications for Device Modelling. *Prog. Photovoltaics Res. Appl.* **2003**, *11* (5), 333–340. https://doi.org/10.1002/pip.496.

(18) Green, M. A. Self-Consistent Optical Parameters of Intrinsic Silicon at 300 K Including Temperature Coefficients. *Sol. Energy Mater. Sol. Cells* **2008**, *92* (11), 1305–1310. https://doi.org/10.1016/j.solmat.2008.06.009.

(19) Green, M. a. Solar Cells: Operating Principle. 1982, p 2.

(20) Green, M. A. Third Generation Photovoltaics : Advanced Solar Energy Conversion. Springer-Verlag Berlin Heidelberg: Berlin, Heidelberg 2006.

(21) Green, M. A. Accurate Expression for Solar Cell Fill Factors Including Series and Shunt Resistance. *Applait Phys. Lett.* **2016**, *108*, 081111-1–5. https://doi.org/10.1063/1.4942660.

(22) Green, M. A. Limits on the Open-Circuit Voltage and Efficiency. *IEEE Trans. Electron Devices* **1984**, *ED-31* (5), 671–678.

(23) Green, M. A. Radiative Efficiency of State-of-the-Art Photovoltaic Cells. *Prog. Photovoltaics Res. Appl.* **2012**, *20* (4), 472–476. https://doi.org/10.1002/pip.1147.

(24) National Renewable Energy Laboratory. Reference Air Mass 1.5 Spectra Reference Air Mass 1.5 Spectra%0A (accessed Sep 21, 2020).

(25) Shockley, W.; Queisser, H. J. Detailed Balance Limit of Efficiency of P-n Junction Solar Cells. *J. Appl. Phys.* **1961**, *32* (3), 510–519. https://doi.org/10.1063/1.1736034.

(26) Würfel, P.; Finkbeiner, S.; Daub, E. Generalized Planck's Radiation Law for Luminescence via Indirect Transitions. *Appl. Phys. A Mater. Sci. Process.* **1995**, *60* (1), 67–70. https://doi.org/10.1007/BF01577615.

(27) Wurfel, P. The Chemical Potential of Radiation. *J. Phys. C Solid State Phys.* **1982**, *15* (18), 3967–3985. https://doi.org/10.1088/0022-3719/15/18/012.

(28) Landsberg, P. T.; Tonge, G. Thermodynamic Energy Conversion Efficiencies. *J. Appl. Phys.* **1980**, *51* (7), R1–R20. https://doi.org/10.1063/1.328187.

(29) Hirst, L. C.; Ekins-Daukes, N. J. Fundamental Losses in Solar Cells. *Prog. Photovoltaics Res. Appl.* **2011**, *19* (3), 286–293. https://doi.org/10.1002/pip.1024.

(30) Nayak, P. K.; Mahesh, S.; Snaith, H. J.; Cahen, D. Photovoltaic Solar Cell

Technologies: Analysing the State of the Art. *Nat. Rev. Mater.* **2019**, *4* (4), 269–285. https://doi.org/10.1038/s41578-019-0097-0.

(31) optics.org. Alta sets flexible solar record with 29.1% GaAs cell https://optics.org/news/9/12/19 (accessed Sep 29, 2020).

(32) Byrnes, S. J. Multilayer Optical Calculations. **2016**.

(33) Centurioni, E. Generalized Matrix Method for Calculation of Internal Light Energy Flux in Mixed Coherent and Incoherent Multilayers. *Appl. Opt.* **2005**, *44* (35), 7532. https://doi.org/10.1364/AO.44.007532.

(34) Landsberg P. T. and Badescu V. Carnot factor in solar cell efficiencies. *J. Phys. D: Appl. Phys.* **33** 3004 (2000)

(35) Markvart T. The thermodynamics of optical etendue. *J. Opt. A: Pure Appl. Opt.* **10** 015008 (2007)

(36) Kirchartz T. *et al.* Reciprocity Between Electroluminescence and Quantum Efficiency Used for the Characterisation of Silicon Solar Cells. *Prog. Photovolt: Res. Appl.* 2009 **17:**394-402 (2009)

(37) Tvingstedt K. *et al*. Radiative efficiency of lead iodide based perovskite solar cells. *Scientific Reports* **4** 6071(2014)

4

Methods

4.1 Overview

All the techniques used in this thesis— both experimental and modelling— are briefly detailed here to aid readers who may wish to reproduce the results. These details are all collected here, despite the consequent loss of context, to enable the main chapters to focus on the results and their interpretation. Some of these measurements have been performed in collaboration with others. Such contributors have been credited at appropriate locations in chapters where their contributions appear.

4.2 Mixed Halide Perovskite Solar Cell Fabrication

4.2.1 $FA_{0.83}Cs_{0.17}Pb(I_xBr_{1-x})_3$ based Solar Cell Fabrication

All powders were used as purchased without further purification and weighed in a nitrogen filled glovebox. To form the perovskite precursor, lead iodide (PbI_2, 99.99 %, Alfa-Aesar), lead bromide ($PbBr_2$, >98 %, Alfa-Aesar), cesium iodide (CsI,

99.99%, Alfa-Aesar), and formamidinium iodide (FAI, GreatCell Solar) were weighed stoichiometrically to the target perovskite composition (e.g. $FA_{0.83}Cs_{0.17}Pb(I_{0.6}Br_{0.4})_3$). To form the precursor solution, a 4:1 volume ratio of anhydrous N,N-dimethylformamide (DMF, Sigma Aldrich)) and anhydrous dimethyl sulfoxide (DMSO, (Sigma Aldrich) was added to achieve a concentration of 1.4 M.

Poly(4-butylphenyl-diphenyl-amine) (polyTPD, 1-Material) was used as hole transporting material (HTM). Poly-TPD was dissolved in toluene at a concentration of 1 mg/mL and was doped with 20 wt% 2,3,5,6-Tetrafluoro-7,7,8,8-tetracyanoquinodimethane (F4-TCNQ, Lumtec). [6,6]-phenyl-C_{61}-butyric acid methyl ester ($PC_{61}BM$, >99.5%, Solenne BV) was used as the electron transporting material (ETM). PCBM was dissolved in a volume ratio of 3:1 chlorobenzene : 1,2-dichlorobenzene and used at a concentration of 20 mg/mL. Bathocuproine (BCP, 98 %, Alfa-Aesar) was implemented as a hole blocking layer (HBL) at concentration of 0.5 mg/mL in isopropanol (IPA).

The p-i-n device architecture employed for the FACs cells was FTO/polyTPD/perovskite/PCBM/BCP/Ag. Fluorine-doped tin oxide (FTO, Pilkington TEC 7, 7 Ω/sq. sheet resistivity) was used as the transparent electrode. Zinc powder and 2 M HCl were used to etch the FTO to the desired electrode pattern. The substrates were then cleaned by sonication in deionised (DI) water with 1 vol% Decon90 cleaning detergent, before being rinsed with DI water, acetone and IPA

sequentially. The substrates were then dried with a nitrogen gun followed by an UV-Ozone treatment for 15 minutes, prior to use.

Immediately after the substrate preparation was complete, the HTM was deposited in ambient air. 70 µL of the doped polyTPD solution was dispensed onto a substrate spinning at 2000 rpm for 20 seconds, and then annealed at 130 °C for 10 minutes. Then the perovskite layer was deposited in a nitrogen filled glovebox. 170 µL of the perovskite precursor solution was dispensed onto a substrate spinning at 1000 rpm. After 5 seconds, the substrate was accelerated to 5000 rpm over the course of 5 s and remained at this speed for 30 s. 5 s before the end of this process, 350 µL of anisole was applied to the spinning substrate as an anti-solvent quench. The films were then annealed at 100 °C for 45 minutes.

The ETM and HBL were both deposited in a nitrogen filled glovebox. 40 µL of the PCBM solution was dynamically spun onto the perovskite layer at 2000 rpm for 20 s, then heated at 100 °C for 3 mins to remove any remaining solvent. BCP was applied on the PCBM layer by depositing 100 µL onto a substrate spinning at 5000 rpm for 30 s before being heated to 100 °C for one minute to remove any remaining solvent.

Devices were completed by thermally evaporating silver electrodes (100 nm) through shadow masks (active area defined as 0.0919 cm^2) under high vacuum (~10^{-6} mbar) using a Nano36, Kurt J. Lesker thermal evaporator.

4.2.2 Preparation of $FA_{0.83}MA_{0.17}Pb(I_{0.4}Br_{0.6})_3$ based Solar Cells

The structure of the cell was: FTO/SnO_2/Perovskite/Spiro-OMeTAD/Au. The SnO_2 and Spiro-OMeTAD layers were deposited as described in Petrus M.L et al[1]. FAI (Dyesol), MABr (Dyesol), PbI_2 (TCL Chemicals) and $PbBr_2$ (Alfa Aesar) were weighed to exact stoichiometry in a glovebox and dissolved in 4:1 DMF:DMSO (Sigma Aldrich), such that the overall concentration was 0.5 M. The solution was stirred at 85°C for 5 hours in nitrogen. All solution processing and annealing was done in a nitrogen filled glovebox. The perovskite was spun in on top of the SnO_2 at 1000 rpm for 10 s, followed by 6000 rpm for 35 s. The film was quenched with 150 uL of Anisol, 40 s into the spin. The film was annealed at 100°C for 1 hour in the glovebox. 2 nm of Cr, followed by 100 nm of Au was evaporated on top of the HTL using a Nano36, Kurt.K.Lesker thermal evaporator held under high vacuum (~10^{-6} mbar). The device active area was 0.0919cm^2.

4.3 $Cs_2AgBiBr_6$ based Thin-Films and Solar Cells

4.3.1 $Cs_2AgBiBr_6$ Thin Film Fabrication

The double-perovskite thin films studied in this work were all prepared through sequential vapour deposition. AgBr (99% Fluka), $BiBr_3$ (≥98% Sigma Aldrich) and CsBr (99.9% Sigma Aldrich) were placed in separate crucibles and

sequentially thermally evaporated onto the substrates in a vacuum-sealed chamber. Our optimized procedure evaporated 90 nm of AgBr, 120 nm of $BiBr_3$ and 150 nm of CsBr to obtain 300 nm of $Cs_2AgBiBr_6$. This basic stack was repeated sequentially to achieve the desired total film thickness. To achieve thicknesses that are not multiples of 300 nm (like the 750 nm reported), fractions of the previously mentioned thicknesses were deposited, while keeping the ratios the same (1:1.3:1.6 AgBr:$BiBr_3$:CsBr). After the deposition of the desired thickness, we annealed the samples on a hotplate at 250 ºC for 30 minutes in air. The post-deposition annealing temperature and time were optimized to obtain the best solar cell PCE.

4.3.2 $Cs_2AgBiBr_6$ based solar cell fabrication.

FTO or ITO coated glass (7 Ω/sq. sheet resistivity) was cleaned by sequential sonication in soap, water, acetone, and isopropanol. After being dried with a N_2 gun, the substrates were further cleaned by O_2 plasma for 10 minutes. Titanium isopropoxide (140 µl in 1 ml of EtOH) was added to 1 ml of acidic EtOH (10 µl of HCl 2M in 1 ml EtOH) and deposited on the FTO substrates by spin-coating at 2000 rpm for 45 sec with 2000 rpm/sec acceleration. Following this, the films were annealed at 150°C for 15 min and 500°C for 30 min. SnO_2 layers were prepared by spin-coating at 3000 rpm (200 rpm/sec) for 30 sec of a solution of $SnCl_4 \cdot 5H_2O$ in isopropanol (17.5 mg/ml) on top of the FTO or ITO coated glasses. The so-

prepared films were annealed at 100°C for 10 min followed by an annealing at 180°C for 30 min. The SnO_2 and TiO_2 films were placed in the vacuum chamber, and the $Cs_2AgBiBr_6$ film was deposited as previously presented. The hole transport material (Spiro-OMeTAD, Lumtec) was dissolved in chlorobenzene (85 mg/ml) and doped with 20 µl of LiTFSI (500 mg/ml in BuOH) and 30 µl of tert-butylpyridine. The solution was then deposited on the active layer by spincoating in air at 2000 rpm (2000 rpm/sec) for 45 sec. The devices were then left overnight in a desiccator, and then completed by the evaporation of 100 nm silver contacts. Semi-transparent devices were fabricated by substituting the silver by 20 nm of gold and using a 435 nm thick double-perovskite absorber.

4.4 Solar Cell Characterisation

For measuring the performance of the fabricated solar cells, simulated AM1.5 sunlight was generated with a class AAB ABET solar simulator. An NREL-calibrated KG5 filtered silicon reference cell was used to calibrate it for 100 mW/cm^2 equivalent irradiance. The mismatch factor was calculated to consistently be less than 1.05 between 300-900 nm, which is the usual operating range of the perovskite cells presented here. A Keithley 2400 sourcemeter was used to record the current-voltage curves. During measurement, a metal aperture (0.0929 cm^2) was used to define the active area.

4.5 Fourier Transform Photocurrent Spectroscopy

Fourier-transform photocurrent spectroscopy was used to measure the photovoltaic external quantum efficiency (EQE_{PV}) of solar cells using a Bruker Vertex 80 Fourier-transform infrared spectrometer. A Newport Orial Sol3A solar simulator was used to provide a simulated AM1.5G illumination spectrum. The cells were illuminated with this light source to induce halide segregation but measurements were performed with an optical filter to enable enhanced dynamic range in the sub-bandgap region. The current signal from the solar cell was converted to a voltage using a Stanford Research SR570 current preamplifier and fed into an analog-to-digital converter for measurement. The absolute values of EQE_{PV} were calculated based on the ratio of the current from the cell to that of the current from a calibrated Si reference solar cell (Newport) of known EQE_{PV}

4.6 UV-Vis Transmission and Reflection

The transmittance and reflectance were measured with a Perkin Elmer Lambda 1050, equipped with a 100mm integrated sphere. For reflectance measurements, calibration was performed using a diffuse reflecting $BaSO_4$ reference.

4.7 Photoluminescence Quantum Efficiency

For the measurement of the photoluminescence quantum efficiency (PLQE), a CNI Low Noise Violet Blue 405 nm 200 mW laser is used with an integrating sphere and an Ocean Optics Maya2000 Pro spectrometer. A calibration halogen lamp from OceanOptics is used to calibrate the system, including the sphere, fiber and spectrometer. The PLQE is calculated according to the method developed by De Mello et al[11].

4.8 X-Ray Diffraction

Powder XRD patterns were recorded on a Panalytical X'pert powder diffractometer (equipped with Cu Kα1 anode X-ray source, and radiation; λ = 1.5405 Å). The samples, consisting of a $Cs_2AgBiBr_6$ thin film on a quartz substrate, were rotated during data collection, which was done at room temperature and normal indoor lighting conditions

4.9 Ellipsometry

Optical constants were measured using a Woollam RC2 spectroscopic ellipsometer. The ellipsometer was calibrated with a reference silicon wafer with ~20 nm SiO_2 on top. Ellipsometric data (amplitude ratio and phase shift) was

acquired at three different angles: 55°, 65°, 75° from 210-1690 nm. The software CompleteEASE was used to model the data to obtain the Kramers-Kronig consistent complex refractive index.

4.10 Photothermal Deflection Spectroscopy

Photothermal deflection spectroscopy is a surface-sensitive absorption measurement technique capable of measuring absorbance several orders of magnitude weaker than possible with conventional UV-Vis spectroscopy. The sample is immersed in an inert liquid FC-72 Fluorinert® (3M Company), which exhibits a large change in refractive index per unit change in temperature. For the measurements, a monochromatic pump light is shined on the sample, where non-radiative recombination of excited carriers causes sample heating. This causes a thermal gradient near the sample surface, causing a change in the refractive index of the liquid. A fixed wavelength CW laser probe beam is passed through this refractive index gradient, causing a reflection proportional to the light absorbed at that wavelength. This is detected by a photo-diode and lock-in amplifier combination. A monochromator is used to scan through different wavelengths to obtain the complete absorption spectra.

4.11 Surface Photovoltage Spectroscopy

The surface photovoltage measurements were performed using a KP020 Single-Point Kelvin Probe from KPTechnology. The measurements were performed in the ambient.

4.12 Optical-Pump Terahertz Probe Spectroscopy

An amplified laser system (Spectra Physics, MaiTai – Ascend – Spitfire), with a 5 kHz repetition rate, centre wavelength of 800 nm and pulse duration of 35 fs was used to generate THz radiation via the inverse-spin Hall effect from a spintronic emitter, as described in Buizza L.R. et al[2]. The THz probe was focused onto the sample and detected via free-space electro-optical sampling in a ZnTe(110) crystal of thickness 200 μm. A 400 nm pump pulse was generated using a Beta Barium Borate (BBO) crystal. Transient decays were measured by recording the change in peak THz amplitude transmitted as a function of pump-probe delay time. Measurements were carried out under vacuum (< 10-2 mbar).

OPTP is a standard non-contact characterization technique that provides information about local charge-carrier mobility at THz frequencies. Thin-film samples were excited at 400 nm with an amplified laser with low repetition rate illuminating from the perovskite side of the films. We measured the change in

terahertz transmission ($\Delta T/T$) over time. At low fluences (< 50 $\mu J cm^{-2}$) there is a linear relationship between the charge-carrier mobility μ and the change in photoconductivity of the sample ΔS:

$$\mu = \frac{\Delta S \, A_{eff}}{Ne}. \qquad 4.1$$

The change in photoconductivity can in turn be related to the fractional change in terahertz transmission using a standard formula for thin-film samples:

$$\Delta S = -\epsilon_0 c(n_A + n_B)\left(\frac{\Delta T(t=0)}{T}\right) \qquad 4.2$$

We can also calculate the number of photoexcited charge carriers using:

$$N = \phi \frac{E\,\lambda}{h\,c}\left(1 - R_{pump}(\lambda)\right)\left(1 - T_{pump}(\lambda)\right) \qquad 4.3$$

We can combine equations 4.1, 4.2 and 4.3, to calculate the effective charge-carrier mobility as:

$$\mu = -\epsilon_0 c(n_A + n_B)\frac{A_{eff} hc}{Ee\lambda\left(1 - R_{pump}(\lambda)\right)\left(1 - T_{pump}(\lambda)\right)}\left(\frac{\Delta T(t=0)}{T}\right) \qquad 4.4$$

4.13 Modelling Halide Segregation

4.13.1 Optical Modelling

The optical modelling was done using a modified version of the implementation of the generalised transfer matrix method developed by E. Centurioni[3]. All calculations were done in Python using the libraries NumPy and SciPy. The model takes the wavelength dependant complex refractive index, the

layer thicknesses and the incident angle (normal incidence in our case) as input. It calculates the absorptance of each layer, and the transmittance and the reflectance of the stack. To model the EQE_{PV} of the halide-segregated perovskite cell, we used a hypothetical stack: FTO (200nm)/SnO_2 (10nm)/Perovskite (400nm)/Spiro-OMeTAD (200nm)/Ag (100nm). We assume 100% collection efficiency and thus take the EQE_{PV} to be the same as the absorptance of the perovskite. This assumption does not dictate our results, since V_{OC} is only weakly dependant on the current. The complex refractive index of the perovskite was got via the effective medium approximation, as described in the next subsection. For FTO[4], SnO_2,[5] Spiro-OMeTAD[6] and Ag[7], values reported in the literature were used.

4.13.2 Effective Medium Approximation

The approach of Hoerantner et al. in shifting the optical constants of $MAPbI_3$[8] was followed to simulate the optical constants of the iodide-bromide mixed halide perovskites. An 18mV Urbach tail was also appended till 0.5 eV. Since the trend in V_{OC} is our main focus and the V_{OC} is determined largely by the absorption tail, this approach is sufficient for the purpose. To model the expected loss from a two-phase segregation, the complex refractive index of the halide-segregated film was modelled as a Bruggeman effective medium of the two phases. Since the amount of minority phase is small, the Bruggeman effective refractive index turns out to be very close to a linear combination of the two refractive indices.

4.13.3 Electronic Modelling

The open-circuit voltage was calculated using the equation:

$$V_{oc} = \frac{kT}{q} ln\left(\frac{J_{sc}}{J_0}\right) \quad 4.5$$

J_{sc} is the overlap integral of the solar AM1.5 spectrum with the EQE_{PV} of the cell. Similarly, J_0 is calculated as the overlap integral of the Blackbody spectrum at 300K with the EQE_{PV} of the cell:

$$J_{sc} = q \int_0^{\infty} EQE_{PV}(\lambda) \cdot \phi_{AM1.5}(\lambda) \cdot d\lambda \quad 4.6$$

$$J_0 = \frac{J_{0,rad}}{EQE_{EL}} = \frac{q}{EQE_{EL}} \int_0^{\infty} \phi_{BB}(\lambda) \cdot EQE_{PV}(\lambda) \cdot d\lambda \quad (3)$$

Here, the EQE_{EL} is the electroluminescence quantum efficiency. These equations have been derived in chapter 3.

4.13.4 Modelling the Effect of varying EQE_{EL}

To investigate the effect of different EQE_{EL} of the majority and minority phases, we sum dark current contributions from the minority and majority phases. The dark current contribution from the majority phase is calculated by integrating over the unsegregated device EQE_{PV} (Equation 4.7). The dark current contribution from the minority phase, is calculated by integrating over the segregated EQE_{PV}, after subtracting the unsegregated EQE_{PV} (Equation 4.8). For

simplicity, the broadening in the majority phase is considered to be part of the minority phase.

$$\boldsymbol{J_{00,maj}} = \frac{q}{EQE_{EL,maj}} \int_0^\infty \phi_{BB}(\lambda) \cdot EQE_{PV,unseg}(\lambda) \cdot d\lambda \qquad 4.7$$

$$\boldsymbol{J_{00,min}} = \frac{q}{EQE_{EL,min}} \int_0^\infty \phi_{BB}(\lambda) \cdot (EQE_{PV,seg}(\lambda) - EQE_{PV,unseg}(\lambda)) \cdot d\lambda \qquad 4.8$$

4.13.5 Calculation of Distribution of Bandgaps

We model the perovskite as being made of two components:

1. A majority phase: A phase mixture comprising of exponentially distributed bandgaps.
2. A minority phase: phase pure, i.e. a Dirac-delta bandgap distribution.

The optical constants of the perovskite are modelled through a linear effective medium approximation. The optical constants of perovskites of different bandgaps are approximated by linearly shifting the absorption edge and then performing a Kramers-Kronig transform to obtain the refractive index in the same fashion as Hoerantner et al[9]. Work by McMeekin et al. demonstrates that the bandgaps of mixed-halide perovskites do shift linearly in this way[10].

$$\widetilde{n_{EMA,maJ}} = \int \tilde{n}(E) \cdot f(E) \cdot dE$$

Here $f(E) \cdot dE$ is the molar fraction of the film with bandgap at E. We have verified that, in this case, the linear approximation nearly coincides with the more

specialised Bruggeman effective medium approximation. In our case, the distribution $f(E)$ is taken to be exponential:

$$f(E) = \begin{cases} \alpha e^{\alpha(E-E_g)}, & E < E_g \\ 0, & E > E_g \end{cases}$$

As we have already mentioned, the minority phase is modelled as a pure phase.

The segregated film refractive index is calculated using Bruggeman EMA, assuming fractions x and $1 - x$ for the two phases respectively:

$$n_{EMA} = EMA(n_{EMA,maj}, n_{min})$$

The effective refractive index is used to optically model the absorptance of the perovskite layer, which is used to fit the measured EQE_{PV} of the segregated perovskite, by varying the parameters x and α.

4.14 Estimating Diffusion Length from EQE

The optical response of the stack was modelled using the generalized transfer matrix method[3]. All calculations were performed in Python using the NumPy and SciPy libraries. Transfer matrix calculations take the complex refractive index spectrum and thickness for each layer as input. The stack used was Glass/ITO (200 nm)/SnO_2 (20 nm)/$Cs_2AgBiBr_6$ (435 nm)/Spiro-OMeTAD (200 nm)/ Au (20 nm). The calculation provides us with the intensity of light at any cross-section of the stack, which can be used to calculate the generation within any desired volume of the

solar cell. We assume that with diffusion length of $d_{e(h)}$, all electrons (holes) generated within a distance $d_{e(h)}$ of the electron (hole) transporting layer are collected. The cell current is determined by the smaller of the electron and hole currents. The stack used was Au (20 nm)/Spiro-OMeTAD (200 nm)/ $Cs_2AgBiBr_6$ (435 nm)/SnO2 (20 nm)/ITO (200 nm)/Glass. The transfer matrix method was used to calculate, for each wavelength, the fraction of photons absorbed within a distance $d_{e(h)}$ from the electron (hole) transporting layer. We make the assumption that there is no current loss at the interfaces. Then, the smaller of the two calculated photon fractions is, by definition, the external quantum efficiency of the cell at each wavelength. We then obtained the best fit for the measured EQE by varying d_e and d_h using the Newton-Raphson method implemented in the library Scipy.

4.15 References

(1) Petrus, M. L.; Schutt, K.; Sirtl, M. T.; Hutter, E. M.; Closs, A. C.; Ball, J. M.; Bijleveld, J. C.; Petrozza, A.; Bein, T.; Dingemans, T. J.; Savenije, T. J.; Snaith, H.; Docampo, P. New Generation Hole Transporting Materials for Perovskite Solar Cells: Amide-Based Small-Molecules with Nonconjugated Backbones. *Adv. Energy Mater.* **2018**, *8* (32), 1801605. https://doi.org/10.1002/aenm.201801605.

(2) Buizza, L. R. V.; Crothers, T. W.; Wang, Z.; Patel, J. B.; Milot, R. L.; Snaith, H. J.; Johnston, M. B.; Herz, L. M. Charge-Carrier Dynamics, Mobilities, and

Diffusion Lengths of 2D–3D Hybrid Butylammonium–Cesium–Formamidinium Lead Halide Perovskites. *Adv. Funct. Mater.* **2019**, *29* (35), 1902656. https://doi.org/10.1002/adfm.201902656.

(3) Centurioni, E. Generalized Matrix Method for Calculation of Internal Light Energy Flux in Mixed Coherent and Incoherent Multilayers. *Appl. Opt.* **2005**, *44* (35), 7532. https://doi.org/10.1364/AO.44.007532.

(4) Ball, J. M.; Stranks, S. D.; Hörantner, M. T.; Hüttner, S.; Zhang, W.; Crossland, E. J. W.; Ramirez, I.; Riede, M.; Johnston, M. B.; Friend, R. H.; Snaith, H. J. Optical Properties and Limiting Photocurrent of Thin-Film Perovskite Solar Cells. *Energy Environ. Sci.* **2015**, *8* (2), 602–609. https://doi.org/10.1039/C4EE03224A.

(5) Çetinörgü, E.; Gümüs, C.; Goldsmith, S.; Mansur, F. Optical and Structural Characteristics of Tin Oxide Thin Films Deposited by Filtered Vacuum Arc and Spray Pyrolysis. *Phys. Status Solidi Appl. Mater. Sci.* **2007**, *204* (10), 3278–3285. https://doi.org/10.1002/pssa.200723081.

(6) Filipič, M.; Löper, P.; Niesen, B.; De Wolf, S.; Krč, J.; Ballif, C.; Topič, M.; Wolf, S. De; Krč, J.; Ballif, C.; Topič, M. CH_3NH_3PbI_3 Perovskite / Silicon Tandem Solar Cells: Characterization Based Optical Simulations. *Opt. Express* **2015**, *23* (7), A263. https://doi.org/10.1364/OE.23.00A263.

(7) Johnson, P. B.; Christy, R. W. Optical Constants of the Noble Metals. *Phys. Rev. B* **1972**, *6* (12), 4370–4379. https://doi.org/10.1103/PhysRevB.6.4370.

(8) Löper, P.; Stuckelberger, M.; Niesen, B.; Werner, J.; Filipič, M.; Moon, S.-J.; Yum, J.-H.; Topič, M.; De Wolf, S.; Ballif, C. Complex Refractive Index Spectra of $CH_3NH_3PbI_3$ Perovskite Thin Films Determined by Spectroscopic Ellipsometry and Spectrophotometry. *J. Phys. Chem. Lett.* **2015**, *6* (1), 66–71. https://doi.org/10.1021/jz502471h.

(9) Hörantner, M. T.; Leijtens, T.; Ziffer, M. E.; Eperon, G. E.; Christoforo, M. G.; McGehee, M. D.; Snaith, H. J. The Potential of Multijunction Perovskite Solar Cells. *ACS Energy Lett.* **2017**, *2* (10), 2506–2513. https://doi.org/10.1021/acsenergylett.7b00647.

(10) McMeekin, D. P.; Sadoughi, G.; Rehman, W.; Eperon, G. E.; Saliba, M.; Horantner, M. T.; Haghighirad, A.; Sakai, N.; Korte, L.; Rech, B.; Johnston, M. B.; Herz, L. M.; Snaith, H. J. A Mixed-Cation Lead Halide Perovskite Absorber for Tandem Solar Cells. *Science (80-.).* **2016**, *351* (6269), 151–155. https://doi.org/10.1126/science.aad5845.

(11) de Mello *et al.* An improved experimental determination of external photoluminescence quantum efficiency. *Adv. Mater.* **9:** 230-232 (1997)

5

Origin of Voltage Loss in Wide Bandgap Mixed Halide Perovskite Solar Cells

The results presented in this chapter have been published in the article:

Mahesh, S.; Ball, J. M.; Oliver, R. D. J.; McMeekin, D. P.; Nayak, P. K.; Johnston, M. B.; Snaith, H. J. **Revealing the Origin of Voltage Loss in Mixed-Halide Perovskite Solar Cells**. *Energy Environ. Sci.* **2020**, *13* (1), 258–267. https://doi.org/10.1039/C9EE02162K.

5.1 Overview

The tunable bandgap of metal-halide perovskites has opened up the possibility of tandem solar cells with over 30% efficiency. Iodide–bromide (I–Br) mixed-halide perovskites are crucial to achieve the optimum bandgap for such tandems. However, when the Br content is increased to widen the bandgap, cells fail to deliver the expected increase in open-circuit voltage (V_{OC}). This loss in V_{OC} has been attributed to photo-induced halide segregation. Here, we

combine Fourier transform photocurrent spectroscopy (FTPS) with detailed balance calculations to quantify the voltage loss resulting from halide segregation, thus providing a means to quantify the impact of the low bandgap iodide-rich phases on performance. Our results indicate that, contrary to popular belief, halide segregation is not the dominant V_{OC} loss mechanism in Br-rich wide bandgap cells. Rather, the loss is dominated by the relatively low initial radiative efficiency of the cells, which arises from both imperfections within the absorber layer, and at the perovskite/charge extraction layer heterojunctions. We thus identify that focussing on maximising the initial radiative efficiency of the mixed-halide films and devices is more important than attempting to suppress halide segregation. Our results suggest that a V_{OC} of up to 1.33 V is within reach for a 1.77 eV bandgap perovskite, even if halide segregation cannot be suppressed.

5.2 Introduction

Perovskites are particularly attractive materials for making multi-junction solar cells because their bandgap can be tuned across the visible spectrum simply by ionic substitution and mixing over a wide stoichiometric range. For ABX_3 perovskites, with the selection of A = Cs, methylammonium (MA^+) or formamidinium (FA^+), B = Sn^{2+} or Pb^{2+}, and X = I^-, Br^- or Cl^-, the bandgap can be tuned from ~1.24eV to 3.5eV[1]. Mixed-halide I-Br perovskites, $APb(I_xBr_{1-x})_3$, have bandgaps between 1.48-2.35eV, making them ideal for tandem and triple junction

applications. However, the same ion-interchangeability that facilitates such convenient bandgap tuning also gives rise to a host of problems due to ionic diffusion. Notably, under illumination, "halide segregation" occurs in $APb(I_xBr_{1-x})_3$ films, leading to the formation of iodide-rich phases which have lower bandgaps than the surrounding unsegregated material[2]. This was first observed through photoluminescence (PL) spectra in mixed-halide films, where a lower energy emission was correlated with the formation of iodide-rich domains. Much work has since followed up on this phenomenon in an attempt to understand the mechanism[3–8]. Notably, some studies have shown that enhanced crystallinity in the perovskite film can lead to reduced severity of the halide segregation[9–11].

The most efficient single junction perovskite solar cells reported to-date have bandgaps which range from 1.53 to 1.62 eV, and are generally composed of iodide-rich mixed-cation lead mixed-halide perovskites. These cells only have a loss in V_{OC} of ~ 60 mV from the theoretical limit[12] (herein, we will refer to these "benchmark" perovskite cells as the ~1.6eV gap cells). In contrast, the best mixed-halide devices with a high bromide content of 40% and above, show many hundreds of mV of loss in V_{OC} from the theoretical limit. The open-circuit voltage (V_{OC}) has been observed to "plateau" at about 1.2 V, (or even decrease) with the addition of Br to the $APb(I_{1-x}Br_x)_3$ perovskite, once the bromide content exceeds around 20%[13]. The prevailing notion in the scientific community is that the emergence of the low energy PL peak in mixed-halide perovskite films

corresponds to a limitation upon the open-circuit voltage; the open-circuit voltage will be “pinned” by the low bandgap iodide-rich impurity phases. However, intuition aside, there is yet no quantitative analysis of how halide segregation influences open-circuit voltage. Notably, the wide bandgap cell contributes the majority of the power output of a tandem cell. Thus, both scientifically and commercially, it is important to able to quantify the loss occurring due to halide-segregation.

The plethora of parameters that halide segregation depends on greatly confounds efforts to understand and suppress it. Even studies that have succeeded in suppressing the PL shift show significant V_{OC} loss from the theoretical limit, when benchmarked against ~1.6eV cells[14]. Photoluminescence has generally been the tool of choice to probe halide segregation. While photoluminescence can detect the presence of low-bandgap phases, it is an insensitive measure of their size and composition. Some have used X-ray diffraction, but this is not quantitatively reliable due to its strong sensitivity to texture[5]. Methods that can quantitatively characterize the segregated phase(s) and associated performance losses are highly desirable. In addition, the scientific community lacks a way of quantifying the variation in open-circuit voltage expected as a function of degree of halide segregation, and other fundamental properties such as radiative efficiency.

This study uses Fourier-Transform Photocurrent Spectroscopy (FTPS) to reveal the evolution of iodide-rich impurity phase absorption in mixed-halide perovskite solar cell undergoing phase segregation under a simulated AM1.5G illumination. Reports so far have treated halide segregation as a simple two-phase phenomenon. This study finds that, contrary to popular belief, a distribution of minority phases is formed. Further, there is also significant bandgap broadening in the "majority" phase. The measured FTPS spectra are coupled with detailed balance calculations[15] to estimate the voltage penalty from the evolution of the sub bandgap absorption tail. This enables the voltage penalty from halide-segregation to be isolated, ignoring losses from other mechanisms. The study also finds that the broadening of the majority phase absorption edge, which is distinct from the minority phase, should have a significant impact upon the V_{OC}. Following the same approach, a thermodynamic model is presented, by which V_{OC} losses for various bandgaps and severities of segregation can be estimated. By comparing the time evolution of the calculated halide segregation induced V_{OC} loss with the measured time evolution of the open-circuit voltage of the cell, the study concludes that the open-circuit voltage losses in bromide-rich high-bandgap cells are not dominated by halide segregation. Large trap densities, which mediate non-radiative Shockley-Read-Hall (SRH) recombination, are the dominant loss channel, and are already present before halide segregation commences. Therefore, significant improvements in V_{OC} are within reach by improving

absorber radiative efficiency and quality of the perovskite-charge transport layer heterojunctions, even if halide segregation remains unsuppressed.

5.3 What determines the V_{OC} of a PV cell?

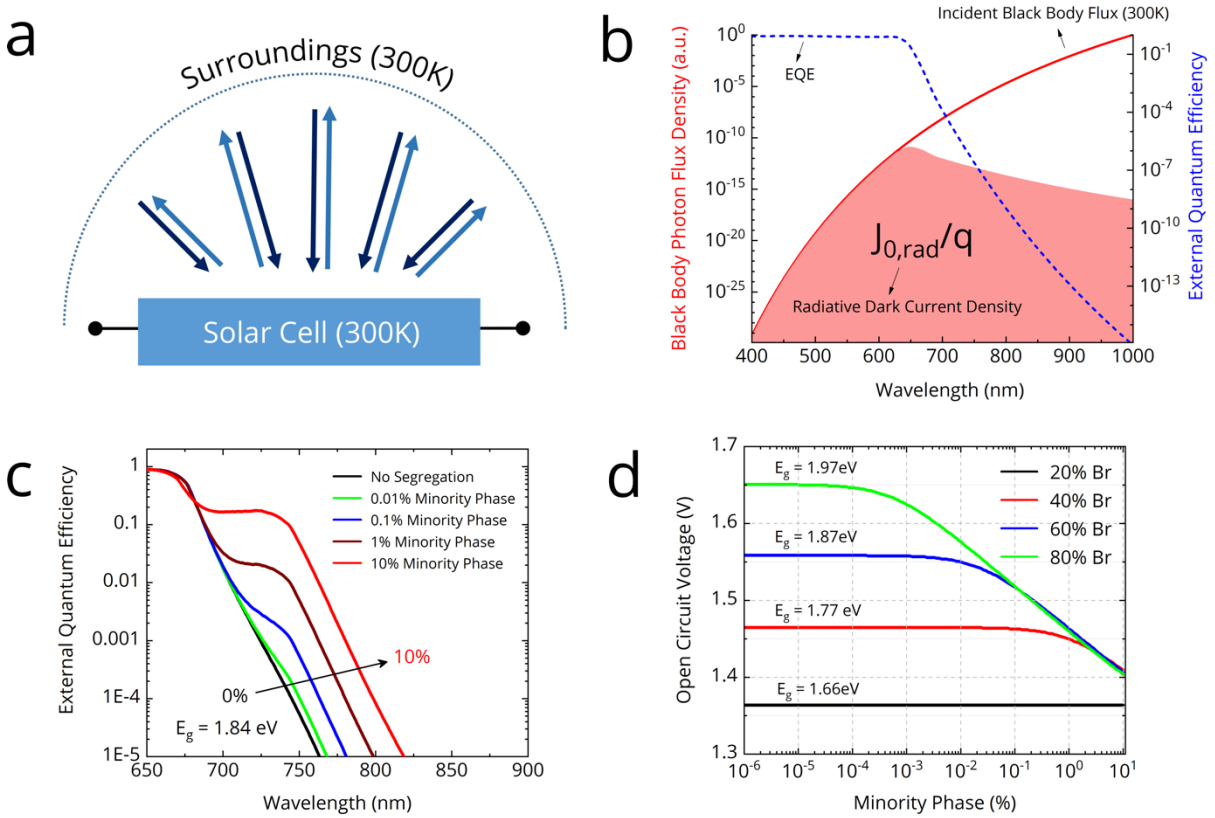

Figure 5.1 | (**a**) Principle of Detailed Balance: In equilibrium, the black-body photon flux emitted and absorbed by the solar cell are equal. (**b**) The dark current J_0 is determined by the overlap integral of the blackbody flux and the EQE_{PV}. **(c)** Modelled EQE_{PV} for a halide segregating 1.84eV gap perovskite. The "bump" in the tail is due to absorption by the minority phase (80:20 I:Br) **(d)** Radiative limit V_{OC} as a function of the volume percentage of the minority phase (80:20 I:Br). Calculations performed by Suhas Mahesh.

We begin by summarizing the factors that influence the open-circuit voltage of a solar cell and illustrate how we would expect the open-circuit voltage to evolve with the emergence of lower bandgap impurity phases. The mentioned equations

have already been derived in the chapter *Thermodynamics and Optical Modelling*. We briefly review the ideas again to establish context. The open-circuit voltage of an ideal solar cell is expressed by the well-known relation[16]:

$$V_{oc} = \frac{k_B T}{q} \ln\left(\frac{J_{sc}}{J_0}\right) \quad 5.1$$

Here, J_{sc} is the short circuit current density and J_0 is the dark recombination current density, also called as the dark current or reverse saturation current density. The calculation of J_{sc} via an overlap integral between the photovoltaic external quantum efficiency EQE_{PV} and the solar photon flux $\phi_{AM1.5}$ is well known:

$$J_{sc} = q \int_0^\infty EQE_{PV}(\lambda) \cdot \phi_{AM1.5}(\lambda) \cdot d\lambda \quad 5.2$$

The photovoltaic external quantum efficiency EQE_{PV} is defined as the fraction of photons incident on the solar cell that produce electric current. However, the calculation of the recombination current density $J_0$is not often discussed, despite being theoretically well established. Experimentally, the dark recombination current density J_0 is the current that can be extracted from a solar cell in the dark by applying a large reverse bias. This current arises from thermally excited charges, i.e. charges excited by the ambient black-body radiation being absorbed by the cell (Fig. 5.1a). This is the reason for J_0 being strongly dependent on junction temperature ($\propto T^3 e^{\frac{qE_g}{kT}}$)[17].

In a real cell which includes non-radiative recombination, the recombination current J_0 is the sum of the radiative and the non-radiative recombination currents. The radiative recombination current can be calculated by using the

principle of detailed balance: in equilibrium, the absorbed photon current must equal the emitted photon current. Thus, we can calculate the radiative recombination current through the overlap integral between the blackbody flux and the EQE_{PV} of the photoactive material. Thus, $J_{0,rad}$, which is equal to the emitted photon current can be written as:

$$J_{0,rad} = q \int_0^\infty \phi_{BB}(\lambda) \cdot EQE_{PV}(\lambda) \cdot d\lambda \qquad 5.3$$

However, in a real cell, only a fraction of the recombination is radiative. The non-radiative recombination current is accounted for using the external electroluminescence quantum efficiency (EQE_{EL}), which is defined as the ratio of the radiative recombination current to the total recombination current (Equation 5.4). By definition, EQE_{EL} is always positive and less than unity.

$$EQE_{EL} = \frac{J_{0,rad}}{J_0} = \frac{J_{0,rad}}{J_{0,rad} + J_{0,non-rad}} \qquad 5.4$$

U. Rau has rigorously established the relation between the open-circuit voltage and EQE_{EL}[18]. Thus, by definition, the total recombination current density J_0 can be calculated by including the external electroluminescence quantum efficiency EQE_{EL} as a scaling factor[15]:

$$J_0 = \frac{J_{0,rad}}{EQE_{EL}} = \frac{q}{EQE_{EL}} \int_0^\infty \phi_{BB}(\lambda) \cdot EQE_{PV}(\lambda) \cdot d\lambda \qquad 5.5$$

Thus, J_0 can be calculated for a cell if EQE_{PV}, EQE_{EL} and the junction temperature are known. The relation between V_{OC} and EQE_{EL} can also be written as:

$$V_{oc} = V_{oc,rad} + \left(\frac{k_B T}{q}\right) \cdot ln(EQE_{EL}) \quad 5.6$$

Here, $V_{OC,rad}$ is the V_{OC} calculated in the radiative limit. It is worth noting that because the black-body photon flux increases exponentially towards lower energies, tail state absorption makes the largest contribution to J_0. In fact, the magnitude of J_0 is almost exclusively dictated by the position of the absorption tail. Thus, even small increases in tail-state absorption can increase J_0 by orders of magnitude, lowering V_{OC} (cf. equation 5.1). These tail states could even be so small as to be virtually invisible to conventional UV-Vis absorption spectroscopy or EQE_{PV} measurements. Consequently, their impact on J_{sc} would be negligible. However, their impact on the V_{OC} would be significant. This fact is central to the understanding of how the presence of low-bandgap phases affects V_{OC}.

The presence of a low-bandgap minority phase in the perovskite film can be expected to show up as a "bump" in the sub-bandgap absorptance. The magnitude of the absorption feature would be determined by the fraction of the film converted to the minority phase. As we have explained above, even a small below bandgap absorption feature would be sufficient to increase J_0 significantly. If the feature is sufficiently large, J_0 (and hence V_{OC}) would be completely determined by the minority phase, independent of the bandgap of the majority phase. This is the thermodynamic reasoning behind the assumption that voltage "pinning" will occur in cells exhibiting halide segregation. We used a generalized transfer matrix[19] based optical model and detailed balance calculations to model

the impact of halide segregation on V_{OC} in the radiative limit. The model serves to reveal the susceptibility of different compositions to V_{OC} losses upon halide segregation. We fixed the minority phase bandgap at 1.66 eV, consistent with reports of minority phase composition being 20:80 Br:I, regardless of majority phase bandgap[20]. We modelled the complex refractive index of the perovskite as a Bruggeman effective medium[21] of the minority and majority phases. We then used the generalized transfer matrix method to calculate the cell EQE_{PV} in an ITO/SnO_2/perovskite/spiro-OMeTAD/gold stack. Our modelled EQE_{PV} curves show a "bump" in the sub-gap absorption whose magnitude increases with fraction of minority phase (Fig. 5.1c). We then employed detailed balance calculations to estimate the V_{OC} in the radiative limit as a function of percentage of minority phase in the film (Fig. 5.1d).

Our model reveals that V_{OC} drops off logarithmically once the minority phase fraction exceeds a threshold. This threshold is smaller for larger bromide concentrations. For instance, an 80:20 Br:I film with 0.01% minority phase, incurs a voltage penalty of 76mV. However, a 40:60 Br:I film will shows almost no V_{OC} loss at the same minority phase percentage. At higher minority phase concentrations (>1%), the V_{OC} is similar ("pinned") for all majority phase compositions, but notably still around 70 mV larger than the V_{OC} generated from a 100% minority phase composition cell.

5.4 Photo-induced sub-bandgap states

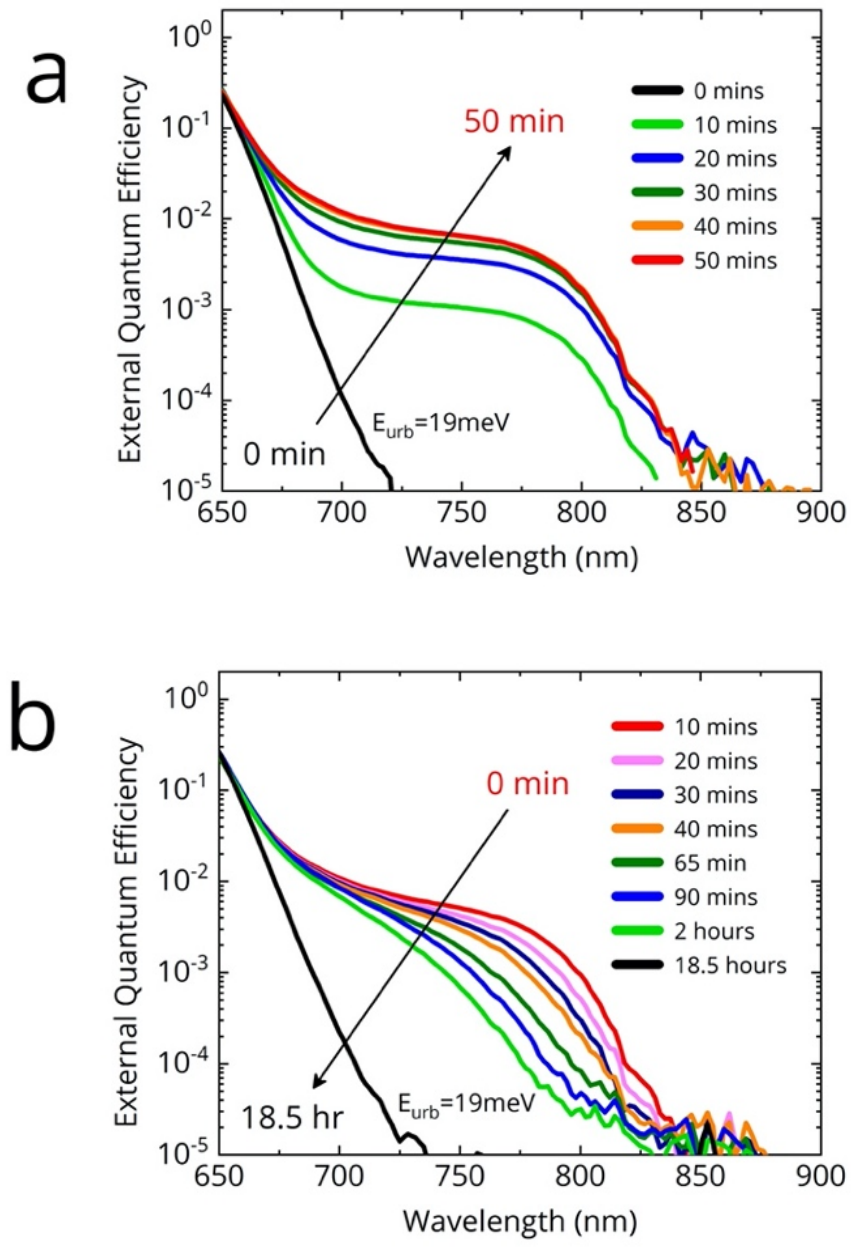

Figure 5.2 | Photovoltaic External Quantum Efficiency (EQE_{PV}) of a $FA_{0.83}MA_{0.17}Pb(I_{0.4}Br_{0.6})_3$ cell measured with Fourier Transform Photocurrent Spectroscopy (FTPS). **(a)** Time evolution of EQE_{PV} under simulated AM1.5 illumination. **(b)** Time evolution of EQE_{PV} upon being kept in the dark. Cells fabricated by Robert J. Oliver, David McMeekin and Suhas Mahesh. Measurements performed by James Ball and Suhas Mahesh.

We used Fourier Transform Photocurrent Spectroscopy (FTPS) to study the effect of simulated sunlight on the external quantum efficiency of an $FA_{0.83}MA_{0.17}Pb(I_{0.4}Br_{0.6})_3$ solar cell deposited via the anti-solvent quenching method. In figure 5.2a we show the time-evolution of the External Quantum Efficiency (EQE_{PV}) spectrum of an $FA_{0.83}MA_{0.17}Pb(I_{0.4}Br_{0.6})_3$ device under simulated AM1.5 illumination. We use simulated AM1.5 illumination as phase segregation has been shown to be sensitive to illumination spectrum and intensity[3]. We held the cells at open-circuit at all times. After 10 minutes of light soaking, we observe a new shoulder at ~780 nm (1.59 eV) in the sub-bandgap region of the EQE_{PV} spectrum, consistent with the photo-induced formation of iodide-rich impurity phases. We observe this feature to grow, and eventually saturate at about 1% quantum efficiency after 40 minutes. At saturation, the absorption edge of the feature is approximately 800 nm (1.55 eV), as determined from the EQE_{PV} inflection point. We identify this feature as absorption from the iodide-rich regions formed upon illumination (we note that the A site composition is FA-rich, and hence lower bandgap than $MAPbX_3$ perovskites[22]). We shall henceforth refer to the iodide-rich regions as the *minority phase*, and the phase in which the minority phase is embedded as the *majority phase*. The appearance of the minority phase causes virtually no change in the bandgap of the majority phase, and is hence virtually invisible to conventional UV-Vis absorption spectroscopy. Consequently, the photo-induced carrier generation rate in the cell is unaffected. Upon being

kept in dark, we observe the feature to relax back towards the original starting point, albeit much more slowly over more than 18 hours (Fig. 5.2b). Incidentally, upon halide “de-segregation”, the minority phase appears to progressively become less rich in iodide. This is in contrast to segregation, where the heavily iodide-rich phase rapidly forms first. We interpret this to imply that halide segregation proceeds by first nucleating the lowest-bandgap phase, followed by the growth of this phase. In contrast, during desegregation, the iodide-rich phase absorption gradually blue shifts, while also reducing in intensity. This suggests that the mechanism of desegregation is likely to be entropic mixing, which causes the minority phase to be slowly enriched with bromide, consistent with disappearance of the most iodide-rich phases first.

5.5 Bandgap Distribution in a Segregated Absorber

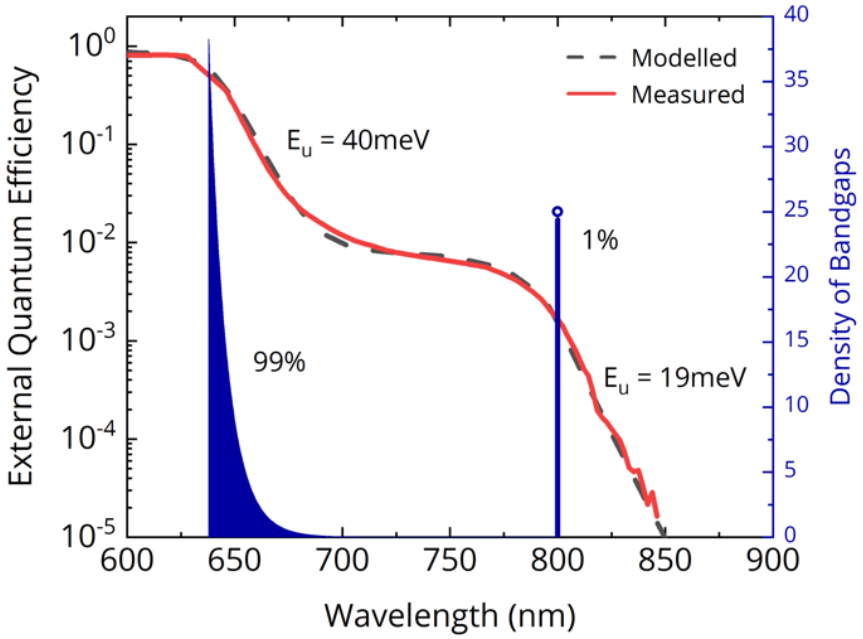

Figure 5.3 | (**a**) Modelled halide segregated EQE_{PV} (dotted green) and the distribution of bandgaps in perovskite (blue) at saturated halide segregation. Calculations performed by Suhas Mahesh.

Studies so far treat halide segregation as a simple two phase phenomenon[3,20,23,24]. A minority phase of a single composition (often 20:80 Br:I) is assumed to have formed, which is the source of the low-energy photoluminescence peak. In practice, such a clear-cut phase separation is unlikely. A continuum in iodide concentration, or at least multiple phases are more probable. Our FTPS measurements (Fig. 5.3) confirm this hypothesis. The absorption edge of the pristine cell has an Urbach energy of 19 meV. As the film segregates, we estimate the Urbach energy of the majority phase to increase,

reaching 40 meV after 50 minutes of light soaking. This points to considerable compositional inhomogeneity in the majority phase due to segregation. Serious V_{OC} losses are expected when the Urbach energy exceeds $k_B T$[25]. This loss mechanism in halide segregated films has hitherto escaped attention. However, the most significant losses do arise from the iodide-rich minority phase. The appearance of a nearly flat shoulder between 725-800 nm indicates that the minority phase is comprised of material with a narrow bandgap range centered on 1.55 eV. The Urbach energy of the tail is 19 meV—similar to that of the unsegregated film, but notably slightly larger than the ~15 meV expected for $FA_{0.83}MA_{0.17}PbI_3$.

We model the halide segregated EQE_{PV} (Fig. 5.2a; red curve at 50mins) using the generalized transfer matrix method[26] and effective medium approximation, and use it to extract the distribution of bandgaps in the material. We find that the majority phase exhibits an exponential distribution of bandgaps, decaying from a peak at 640 nm. The minority phase has a single bandgap at 800 nm. Through our model, we estimate that the minority phase occupies about 1 % by volume of the film (assuming the optical density scales with thickness). This is in agreement with previous estimation at 1% by Hoke et al.[20] The extent of segregation can also be roughly estimated from the EQE_{PV}, by observing the magnitude of the minority phase absorption, which is also 1%. This follows from Lambert's law, since EQE_{PV} scales linearly with absorptance at low-absorptance (<<1).

5.6 V_{OC} Penalty from Halide Segregation

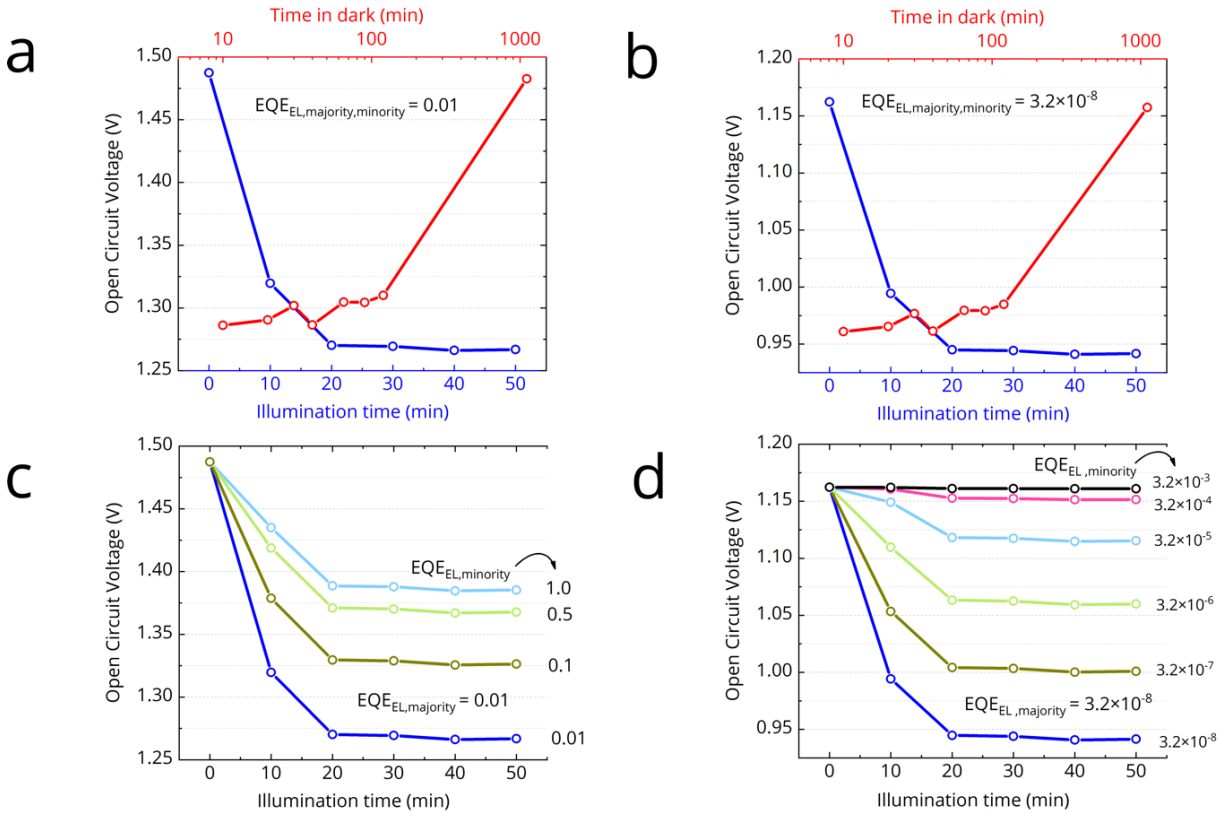

Figure 5.4 | Time evolution of V_{OC} calculated via detailed balance using the FTPS data measured on $FA_{0.83}MA_{0.17}Pb(I_{0.4}Br_{0.6})_3$ based cells. We show the effect of varying the EQE_{EL} of the two phases. **(a)** Time evolution of V_{OC}, assuming EQE_{EL} = 0.01 for both the majority and minority phases. This would be the voltage of a wide bandgap cell if it were electronically as good as the best 1.6 eV cells. **(b)** Time evolution of V_{OC}, assuming a realistic EQE_{EL} = $3.2{\cdot}10^{-8}$ for both the majority and minority phases. **(c)** Time evolution of V_{OC} for a range of minority phase EQE_{EL}, fixing majority phase EQE_{EL} = 0.01. **(d)** Time evolution of V_{OC} for a range of minority phase EQE_{EL}, fixing majority phase EQE_{EL} = $3.2{\cdot}10^{-8}$. Calculations performed by Suhas Mahesh.

The severity of halide-segregation in a solar cell is best characterized by the accompanying V_{OC} loss. Here, we perform detailed balance calculations on the presented FTPS data to determine the expected loss in V_{OC} arising from halide-segregation. This calculated loss can be used as a measure of the severity of halide-segregation in a cell. We perform the previously described detailed balance

calculations (Equations 5.1,5.2,5.5) on the measured time dependent EQE_{PV} spectra (Fig. 5.2a, 5.2b) to get the expected time dependence of the open-circuit voltage (Fig. 5.4). In the first instance, we assume that both the majority and minority phase have the same time-invariant radiative efficiency, EQE_{EL} (expressed as a fraction of unity, where EQE_{EL} = 1 is 100%). The magnitude of the voltage loss arising from halide segregation is not dependent on the choice of EQE_{EL}, as long it does not vary with time. So its precise value is not relevant. Later, we also discuss the case of the two phases having different EQE_{EL}.

The best perovskite cells (with a bandgap of ~1.6eV) today typically have an EQE_{EL} ~ 0.01[27]. We set EQE_{EL} = 0.01 for both the minority and majority phases and calculate the time evolution of V_{OC} (Fig. 5.4b). We calculate V_{OC} = 1.49 eV from the pristine cell. As segregation proceeds in time, we calculate that the V_{OC} should drop very rapidly in the beginning, losing 170 mV in 10 minutes, despite sub-bandgap EQE_{PV} being just ~0.1%. After 20 minutes, we estimate the V_{OC} to have dropped by 220 mV and hit 1.27 V. After 20 minutes, we determine that the V_{OC} is stable at 1.27 V, despite an increasing sub-bandgap absorption. Thus, we estimate that the total V_{OC} loss at saturated segregation to be 220 mV. This loss is independent of the EQE_{EL} chosen, provided it does not change during time under illumination. Setting $EQE_{EL} = 3.2 \cdot 10^{-8}$ predicts a more realistic V_{OC} = 1.16 V from pristine cell (Equation 5.5). The calculated V_{OC} loss due to segregation, however, remains the same at 220 mV (Fig. 5.4b).

5.7 Impact of enhanced EQE_{EL} of minority phase

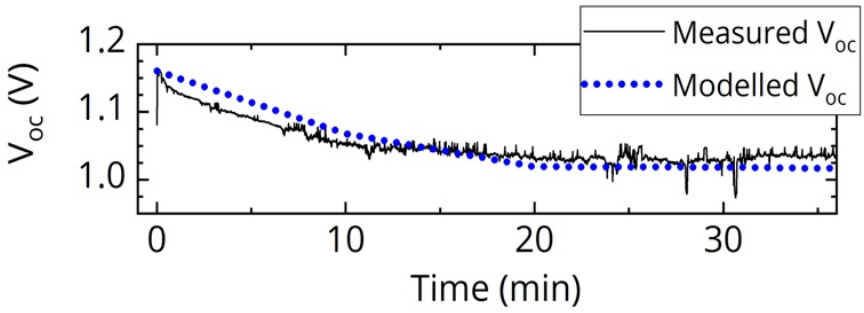

Figure 5.5 | Measured time evolution of the V_{OC} of a halide segregating cell (black). The modelled V_{OC} (dotted blue) allows us to extract $EQE_{EL,majority} = 3.2 \cdot 10^{-8}$ and $EQE_{EL,minority} = 6.2 \cdot 10^{-7}$. Calculations and measurements performed by Suhas Mahesh.

Since the carrier diffusion length in these materials is relatively long, the charge carriers will explore a large volume of film under open-circuit conditions, when they are not being extracted. Therefore, they are likely to find the low bandgap minority phase regions, and will become localized within these regions due to energetic confinement. In a real cell, the minority phase occupies a small fraction of the total film volume. Since the emission from a halide-segregated film is predominantly via this lower energy phase, we know that there is a predominant accumulation of charge carriers in this region. This accumulation of carriers within the low bandgap regions of mixed phase perovskites, is often referred to as charge-funneling[28]. The average carrier concentration within the minority phases, will therefore be much higher than in the majority phase regions (or non-segregated film). For a 1% segregated film, this may therefore result in a

100 fold increase in charge-carrier density within the low bandgap phase (in comparison to the charge density in the unsegregated majority phase). This increased charge density will promote radiative recombination, due to bimolecular radiative recombination competing more strongly with monomolecular non-radiative recombination. Trap filling from the local increase in carrier density will also serve to increase the radiative efficiency[29]. This therefore suggests that we would expect an increased EQE_{EL} from the minority phase. We note that a narrower bandgap 3D minority phase inclusion in a wider bandgap 2D majority phase matrix, is the strategy adopted for the best perovskite light emitting diodes[28]. In our case here, the increase in radiative efficiency of the iodide-rich minority phase, would cause the drop in V_{OC} to be less dramatic. Thus we expect that the 220 mV loss we estimate from the EQE_{PV} measurements, is an upper-bound for the V_{OC} loss. We also calculate the V_{OC} (Fig. 5.4c) by varying the EQE_{EL} of the minority phase, while keeping the majority phase EQE_{EL} fixed at 0.01. We find that every ten-fold increase in the radiative efficiency of the minority phase, the V_{OC} loss due to halide segregation reduces by ~ 55meV.

If we set the majority phase EQE_{EL} at a realistic $3.2 \cdot 10^{-8}$, we can vary minority phase EQE_{EL} by many more orders of magnitude (Fig. 5.4d). When we choose the radiative recombination of the minority phase to be 100,000 times higher than the majority phase, then we estimate no V_{OC} loss following halide segregation. In this case, the recombination rate in the absorber would be controlled by fast non-

radiative recombination in the majority phase, and the formation of a low-bandgap phase would only cause a negligible increase in the net recombination rate.

In order to understand the impact of the enhanced EQE_{EL} that we just described, we measure the time evolution of the open-circuit voltage of a pristine $FA_{0.83}MA_{0.17}Pb(I_{0.4}Br_{0.6})_3$ cell (bandgap 1.94eV) under simulated AM1.5 conditions (Fig. 5.5). We observe the voltage to drop quickly initially and then stabilize with a V_{OC} loss of around 120mV after 20 minutes. This is consistent with the behavior predicted by our EQE_{PV} measurements (Fig. 5.4). We model the curve using the approach previously presented (Fig. 5.5), and vary the EQE_{EL} of the majority and minority phase until we achieve a similar trend. We find consistency if we set the EQE_{EL} of the majority phase to $3.2 \cdot 10^{-8}$, and the EQE_{EL} of the minority phase to $6.2 \cdot 10^{-7}$. This suggests a 19-fold enhanced EQE_{EL} in the minority phase, as compared to the majority phase, which seems to be perfectly reasonable.

5.8 Halide Segregation in FACs perovskite cells

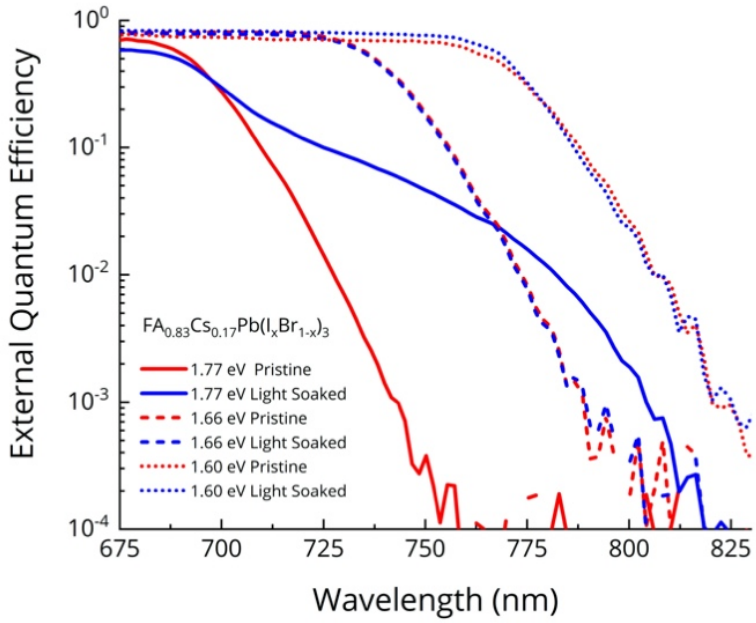

Figure 5.6 | Photovoltaic External Quantum Efficiencies (EQE_{PV}) of $FA_{0.83}Cs_{0.17}Pb(I_xBr_{1-x})_3$ based p-i-n solar cells measured before and after light soaking for 2 hours under 0.2 suns illumination. Measurements performed by Suhas Mahesh and James Ball.

In order to quantify the V_{OC} penalty from halide segregation, in the preceding sections we presented studies on a perovskite composition (FAMA based) and bandgap (1.94 eV) that rapidly underwent halide segregation, in order to exemplify our theoretical assessment. However, in order to exemplify more state-of-the-art wide bandgap compositions, we now present results for the $FA_{0.83}Cs_{0.17}Pb(I_xBr_{1-x})_3$ family. We fabricated $FA_{0.83}Cs_{0.17}Pb(I_xBr_{1-x})_3$ based p-i-n devices of three different bandgaps: 1.77 eV (40% Br, suitable for perovskite-perovskite tandems[30]), 1.66 eV (23% Br, ideal for perovskite-silicon tandems[30]),

and 1.60 eV (10% Br, best bandgap for single-junction performance in our lab). We light soaked the devices for two hours under 1 sun simulated AM1.5 illumination, till the absorption tail was seen to evolve no more, and show the measured FTPS-EQE_{PV} spectra for the pristine and light-soaked devices in figure 6.

The 1.66 eV and 1.60 eV absorbers show negligible changes in the absorption tail, indicating that the low bandgap phase segregated fraction is less than our resolution limit of 10^{-4}. As our modelling (Fig. 5.1d) has indicated, this will be accompanied by negligible V_{OC} loss. Furthermore, the Urbach energy, which is a measure of electronic disorder, is just 15 meV before and after segregation, suggesting that no segregation has occurred. The 1.77 eV bandgap absorber (40% Br), on the other hand, undergoes halide-segregation, evolving a sub bandgap absorption feature. The formed absorption shoulder is also quite broad, suggesting that there is no single prominent composition, but only a mixture of phases. A detailed balance calculation on the EQE_{PV} of this 1.77eV cell, presented in Fig. 5.6, reveals a 97 mV V_{OC} penalty due to halide-segregation, assuming no change in the radiative efficiency EQE_{EL} during segregation. As we have already explained, we expect that the actual V_{OC} loss will be less than 97 mV, owing to increased radiative efficiency of the iodide-rich phase. Indeed, the V_{OC} measurement done simultaneously with the FTPS-EQE_{PV} reveals that the loss is only 75 mV, since the V_{OC} drops from 1.105 V to 1.030 V.

5.9 The key factor limiting the V_{OC} of wide band gap mixed-halide perovskite cells

In the preceding sections, we combined sensitive EQE_{PV} measurements with detailed balance calculations to quantify the V_{OC} penalty due to halide segregation in FAMA and FACs based mixed-halide perovskite cells. In this section, we quantitatively compare the segregation-loss to the non-radiative V_{OC} loss.

In our FAMA based 1.94eV bandgap cell, we calculated the expected V_{OC} to be 1.61 V in the radiative limit. Our cell shows a V_{OC}, prior to halide segregation, of 1.16 V, suggesting an initial $EQE_{EL} \sim 10^{-8}$ (from Equation 5.6). The situation is similar in our FACs based 1.77 eV bandgap device, which in the radiative limit would deliver a 1.49 V V_{OC}, However, the device exhibits a V_{OC}, prior to halide segregation of 1.105 V, suggesting an initial $EQE_{EL} \sim 10^{-6}$. The non-radiative V_{OC} loss in this instance (385 mV) is over five times the segregation loss (75mV). Clearly, the V_{OC} loss due to non-radiative recombination is much more overwhelming than the loss from segregation. In comparison, the best perovskite cells (~1.6eV) have non-radiative losses of approximately 60 mV[31]. If this is achieved for 1.94 and 1.77 eV bandgap cells, they would deliver a V_{OC} of 1.54 and 1.43 V respectively, prior to halide segregation. Hence, even if halide segregation occurred, and induced a voltage penalty to the same extent that we have measured here, we would still

reach open-circuit voltages of 1.42 V and 1.33 V for the 1.94 eV and 1.77 eV bandgap cells respectively.

Therefore, the performance of mixed-halide perovskites is predominantly limited by trap-assisted non-radiative recombination and not halide-segregation. The problem in mixed-halide perovskites seems to be two-fold: a) non-radiative recombination within the perovskite absorber and b) Interfacial non-radiative recombination at the perovskite/charge extraction layer heterojunctions. In our 1.77 eV bandgap FACs based devices, the Urbach energy, which represents electronic disorder in the continuum of states, is low at only 15meV. This indicates that the poor quality does not arise from electronic disorder in the bands. We measure a PLQE of approximately 0.3% for the isolated perovskite film on glass. In comparison, the PLQE of the best metal halide perovskite films (~1.6 eV bandgap) is over 10%. Therefore, efforts are required to minimise the defects responsible for non-radiative recombination in these wider band gap mixed-halide perovskites. A further significant loss occurs due to the poor electronic quality of the perovskite/charge-transport-layer heterojunctions. Considering the difference between the inferred EQE_{EL} (10^{-6}) and the PLQE of the isolated perovskite film (10^{-3}), we infer that the contact materials quench the PLQE by three orders of magnitude. From this perspective, the electron-transport layer Phenyl-C61-butyric acid methyl ester (PCBM) is particularly deleterious, since it significantly quenches the PLQE of our 1.77 eV gap perovskite films to below our

detector limit (0.01%). By considering these absolute radiative efficiency values, we can estimate that the non-radiative losses from within the 1.77 eV gap perovskite absorber are responsible for ~180 mV loss in V_{OC}, and the integration into the device induces a further ~180 mV loss, with the latter primarily governed by the charge extraction layer/perovskite heterojunctions.

Thus, as a first priority, improved transport layers have to be identified by a systematic study of PL quenching, using the approach demonstrated by Stolterfoht. M. et al[32]. The development of new transport layers with new doping strategies to enable better band alignment, is also essential. Efforts to optimise the crystallisation and passivation of defects are also needed to eventually bring the PLQE of wide bandgap films on par with the best 1.6 eV bandgap films (~10%)

As a final note, halide segregation has itself been found to correlate positively with the fraction of non-radiative recombination in the film.[8] In addition, halide segregation has been shown to be highly suppressed in perovskite films with lower trap densities[8,33,34]. We may therefore postulate that it is the accumulated trapped charge which offers the electrostatic driving force for halide-segregation. We therefore expect that the route to maximise the radiative efficiency via reducing the trap density in the mixed-halide perovskites will not only maximise the initial V_{OC}, but will also likely overcome halide segregation itself.

5.10 Conclusions

In conclusion, we have quantified the impact of halide-segregation upon the open-circuit voltage (V_{OC}) of mixed-halide perovskite solar cells, using Fourier-Transform Photocurrent Spectroscopy (FTPS) measurements coupled with detailed balance calculations. Our results reveal that the V_{OC} loss from non-radiative recombination (~400 mV) is four to five times the loss from halide-segregation (~100 mV) in both FAMA (1.94 eV) and FACs (1.77 eV) based solar cells. These results represent the first quantitative evaluation of the contribution of halide-segregation towards the poor performance of mixed-halide perovskite cells. We suggest that currently, the performance of mixed-halide cells is limited by poor electronic quality of the perovskite cell which results in a low radiative efficiency, and not by halide segregation. The cause of this low radiative efficiency is twofold: a) perovskite absorber with a high degree of trap assisted non-radiative recombination and b) poor electronic quality of perovskite/charge-transport-layer heterojunctions, leading to “heterojunction-induced” non-radiative losses.

To reach higher open-circuit voltages, improving the radiative efficiencies of mixed-halide perovskite films, and developing more efficient perovskite/charge extraction layer interfaces should be viewed as a matter of priority. With such improved materials processing, we suggest that a V_{OC} of up to 1.33 V is within reach for a 1.77 eV perovskite, even if halide segregation remains unsuppressed.

Our work clearly highlights that the means to solve the voltage deficit issue in wide band gap mixed-halide cells, is to focus on reducing the initial defect density, and to neglect halide segregation as an issue, until improved radiative efficiency has been achieved. We also suggest that future studies on mixed-halide perovskites should include sensitive EQE_{PV} measurements coupled with detailed balance calculations to clearly differentiate V_{OC} loss due to halide-segregation and non-radiative recombination.

5.11 References

(1) Eperon, G. E.; Hörantner, M. T.; Snaith, H. J. Metal Halide Perovskite Tandem and Multiple-Junction Photovoltaics. *Nat. Rev. Chem.* **2017**, *1* (12), 0095. https://doi.org/10.1038/s41570-017-0095.

(2) Hoke, E. T.; Slotcavage, D. J.; Dohner, E. R.; Bowring, A. R.; Karunadasa, H. I.; McGehee, M. D. Reversible Photo-Induced Trap Formation in Mixed-Halide Hybrid Perovskites for Photovoltaics. *Chem. Sci.* **2015**, *6* (1), 613–617. https://doi.org/10.1039/C4SC03141E.

(3) Slotcavage, D. J.; Karunadasa, H. I.; McGehee, M. D. Light-Induced Phase Segregation in Halide-Perovskite Absorbers. *ACS Energy Lett.* **2016**, *1* (6), 1199–1205. https://doi.org/10.1021/acsenergylett.6b00495.

(4) Bischak, C. G.; Hetherington, C. L.; Wu, H.; Aloni, S.; Ogletree, D. F.; Limmer, D. T.; Ginsberg, N. S. Origin of Reversible Photoinduced Phase Separation in

Hybrid Perovskites. *Nano Lett.* **2017**, *17* (2), 1028–1033. https://doi.org/10.1021/acs.nanolett.6b04453.

(5) Brennan, M. C.; Draguta, S.; Kamat, P. V.; Kuno, M. Light-Induced Anion Phase Segregation in Mixed Halide Perovskites. *ACS Energy Lett.* **2018**, *3* (1), 204–213. https://doi.org/10.1021/acsenergylett.7b01151.

(6) Samu, G. F.; Janáky, C.; Kamat, P. V. A Victim of Halide Ion Segregation. How Light Soaking Affects Solar Cell Performance of Mixed Halide Lead Perovskites. *ACS Energy Lett.* **2017**, *2* (8), 1860–1861. https://doi.org/10.1021/acsenergylett.7b00589.

(7) Yoon, S. J.; Kuno, M.; Kamat, P. V. {<}i{>}Shift Happens{<}/I{>} . How Halide Ion Defects Influence Photoinduced Segregation in Mixed Halide Perovskites. *ACS Energy Lett.* **2017**, *2* (7), 1507–1514. https://doi.org/10.1021/acsenergylett.7b00357.

(8) Knight, A. J.; Wright, A. D.; Patel, J. B.; McMeekin, D. P.; Snaith, H. J.; Johnston, M. B.; Herz, L. M. Electronic Traps and Phase Segregation in Lead Mixed-Halide Perovskite. *ACS Energy Lett.* **2019**, *4* (1), 75–84. https://doi.org/10.1021/acsenergylett.8b02002.

(9) Rehman, W.; McMeekin, D. P.; Patel, J. B.; Milot, R. L.; Johnston, M. B.; Snaith, H. J.; Herz, L. M. Photovoltaic Mixed-Cation Lead Mixed-Halide Perovskites: Links between Crystallinity, Photo-Stability and Electronic Properties. *Energy Environ. Sci.* **2017**, *10* (1), 361–369. https://doi.org/10.1039/c6ee03014a.

(10) Hu, M.; Bi, C.; Yuan, Y.; Bai, Y.; Huang, J. Stabilized Wide Bandgap MAPbBr x I 3- x Perovskite by Enhanced Grain Size and Improved Crystallinity. *Adv. Sci.* **2016**, *3* (6), 1500301. https://doi.org/10.1002/advs.201500301.

(11) Zhou, Y.; Jia, Y.-H.; Fang, H.-H.; Loi, M. A.; Xie, F.-Y.; Gong, L.; Qin, M.-C.; Lu, X.-H.; Wong, C.-P.; Zhao, N. Composition-Tuned Wide Bandgap Perovskites: From Grain Engineering to Stability and Performance Improvement. *Adv. Funct. Mater.* **2018**, *28* (35), 1803130. https://doi.org/10.1002/adfm.201803130.

(12) Liu, Z.; Krückemeier, L.; Krogmeier, B.; Klingebiel, B.; Márquez, J. A.; Levcenko, S.; Öz, S.; Mathur, S.; Rau, U.; Unold, T.; Kirchartz, T. Open-Circuit Voltages Exceeding 1.26 v in Planar Methylammonium Lead Iodide Perovskite Solar Cells. *ACS Energy Lett.* **2019**, *4* (1), 110–117. https://doi.org/10.1021/acsenergylett.8b01906.

(13) Yang, T. C.-J.; Fiala, P.; Jeangros, Q.; Ballif, C. High-Bandgap Perovskite Materials for Multijunction Solar Cells. *Joule* **2018**, *2* (8), 1421–1436. https://doi.org/10.1016/j.joule.2018.05.008.

(14) Abdi-Jalebi, M.; Andaji-Garmaroudi, Z.; Cacovich, S.; Stavrakas, C.; Philippe, B.; Richter, J. M.; Alsari, M.; Booker, E. P.; Hutter, E. M.; Pearson, A. J.; Lilliu, S.; Savenije, T. J.; Rensmo, H.; Divitini, G.; Ducati, C.; Friend, R. H.; Stranks, S. D. Maximizing and Stabilizing Luminescence from Halide Perovskites with Potassium Passivation. *Nature* **2018**, *555* (7697), 497–501.

https://doi.org/10.1038/nature25989.

(15) Kirchartz, T.; Rau, U. Detailed Balance and Reciprocity in Solar Cells. *Phys. Status Solidi Appl. Mater. Sci.* **2008**, *205* (12), 2737–2751. https://doi.org/10.1002/pssa.200880458.

(16) Sze, S. M.; Ng, K. K. *Physics of Semiconductor Devices*; Jain, V. K., Verma, A., Eds.; Environmental Science and Engineering; Springer International Publishing: Cham, 2014. https://doi.org/10.1007/978-3-319-03002-9.

(17) Radziemska, E. Effect of Temperature on Dark Current Characteristics of Silicon Solar Cells and Diodes. *Int. J. Energy Res.* **2006**, *30* (2), 127–134. https://doi.org/10.1002/er.1113.

(18) Rau, U. Reciprocity Relation between Photovoltaic Quantum Efficiency and Electroluminescent Emission of Solar Cells. *Phys. Rev. B - Condens. Matter Mater. Phys.* **2007**, *76* (8), 1–8. https://doi.org/10.1103/PhysRevB.76.085303.

(19) Katsidis, C. C.; Siapkas, D. I. General Transfer-Matrix Method for Optical Multilayer Systems with Coherent, Partially Coherent, and Incoherent Interference. *Appl. Opt.* **2002**, *41* (19), 3978. https://doi.org/10.1364/AO.41.003978.

(20) Hoke, E. T.; Slotcavage, D. J.; Dohner, E. R.; Bowring, A. R.; Karunadasa, H. I.; McGehee, M. D. Reversible Photo-Induced Trap Formation in Mixed-Halide Hybrid Perovskites for Photovoltaics. *Chem. Sci.* **2015**, *6* (1), 613–617. https://doi.org/10.1039/C4SC03141E.

(21) Niklasson, G. A.; Granqvist, C. G.; Hunderi, O. Effective Medium Models for the Optical Properties of Inhomogeneous Materials. *Appl. Opt.* **2008**, *20* (1), 26. https://doi.org/10.1364/ao.20.000026.

(22) Eperon, G. E.; Stranks, S. D.; Menelaou, C.; Johnston, M. B.; Herz, L. M.; Snaith, H. J. Supplementary Information Formamidinium of Formamidinium Lead Trihalide: A Broadly Tunable Perovskite for Efficient Planar Heterojunction Solar Cells. *Energy Environ. Sci.* **2014**, *7* (3), 982. https://doi.org/10.1039/c3ee43822h.

(23) Yoon, S. J.; Draguta, S.; Manser, J. S.; Sharia, O.; Schneider, W. F.; Kuno, M.; Kamat, P. V. Tracking Iodide and Bromide Ion Segregation in Mixed Halide Lead Perovskites during Photoirradiation. *ACS Energy Lett.* **2016**, *1* (1), 290–296. https://doi.org/10.1021/acsenergylett.6b00158.

(24) Barker, A. J.; Sadhanala, A.; Deschler, F.; Gandini, M.; Senanayak, S. P.; Pearce, P. M.; Mosconi, E.; Pearson, A. J.; Wu, Y.; Srimath Kandada, A. R.; Leijtens, T.; De Angelis, F.; Dutton, S. E.; Petrozza, A.; Friend, R. H. Defect-Assisted Photoinduced Halide Segregation in Mixed-Halide Perovskite Thin Films. *ACS Energy Lett.* **2017**, *2* (6), 1416–1424. https://doi.org/10.1021/acsenergylett.7b00282.

(25) Jean, J.; Mahony, T. S.; Bozyigit, D.; Sponseller, M.; Holovský, J.; Bawendi, M. G.; Bulović, V. Radiative Efficiency Limit with Band Tailing Exceeds 30% for Quantum Dot Solar Cells. *ACS Energy Lett.* **2017**, *2* (11), 2616–2624.

https://doi.org/10.1021/acsenergylett.7b00923.

(26) Centurioni, E. Generalized Matrix Method for Calculation of Internal Light Energy Flux in Mixed Coherent and Incoherent Multilayers. *Appl. Opt.* **2005**, *44* (35), 7532. https://doi.org/10.1364/AO.44.007532.

(27) Nayak, P. K.; Mahesh, S.; Snaith, H. J.; Cahen, D. Photovoltaic Solar Cell Technologies: Analysing the State of the Art. *Nat. Rev. Mater.* **2019**, *4* (4), 269–285. https://doi.org/10.1038/s41578-019-0097-0.

(28) Yuan, M.; Quan, L. N.; Comin, R.; Walters, G.; Sabatini, R.; Voznyy, O.; Hoogland, S.; Zhao, Y.; Beauregard, E. M.; Kanjanaboos, P.; Lu, Z.; Kim, D. H.; Sargent, E. H. Perovskite Energy Funnels for Efficient Light-Emitting Diodes. *Nat. Nanotechnol.* **2016**, *11* (10), 872–877. https://doi.org/10.1038/nnano.2016.110.

(29) Deschler, F.; Price, M.; Pathak, S.; Klintberg, L. E.; Jarausch, D. D.; Higler, R.; Hüttner, S.; Leijtens, T.; Stranks, S. D.; Snaith, H. J.; Atatüre, M.; Phillips, R. T.; Friend, R. H. High Photoluminescence Efficiency and Optically Pumped Lasing in Solution-Processed Mixed Halide Perovskite Semiconductors. *J. Phys. Chem. Lett.* **2014**, *5* (8), 1421–1426. https://doi.org/10.1021/jz5005285.

(30) Hörantner, M. T.; Leijtens, T.; Ziffer, M. E.; Eperon, G. E.; Christoforo, M. G.; McGehee, M. D.; Snaith, H. J. The Potential of Multijunction Perovskite Solar Cells. *ACS Energy Lett.* **2017**, *2* (10), 2506–2513. https://doi.org/10.1021/acsenergylett.7b00647.

(31) Jiang, Q.; Zhao, Y.; Zhang, X.; Yang, X.; Chen, Y.; Chu, Z.; Ye, Q.; Li, X.; Yin, Z.; You, J. Surface Passivation of Perovskite Film for Efficient Solar Cells. *Nat. Photonics* **2019**, *13* (7), 460–466. https://doi.org/10.1038/s41566-019-0398-2.

(32) Stolterfoht, M.; Wolff, C. M.; Márquez, J. A.; Zhang, S.; Hages, C. J.; Rothhardt, D.; Albrecht, S.; Burn, P. L.; Meredith, P.; Unold, T.; Neher, D. Visualization and Suppression of Interfacial Recombination for High-Efficiency Large-Area Pin Perovskite Solar Cells. *Nat. Energy* **2018**, *3* (10), 847–854. https://doi.org/10.1038/s41560-018-0219-8.

(33) McMeekin, D. P.; Wang, Z.; Rehman, W.; Pulvirenti, F.; Patel, J. B.; Noel, N. K.; Johnston, M. B.; Marder, S. R.; Herz, L. M.; Snaith, H. J. Crystallization Kinetics and Morphology Control of Formamidinium-Cesium Mixed-Cation Lead Mixed-Halide Perovskite via Tunability of the Colloidal Precursor Solution. *Adv. Mater.* **2017**, *29* (29), 1607039. https://doi.org/10.1002/adma.201607039.

(34) McMeekin, D. P.; Sadoughi, G.; Rehman, W.; Eperon, G. E.; Saliba, M.; Horantner, M. T.; Haghighirad, A.; Sakai, N.; Korte, L.; Rech, B.; Johnston, M. B.; Herz, L. M.; Snaith, H. J. A Mixed-Cation Lead Halide Perovskite Absorber for Tandem Solar Cells. *Science (80-.).* **2016**, *351* (6269), 151–155. https://doi.org/10.1126/science.aad5845.

6

Factors Limiting the Performance of $Cs_2AgBiBr_6$ based Perovskite Solar Cells

The results presented in this chapter are largely contained in the following article:

Longo, G.; **Mahesh, S**.; Buizza, L. R. V.; Wright, A. D.; Ramadan, A. J.; Abdi-Jalebi, M.; Nayak, P. K.; Herz, L. M.; Snaith, H. J. **Understanding the Performance-Limiting Factors of $Cs_2AgBiBr_6$ Double-Perovskite Solar Cells.** ***ACS Energy Lett.*** **2020, 2200–2207**. https://doi.org/10.1021/acsenergylett.0c01020.

6.1 Overview

The commercialisation of perovskite-based multi-junctions demands the development of highly efficient and stable wide-gap absorbers. The most popular wide-gap perovskites— members of the $FA_{1-x}Cs_xPbI_yBr_{1-y}$ family—not only suffer from significant photo instability but are also prone to degradation. Double perovskites have recently emerged as more stable alternatives to Pb based

perovskites. In particular, the wide-bandgap double perovskite $Cs_2AgBiBr_6$ has been the subject of several studies because of its environmental stability, low toxicity, and its promising optoelectronic features. Despite these encouraging features, the performance of solar cells based on this double perovskite is still low, necessitating a study of electronic and optical loss mechanisms. In this work we combine experiment and modelling to reveal that short electron diffusion length underpins the poor short-circuit current seen in $Cs_2AgBiBr_6$ based solar cells. Our findings point to an important materials issue that must be attended to with priority to bring $Cs_2AgBiBr_6$ solar cells on track towards maturity.

6.2 Introduction

Despite the impressive photovoltaic performance of hybrid perovskite materials, significant roadblocks exist towards the commercialisation of multi-junctions. As has already been explained in previous chapters, the lack of high-performance wide-bandgap perovskites is one major barrier. Furthermore, even the best perovskite-based cells currently have much lower operating lifetimes in the ambient (thousands of hours)[3] than traditional inorganic semiconductor based cells (~10 years). The volatility of the organic cation is a major contributor to this instability[4,5], and can be supressed by using inorganic cations. However, attempts to exploit the inorganic $CsPbX_3$ perovskite family have been thwarted by the intrinsic thermodynamic instability of the photoactive phase at room

temperature[6]. Additionally, there are further concerns from the presence of lead, as well as the almost exclusive use of toxic solvents in solution processing. While initial studies indicate that the associated risk of the use of lead is small, when deployed in utility scale solar, this is still far from conclusive[7]. Moreover, social barriers towards the use of lead may also be difficult to overcome. For these reasons the search for less toxic alternative inorganic perovskites is of immediate interest, especially when the bandgap is upwards of 1.7 eV. The perovskite crystal structure admits a staggering number of elements with a wide variety of configurations[8]. The search is on for the model perovskite that retains the near-ideal optoelectronic properties (long diffusion length, low trap density, direct-bandgap ideally between 1-1.8 eV), while simultaneously being stable in the long term.

In this landscape, double-perovskites have recently emerged as particularly promising alternatives[9,10] exhibiting encouraging optoelectronic properties, high environmental stability and low toxicity. In the double-perovskite crystal, Pb^{2+} is replaced by alternating monovalent and trivalent metal cations, thus preserving an average divalency. The resulting three-dimensional structure takes the form $A_2M'M''X_6$, where A is a monovalent cation, M' and M'' are monovalent and trivalent metal ions respectively, and X is a halide anion. Initial computational studies pointed to pnictogens (Bi^{3+} and Sb^{3+}) and noble metals (Cu^{+}, Ag^{+}, Au^{+}) as optimal substitutes for Pb^{2+}, due to their stable oxidation states, high conductivity in the

metallic form, and ionic radii comparable to Pb^{2+} in an octahedral environment[11,12]. Recent work on the $Cs_2M'M''X_6$ family (M'=Au^+, Ag^+, Cu^+ and M''=Bi^{3+}, Sb^{3+}) has revealed encouraging optoelectronic properties: visible to near infrared absorption[13–15], relatively small carrier effective mass[16] and bright emission[17,18].

In particular, the wide-bandgap double perovskite $Cs_2AgBiBr_6$ has been the subject of much fundamental material characterisation and initial application in photodetectors and photovoltaic devices[15,19–22]. While the absorption onset (>2.3 eV) is far too large for even multi-junction applications, the system serves as a useful testbed for understanding the properties of the yet-unexplored AgBi semiconductor family. So far, material characterisation and calculations suggest promising features: single-crystal carrier lifetime of 1 μs, moderate charge-carrier mobility, and an absorption-edge in the visible[23]. However, despite these favourable characteristics, the best reported photovoltaic power conversion efficiency (PCE) for a planar heterojunction solar cell is still only 2.51%[24], with an open circuit voltage (V_{OC}) of 1.01 V, fill factor (FF) of 0.65 and short-circuit current (J_{SC}) of 3.82 mA cm^{-2}. It is historically common that incipient PV technologies suffer from large voltage deficits, which gradually reduce as material processing improves and as methods to passivate defects are discovered[25]. However, the severely inhibited J_{SC} is unusual, and could prove to be a major barrier to high performance. Furthermore, due to the indirect bandgap of $Cs_2AgBiBr_6$, thick

absorber films, on the order of tens to hundreds of microns, would be necessary to substantially increase the photocurrent generation, but this would require extremely long charge-carrier diffusion lengths. For this reason, the design of devices depends crucially on knowing the charge-carrier mobility and the diffusion length. A clear evaluation of these parameters in this material is still missing, and to date, several different values have been reported[23,26–28].

Here, we undertake a thickness-dependent study of vapour deposited $Cs_2AgBiBr_6$–based solar cells. We evaluate the carrier diffusion length based on a combination of external quantum efficiency (EQE) measurements on semi-transparent devices and optical modelling, and compare it to values we estimate using terahertz photoconductivity spectroscopy and time resolved photoluminescence. Our work reveals that short electron diffusion length, on the order of a few tens of nanometers, is the cause for low short-circuit current densities reported in these solar cells. We also perform photo-thermal deflection spectroscopy (PDS) and surface photovoltage measurements (SPV) and correlate this short electron diffusion length with the presence of a high density of electron traps. We suggest that the electron diffusion lengths in $Cs_2AgBiBr_6$ must be improved as a matter of priority, in order to achieve better performance. Such improvements, likely driven by reduction in trap densities, would also increase open-circuit voltages and reduce hysteresis.

6.3 Material Properties

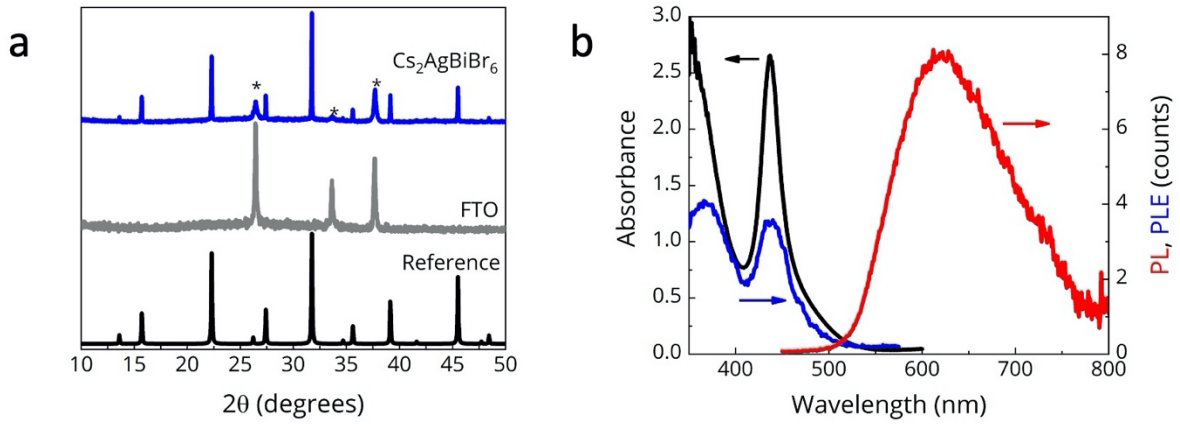

Figure 6.1 | **a)** XRD pattern from an evaporated and annealed $Cs_2AgBiBr_6$ thin film on FTO. **b)** Absorbance (black curve), PL excitation spectrum (PLE, blue curve, recorded at 600 nm emission peak) and PL spectrum (red curve, excitation at 405 nm) from a $Cs_2AgBiBr_6$ thin film deposited on quartz. Devices fabricated and measured by Giulia Longo.

We prepared thin films of $Cs_2AgBiBr_6$ through sequential evaporation, as described in the chapter *Methods*. To assess the formation of the double-perovskite, we performed X-ray diffraction (XRD) measurements on thin-films deposited on FTO. The sharp peaks in the XRD pattern (Figure 6.1a) of the evaporated material validate its high crystallinity and signal the absence of any additional phases or unreacted precursors. Optical properties measured on a quartz substrate (absorbance, photoluminescence spectra (PL), photoluminescence excitation (PLE) spectra) are presented in Figure 6.1b, and are consistent with previous reports[15,29,30]. The films exhibit strong and increasing absorption below 400 nm, which has been identified with the direct bandgap at ~ 3 eV. The strong peak at 440 nm is still subject of controversy: some identify it with

a tightly bound exciton at the direct bandgap edge, while others ascribe it to a strong transition between the Bi^{3+} s-p orbitals, without bound character[31,32]. The weak absorption tail beyond 440 nm is considered to be the indirect bandgap. The large Stokes shift between absorption and emission, the similarity between the absorption and PLE spectra, and the independence of the PLE spectra from the probe wavelength are often indications of charge-lattice interaction mechanisms, like polaron formation, self-trapped excitons or colour-centre formations, as previously reported in other works[33–35]. It is beyond the scope of this work to discuss this further, but we still highlight that ambiguities around the nature of photoexcitation and emission in this material persist.

6.4 Solar Cell Characterisation

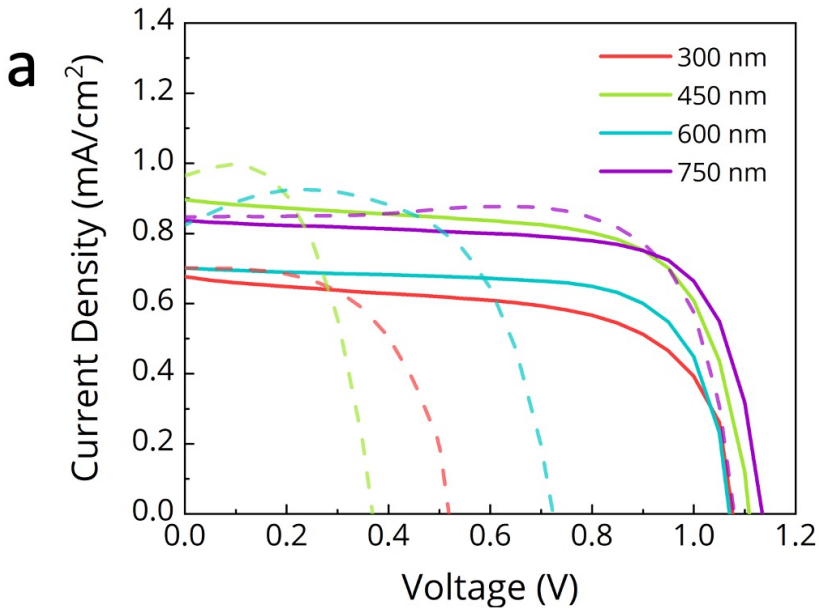

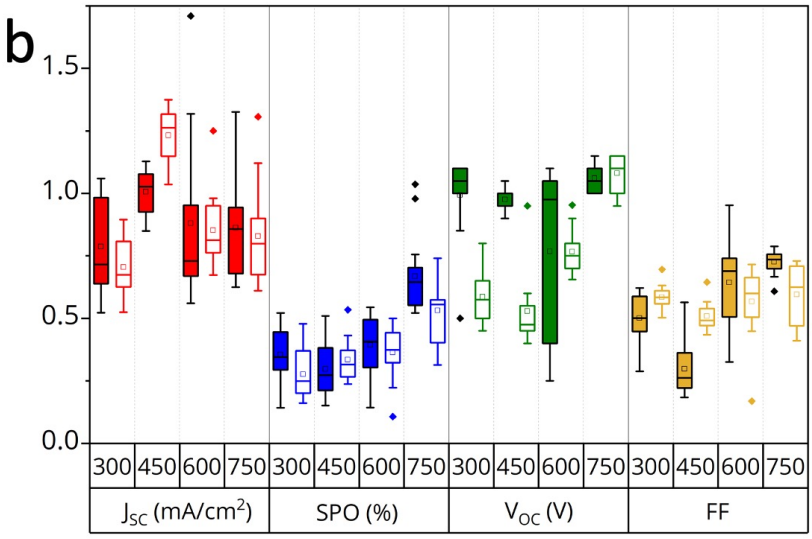

Figure 6.2 | a) JV curves of solar cells with different thicknesses of $Cs_2AgBiBr_6$. Forward scans are dashed and reverse scans are solid. **b)** J_{SC}, PCE, V_{OC} and FF as a function of absorber thickness in nm. Devices fabricated and characterised by Giulia Longo.

Table 6.1 Figures of merit for solar cell devices with different $Cs_2AgBiBr_6$ absorber thicknesses.

	300 nm	450 nm	600 nm	750 nm
PCE (%)	0.468	0.686	0.535	0.696
J_{SC} (mA cm^{-1})	0.676	0.896	0.702	0.837
V_{OC} (V)	1.10	1.10	1.05	1.15
FF (%)	62	68	73	71
SPO (%)	0.523	0.595	0.431	0.609

We prepared double-perovskite n-i-p cells with different active layer thicknesses. The structure of the fabricated n-i-p cell is FTO/TiO_2 /$Cs_2AgBiBr_6$/Spiro-OMeTAD/Ag. In figure 6.2a we present the JV curves of the best

devices for each film thickness, while in figure 6.2b and table 6.1 we present the corresponding figures of merit. The champion device had a 750 nm thick absorber, and was measured to have a PCE of 1.03%, with an open-circuit voltage (V_{OC}) of 1.10 V, short-circuit current (J_{SC}) of 1.33 mA cm^{-2} and a fill-factor (FF) of 0.70, which are comparable to previous reports[21,36,37]. Rather surprisingly, we do not observe any correlation of the device performance with the active layer thickness, as table 6.1 shows.

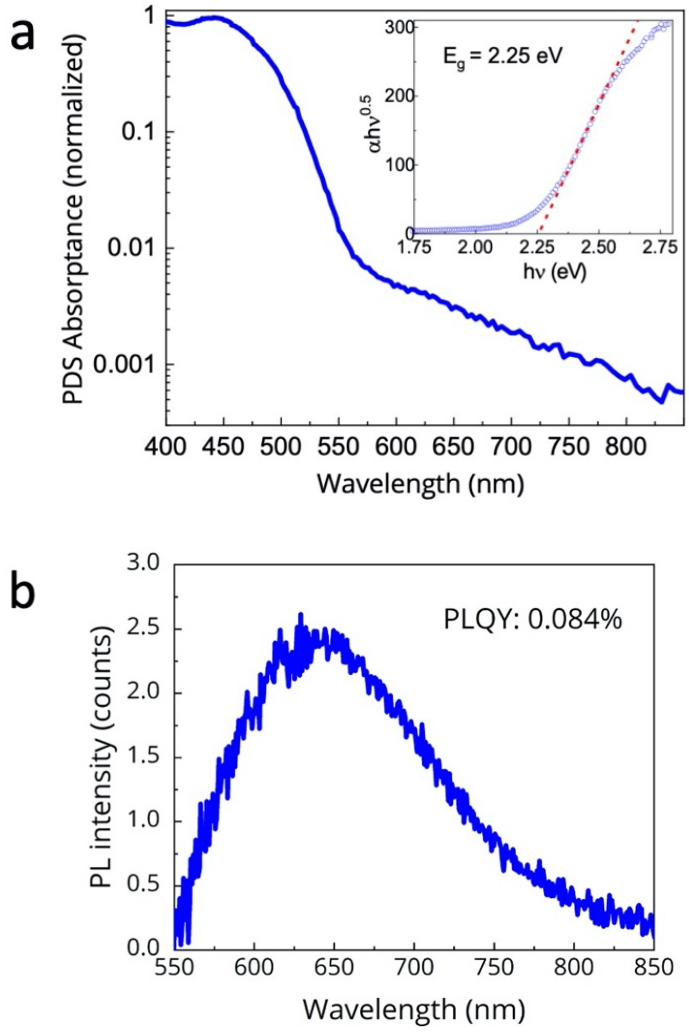

Figure 6.3 | a) Absorptance of a neat $Cs_2AgBiBr_6$ film on quartz glass, measured using PDS. Inset: Tauc plot with the calculated indirect bandgap. Measurement performed by Mojtaba Abdi-Jalebi. **b)** PL spectrum and PLQY of a $Cs_2AgBiBr_6$ thin film measured in an integrating sphere after exciting with a 405 nm laser. Measurement performed by Suhas Mahesh.

The inset to figure 6.3a contains a Tauc plot from which we determine the indirect bandgap to be at 2.25 eV, similar to previous reports[15,16]. For such an absorber, the thermodynamic limit for PV performance (with the Shockley-Queisser assumptions[38]) would be 17.6%, with V_{OC} =1.93 V and J_{SC} =9.79 mA cm^{-2}. Every 60 mV loss in V_{OC}, as measured from the thermodynamic limit, corresponds to an order-of-magnitude reduction in the EQE_{EL}[39–41]. Our devices exhibit a large voltage deficit of ~800 mV, suggesting an extremely low EQE_{EL} of ~10^{-13} for a full device with 1 sun equivalent injection. In comparison, the best inorganic-organic perovskite cells have EQE_{EL} ~ 0.1. This is indicative of an extremely high rate of non-radiative recombination, which in turn indicates extremely large trap densities. We investigate the sub-band gap absorption in these thin films using photothermal deflection spectroscopy (PDS, Figure 6.3a). PDS reveals a shallow absorption edge with an Urbach energy of 70 meV, and significant panchromatic absorption reaching down to 1000 nm. This is consistent with a large density of sub-bandgap states, which could be expected to mediate fast non-radiative recombination. We measured the PL quantum yield (PLQY) of neat $Cs_2AgBiBr_6$ thin films on glass (Figure 6.3b) to be ~0.08% (~10^{-4}). Although this value is low in comparison to lead halide perovskites (~10%), it is orders of magnitude higher than the 10^{-13} that we previously calculated from the V_{OC}. Even in the radiative limit, the shallow absorption onset and the presence of such sub-bandgap states

can be expected to significantly limit the open-circuit voltage in PV devices. This is due to the dark recombination current density (J_0) being proportional to the overlap integral of the black body spectrum under ambient temperature (300K), and the absorption spectrum of the solar absorber material. Since the 300K black body spectrum increases exponentially moving towards lower energy, this factor, J_0, is highly sensitive to small changes in both the steepness of the absorption onset[41]. Furthermore, interfacial recombination at the absorber-transport layer heterojunctions is usually responsible for the bulk of the PL quenching in lead-halide perovskite PV cells. This problem is especially problematic for wider band gap absorbers[41], where there has been little work on tailoring transport layers for the energetics of the absorber. Therefore, improvements in V_{OC} are likely possible if transport layers tailored to the energetics of $Cs_2AgBiBr_6$ can be made. Historically, PV technologies have started off with hundreds of millivolts of voltage deficit, which is then slowly overcome as materials processing improves. However, the very low photocurrent density observed in these cells, representing a loss of ~ 90% of the absorbed photons, is not typical, even for incipient materials. Consequently, this is an important issue that merits immediate attention.

6.5 Estimating Diffusion Length

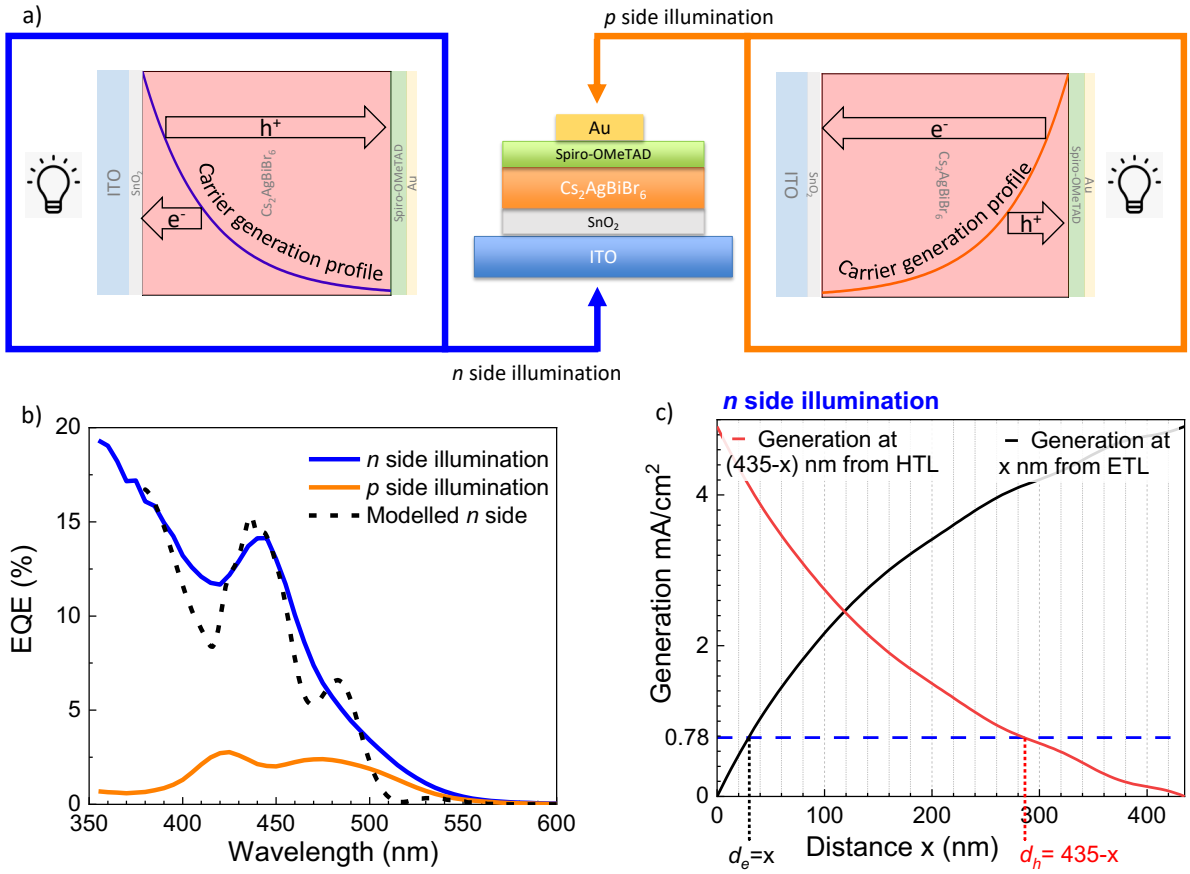

Figure 6.4 | **a)** Schematic illustration of the device structure used in the double-side EQE measurement and the two measurement conditions, with the corresponding carrier generation profile. **b)** EQE measured with illumination through the n side (blue curve), through the p side (orange curve) and the modelled n side EQE (black dashed curve). c) Current generation at a distance x from the ETL (black curve) and from a distance 435-x from the HTL (red curve) in the case of n-side illumination. The dotted blue line indicates the current obtained from the integration of the n sided EQE. Measurements and simulation performed by Suhas Mahesh.

To resolve the puzzle of the high photocurrent loss, we investigate the charge transport and photocurrent generation in complete $Cs_2AgBiBr_6$ solar cells and thin film. We first fabricated semi-transparent PV cells with 435 nm of the $Cs_2AgBiBr_6$ absorber and measured their photovoltaic external quantum efficiency (EQE) spectra through front illumination (through the *n* side), and rear illumination

(through the *p* side), which we schematically represent in Figure 6.4a. When illuminated through the *n* side, the EQE (blue curve in Figure 6.4b) has a peak of ~15%, which very closely matches the absorption spectrum in shape, and has an integrated current of 0.78 mA cm^{-2}. When illuminated through the *p* side, the EQE (orange curve in Figure 6.4b) peaks at only 2.5% and has a shape that counter-correlates with the absorption spectrum and gives an integrated current of 0.16 mA cm^{-2}. We note that the light attenuation from the 20 nm thick "semi-transparent" gold (~20% at 450 nm) is not sufficient to account for this effect. To understand these results, we have to consider that as light passes through the perovskite, its intensity decays exponentially with depth accordingly to the Beer-Lambert law. This means that the density of generated carriers will be higher closer to the transport layer from which light enters the device (*i.e.* higher density close to the electron-transport layer (ETL) for *n* side illumination, and higher density close to the hole-transport layer (HTL) for *p* side illumination, as represented by the carrier generation profile curves in Figure 6.4a). Consequently, with the *n* side illumination, holes will have to travel a longer path to be extracted, as compared to electrons, while for *p* side illumination electrons will have to travel further than holes to reach the ETL. From the EQE in figure 6.4b, it is clear that the *p* side EQE is much lower than the *n* side EQE, indicating that when electrons have to travel across the entire active layer thickness, they cannot be efficiently collected. Furthermore, the *p* side EQE also shows an "inversion" in shape in

comparison to the *n* side EQE and to the absorption spectrum: the peak in the absorption at 440 nm, corresponds to a dip in the *p* side EQE. This happens because wavelengths that are strongly absorbed do not reach the far-end (electron-transporting layer in this case), causing a dip. Weakly absorbed wavelengths, instead, propagate to the far end in greater numbers, appearing as peaks. In contrast, the *n* side EQE spectrum very closely follows the absorption spectra, with the clearly defined peak at 440 nm, rather than the total absorptance spectrum, which for this 435 nm thick film is much broader. This observation is consistent with only a very thin section of the film near the electron extraction layer contributing to photocurrent generation.

These considerations lead us to conclude that electron diffusion is the factor limiting the short-circuit current of $Cs_2AgBiBr_6$ solar cells. We then combined our EQE data with an optical model (generalised transfer matrix method) to obtain a quantitative estimation of the electron and hole diffusion length in our devices (Figure 6.4c). For this, we made the following consideration: if the diffusion length of electrons is d_e, we assume that only electrons generated within a length d_e from the ETL will be collected. We make the same assumption for the diffusion length of holes d_h, and undertake that the overall short-circuit current in the device will be governed by the smaller of the electron and hole currents. We then modelled the carrier generation profile as a function of incident light wavelength using the generalised transfer matrix method, and estimated the total light absorbed as a

function of wavelength within a length *d* of a transport layer. This allowed us to reconstruct the EQE spectrum for every value of *d,* with the assumption of an abrupt interface at *d*: all light absorbed within *d* is converted to collected photocurrent, while all light absorbed beyond *d* is lost. Additionally, we assume that the solar cell current is equal to the smaller between electron and hole currents. Assuming *n* side illumination, we varied *d* until the modelled EQE best approximated the measured spectrum, which we show in Figure 6.4b and c. This tells us that under these assumptions, the electron diffusion length d_e is ~30 nm and that the hole diffusion length d_h> 150nm. We executed the same procedure for the *p* side illumination. However, we remark that the unavailability of the optical constants of the thin gold semi-transparent electrode causes an underestimation in the EQE modelled for *p* side illumination. We also note that the interference fringes visible in our modelled EQE spectrum (Figure 6.4b), which are not replicated in the experimental data, are likely to reflect that the material interfaces are not perfectly smooth in the real devices, as required for coherent optical interference.

6.6 Terahertz Mobility Measurements

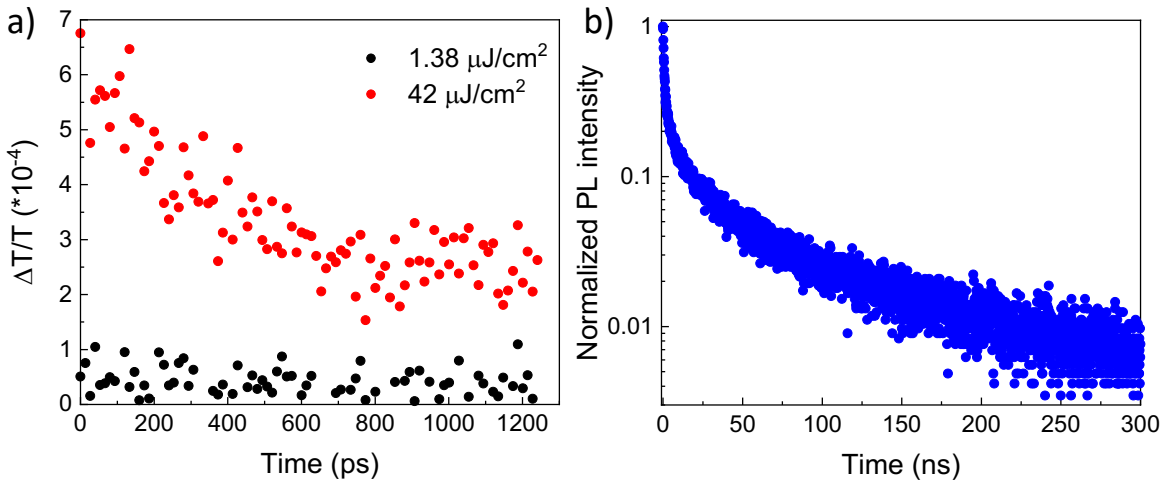

Figure 6.5 | **a)** Transient OPTP decay of a $Cs_2AgBiBr_6$ thin-film deposited on z-cut quartz and **b)** Time resolved photoluminescence decay, measured close to the peak PL wacelength with an excitation fluence of 0.24 μJ/cm^2. In both cases excitation wavelength was 400 nm. Measurements performed by Leonardo R. V. Buizza and Adam D. Wright.

To further investigate charge-carrier mobility, and to corroborate the above estimated carrier diffusion lengths (d_e ~30nm, d_h> 150nm), we performed optical-pump-terahertz-probe (OPTP) photoconductivity measurements. Terahertz radiation probes the dielectric response of a medium in the low-frequency range, allowing the examination of charge-carriers present, as they modify the conductivity at THz frequencies. OPTP spectroscopy offers the possibility to time-resolve changes in the electric field amplitude ($\Delta T/T$) of a single-cycle terahertz pulse transmitted to a sample as a function of time delay after optical excitation. The measured transient signal allows us to evaluate the change in the photoconductivity (ΔS) of photoactive materials, and from there, it is possible to

calculate the sum of electron and hole mobilities for the material ($\Sigma\mu$) from the initial $\Delta T/T$ values, as expressed in Equation 6.1[26,36,42,43].

$$\Delta S \propto \phi \Sigma \mu \propto \frac{\Delta T}{T} \qquad 6.1$$

Here ϕ is the free-charges to absorbed photons branching ratio. The fraction of free carriers generated from a single photon upon photogeneration (the branching ratio ϕ) is a fundamental parameter for the correct evaluation of the mobility, as the measured photoconductivity is generated only from free carriers rather than bound species as excitons. Given that the branching ratio is $0 \leq \phi \leq 1$, the calculated effective charge-carrier mobility is always an underestimation; only in the case of full conversion of photons to free charges our value reflects the true mobility. Importantly, our calculated value of μ arises from changes in photoconductivity due to both electrons and holes, meaning we calculate an overall sum mobility. We report the results in Figure 6.5a. Our OPTPs measurements give an effective sum mobility of $\phi\Sigma\mu = 0.74 \pm 0.29$ cm^2 V^{-1} s^{-1} in good agreement with previous measurements carried out by Time-Resolved Microwave Conductivity[26]. The charge-carrier diffusion length can be calculated, knowing the diffusion co-efficient D (Equation 6.2), as shown in Equation 6.3.

$$D = \frac{k_B T}{q}\mu \qquad 6.2$$

$$L_D = \sqrt{\frac{D}{R_T(n)}} \qquad 6.3$$

Here T is the temperature, k_B the Boltzmann constant, q the elementary charge and $R_T(n)$ is the charge-carrier recombination rate. In order to estimate the charge-carrier lifetime, and hence recombination rate, we performed time correlated single photon counting (TCSPC), and present the time resolved PL decay in Figure 6.5b. The highly heterogeneous nature of the PL decay has been previously reported, both in thin films and single crystals[26,44]. The full transient can therefore be fitted by a stretched exponential function with a mean lifetime of τ_{av} = 10 ns. However, to obtain a PL lifetime that is more representative of the time window of the OPTP measurements, we instead fit a mono-exponential function only between 0 and 1.2 ns to obtain a PL lifetime of of τ = 1.3 ns. Following the convention of Richter et al.[45], we double the fitted lifetime in order to extract our charge-carrier recombination rate, so that $k_1 = 1/2\tau_{meas}$, giving values for k_1 of 5–38.5*10^7 s^{-1}. We thus approximate $R_T(n) \sim k_1$, and calculate values of 70-200 nm for the diffusion length. Although THz photoconductivity measurements cannot distinguish between electron and hole contributions to the charge-carrier mobility, providing a sum mobility, these diffusion lengths are in good agreement with the values obtained from our EQE model above. Alternatively, this mobility estimated by THz spectroscopy, is also likely to represent an upper estimate of the long-range mobility in the solar cell devices, where charge conduction is sensitive to scattering events on longer length scales.

6.7 Surface Photovoltage Measurements

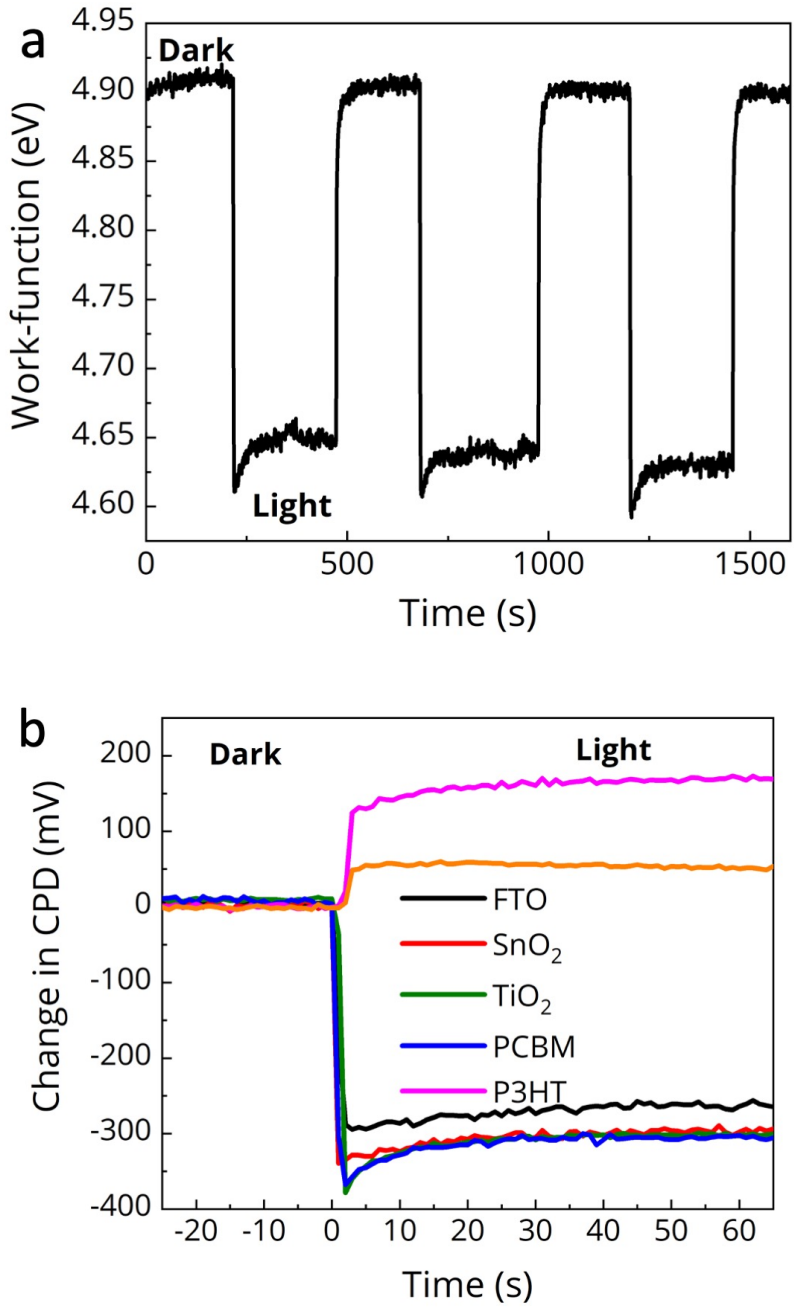

Figure 6.6 | **a)** Work-function of a $Cs_2AgBiBr_6$ thin-film on FTO in dark and under white light. **b)** Contact potential difference of a $Cs_2AgBiBr_6$ thin-film on different charge carriers transport material. Measurements performed by Pabitra K. Nayak.

In the previous sections, we have provided evidence for large trap densities (via PDS measurements) and poor electron diffusion length. To understand the nature of these trap states, we performed Kelvin probe surface photovoltage (SPV) measurements on a double-perovskite thin film deposited on top of FTO substrates and on different transport layers. Kelvin probe is a non-invasive technique that allows us to evaluate the work-function of the material of interest through capacitance measurements between the sample and an oscillating tip of known work-function. We determine the work-function of $Cs_2AgBiBr_6$ thin film deposited on FTO, measured in dark and nitrogen atmosphere, to be 4.91 eV, which is very close to the value of 4.94 eV, which we obtained from ultraviolet photoelectron spectroscopy (UPS) measurements (performed by Alexandra Ramadan). Knowing that the optical bandgap is ~ 2.25 eV and assuming a negligible exciton binding energy, this indicates that we expect the position of the conduction band minimum (CBM) at ~ 4.55 eV. Therefore, the position of the fermi level would appear closer to the CBM, suggesting that our sequentially evaporated Cs2AgBiBr6 thin film is n-type in nature. This result stands in contrast to previously reported works in which this double perovskite has been presented as a p-type semiconductor[23,46,47]. Our results indicate that sequentially evaporated $Cs_2AgBiBr_6$ thin films present an n-type character, possibly related to Br^- vacancies[48] as has been previously inferred[24]. However, we also note that UPS measurements probe the electronic structure of the outermost surface of a

sample. Therefore, the presence of defects on the surface would easily account for the discrepancies between our measurements and previous reports

We present surface photovoltage (SPV) measurements of the double perovskite films on FTO and on different transport layers in Figure 6.6a and b respectively. SPV measures the change in the contact potential difference (CPD) between the sample surface and the Kelvin probe tip when the sample is illuminated. It is defined as $SPV=CPD_{light}-CPD_{dark}$.[49] By calibrating the Kelvin probe tip with a reference, it is possible to correlate the contact potential difference with the sample work-function. Generally, a semiconductor has some degree of band bending in the surface region, due to the trapping of the majority carrier into surface states or due to preferential trapping of one type of the carrier. Accordingly, from the direction of the potential bending, and its change with illumination, it is possible to gain information on the surface states of the semiconductor material investigated. Upon photoexciting above the band gap, photo-generated electrons will drift away from the band bending region, while holes will move to the surface, reducing the band-bending. In Figure 6.6a the SPV of the evaporated double-perovskite on FTO is reported. Under illumination, the work-function decreases, generating a SPV of almost -250 mV. Considering the n-type character of the material, a negative SPV indicates a reduction of the potential bending, consistent with the presence of electron traps. Interestingly, we observe that under illumination, the CPD (and, consequently, the calculated

work-function) has an unsteady behaviour, flattening after several seconds of light exposure. The large time scale necessary for its stabilization suggests that this phenomenon is due to a slow process, likely ionic movement. However, this behaviour is fully reversible, since the work-function is the same even after several cycles of illumination. We also evaluated the SPV of the double perovskite on different hole and electron transport layers (Figure 6b). All the CPD_{dark} values were set to 0 mV, in order to facilitate the comparison between the different samples. When the double perovskite is deposited on top of electron transport materials (as SnO_2, TiO_2 or PCBM), the SPV value becomes slightly more negative than on FTO, reaching values of -300 mV. This is because when electron-hole pairs are created under illumination, electrons are selectively extracted by the transport material at the interface, leaving a higher hole concentration than on FTO. The leftover holes annihilate the trapped electron at the surface, decreasing the band-bending even further. On the contrary, when a hole transport material is used as underlying layer (such as Spiro or P3HT), the SPV becomes positive (+50 mV and +150 mV respectively). After photo-generation, holes get mostly extracted by the hole transport layer while electrons remain in the double-perovskite film increasing the surface band bending and creating a positive SPV. These results further confirm the presence of electron traps at the double perovskite surface, consistent with our evaluation of a low electron diffusion length.

6.8 Conclusions

To conclude, we fabricated $Cs_2AgBiBr_6$ thin-films and solar cells by sequential evaporation and investigated some photovoltaic loss mechanisms. Our thickness dependant study of photovoltaic performance revealed no correlation between performance and absorber thickness, serving as a smoking gun for diffusion limited transport. The transport was confirmed to be strongly electron diffusion limited (d_e~30 nm) by double sided EQE measurements coupled with optical modelling. This observation is further confirmed using THz spectroscopy, which evaluated a modest sum mobility of electrons and holes of less than 1 $cm^2 V^{-1} s^{-1}$. PDS measurements revealed the existence of a very shallow sub bandgap tail (E_{urbach} ~ 70 meV) suggesting the presence of large trap densities. These were confirmed to be electron traps by surface photovoltage measurements. This abundance of electron traps, we believe, is the most important materials issue limiting the performance of $Cs_2AgBiBr_6$ based cells at present. Understanding the origin of these traps, and finding routes to mitigate them will not only improve current extraction, but also improve open-circuit voltage by hundreds of millivolts, and reduce hysteresis.

6.9 References

(1) Shi, Z.; Guo, J.; Chen, Y.; Li, Q.; Pan, Y.; Zhang, H.; Xia, Y.; Huang, W. Lead-Free Organic-Inorganic Hybrid Perovskites for Photovoltaic Applications: Recent Advances and Perspectives. *Adv. Mater.* **2017**, *29* (16), 1605005. https://doi.org/10.1002/adma.201605005.

(2) Best Research-Cell Efficiency Chart https://www.nrel.gov/pv/cell-efficiency.html (accessed Apr 18, 2019).

(3) Meng, L.; You, J.; Yang, Y. Addressing the Stability Issue of Perovskite Solar Cells for Commercial Applications. *Nat. Commun.* **2018**, *9* (1), 5265. https://doi.org/10.1038/s41467-018-07255-1.

(4) Zhou, Y.; Zhao, Y. Chemical Stability and Instability of Inorganic Halide Perovskites. *Energy Environ. Sci.* **2019**, *12* (5), 1495–1511. https://doi.org/10.1039/C8EE03559H.

(5) Park, B.; Seok, S. Il. Intrinsic Instability of Inorganic–Organic Hybrid Halide Perovskite Materials. *Adv. Mater.* **2019**, *31* (20), 1805337. https://doi.org/10.1002/adma.201805337.

(6) Eperon, G. E.; Paternò, G. M.; Sutton, R. J.; Zampetti, A.; Haghighirad, A. A.; Cacialli, F.; Snaith, H. J. Inorganic Caesium Lead Iodide Perovskite Solar Cells. *J. Mater. Chem. A* **2015**, *3* (39), 19688–19695. https://doi.org/10.1039/C5TA06398A.

(7) Babayigit, A.; Ethirajan, A.; Muller, M.; Conings, B. Toxicity of Organometal Halide Perovskite Solar Cells. *Nat. Mater.* **2016**, *15* (3), 247–251. https://doi.org/10.1038/nmat4572.

(8) Filip, M. R.; Giustino, F. The Geometric Blueprint of Perovskites. *Proc. Natl. Acad. Sci.* **2018**, *115* (21), 5397–5402. https://doi.org/10.1073/pnas.1719179115.

(9) Chu, L.; Ahmad, W.; Liu, W.; Yang, J.; Zhang, R.; Sun, Y.; Yang, J.; Li, X. Lead-Free Halide Double Perovskite Materials: A New Superstar Toward Green and Stable Optoelectronic Applications. *Nano-Micro Lett.* **2019**, *11* (1), 16. https://doi.org/10.1007/s40820-019-0244-6.

(10) Fu, H. Review of Lead-Free Halide Perovskites as Light-Absorbers for Photovoltaic Applications: From Materials to Solar Cells. *Sol. Energy Mater. Sol. Cells* **2019**, *193*, 107–132. https://doi.org/10.1016/j.solmat.2018.12.038.

(11) Deng, Z.; Wei, F.; Sun, S.; Kieslich, G.; Cheetham, A. K.; Bristowe, P. D. Exploring the Properties of Lead-Free Hybrid Double Perovskites Using a Combined Computational-Experimental Approach. *J. Mater. Chem. A* **2016**, *4* (31), 12025–12029. https://doi.org/10.1039/C6TA05817E.

(12) Volonakis, G.; Filip, M. R.; Haghighirad, A. A.; Sakai, N.; Wenger, B.; Snaith, H. J.; Giustino, F. Lead-Free Halide Double Perovskites via Heterovalent Substitution of Noble Metals. *J. Phys. Chem. Lett.* **2016**, *7* (7), 1254–1259. https://doi.org/10.1021/acs.jpclett.6b00376.

(13) Slavney, A. H.; Hu, T.; Lindenberg, A. M.; Karunadasa, H. I. A Bismuth-Halide Double Perovskite with Long Carrier Recombination Lifetime for Photovoltaic Applications. *J. Am. Chem. Soc.* **2016**, *138* (7), 2138–2141. https://doi.org/10.1021/jacs.5b13294.

(14) Filip, M. R.; Hillman, S.; Haghighirad, A. A.; Snaith, H. J.; Giustino, F. Band Gaps of the Lead-Free Halide Double Perovskites Cs 2 BiAgCl 6 and Cs 2 BiAgBr 6 from Theory and Experiment. *J. Phys. Chem. Lett.* **2016**, *7* (13), 2579–2585. https://doi.org/10.1021/acs.jpclett.6b01041.

(15) McClure, E. T.; Ball, M. R.; Windl, W.; Woodward, P. M. Cs 2 AgBiX 6 (X = Br, Cl): New Visible Light Absorbing, Lead-Free Halide Perovskite Semiconductors. *Chem. Mater.* **2016**, *28* (5), 1348–1354. https://doi.org/10.1021/acs.chemmater.5b04231.

(16) Volonakis, G.; Filip, M. R.; Haghighirad, A. A.; Sakai, N.; Wenger, B.; Snaith, H. J.; Giustino, F. Lead-Free Halide Double Perovskites via Heterovalent Substitution of Noble Metals. *J. Phys. Chem. Lett.* **2016**, *7* (7), 1254–1259. https://doi.org/10.1021/acs.jpclett.6b00376.

(17) Volonakis, G.; Haghighirad, A. A.; Milot, R. L.; Sio, W. H.; Filip, M. R.; Wenger, B.; Johnston, M. B.; Herz, L. M.; Snaith, H. J.; Giustino, F. Cs 2 InAgCl 6 : A New Lead-Free Halide Double Perovskite with Direct Band Gap. *J. Phys. Chem. Lett.* **2017**, *8* (4), 772–778. https://doi.org/10.1021/acs.jpclett.6b02682.

(18) Luo, J.; Wang, X.; Li, S.; Liu, J.; Guo, Y.; Niu, G.; Yao, L.; Fu, Y.; Gao, L.; Dong, Q.;

Zhao, C.; Leng, M.; Ma, F.; Liang, W.; Wang, L.; Jin, S.; Han, J.; Zhang, L.; Etheridge, J.; Wang, J.; Yan, Y.; Sargent, E. H.; Tang, J. Efficient and Stable Emission of Warm-White Light from Lead-Free Halide Double Perovskites. *Nature* **2018**, *563* (7732), 541–545. https://doi.org/10.1038/s41586-018-0691-0.

(19) Lindquist, K. P.; Mack, S. A.; Slavney, A. H.; Leppert, L.; Gold-Parker, A.; Stebbins, J. F.; Salleo, A.; Toney, M. F.; Neaton, J. B.; Karunadasa, H. I. Tuning the Bandgap of Cs 2 AgBiBr 6 through Dilute Tin Alloying. *Chem. Sci.* **2019**, *10* (45), 10620–10628. https://doi.org/10.1039/C9SC02581B.

(20) Wu, C.; Du, B.; Luo, W.; Liu, Y.; Li, T.; Wang, D.; Guo, X.; Ting, H.; Fang, Z.; Wang, S.; Chen, Z.; Chen, Y.; Xiao, L. Highly Efficient and Stable Self-Powered Ultraviolet and Deep-Blue Photodetector Based on Cs 2 AgBiBr 6 /SnO 2 Heterojunction. *Adv. Opt. Mater.* **2018**, *6* (22), 1800811. https://doi.org/10.1002/adom.201800811.

(21) Gao, W.; Ran, C.; Xi, J.; Jiao, B.; Zhang, W.; Wu, M.; Hou, X.; Wu, Z. High-Quality Cs 2 AgBiBr 6 Double Perovskite Film for Lead-Free Inverted Planar Heterojunction Solar Cells with 2.2 % Efficiency. *ChemPhysChem* **2018**, *19* (14), 1696–1700. https://doi.org/10.1002/cphc.201800346.

(22) Pan, W.; Wu, H.; Luo, J.; Deng, Z.; Ge, C.; Chen, C.; Jiang, X.; Yin, W.-J.; Niu, G.; Zhu, L.; Yin, L.; Zhou, Y.; Xie, Q.; Ke, X.; Sui, M.; Tang, J. Cs2AgBiBr6 Single-Crystal X-Ray Detectors with a Low Detection Limit. *Nat. Photonics* **2017**, *11*

(11), 726–732. https://doi.org/10.1038/s41566-017-0012-4.

(23) Hoye, R. L. Z.; Eyre, L.; Wei, F.; Brivio, F.; Sadhanala, A.; Sun, S.; Li, W.; Zhang, K. H. L.; MacManus-Driscoll, J. L.; Bristowe, P. D.; Friend, R. H.; Cheetham, A. K.; Deschler, F. Fundamental Carrier Lifetime Exceeding 1 Ms in Cs 2 AgBiBr 6 Double Perovskite. *Adv. Mater. Interfaces* **2018**, *5* (15), 1800464. https://doi.org/10.1002/admi.201800464.

(24) Igbari, F.; Wang, R.; Wang, Z.-K.; Ma, X.-J.; Wang, Q.; Wang, K.-L.; Zhang, Y.; Liao, L.-S.; Yang, Y. Composition Stoichiometry of Cs 2 AgBiBr 6 Films for Highly Efficient Lead-Free Perovskite Solar Cells. *Nano Lett.* **2019**, *19* (3), 2066–2073. https://doi.org/10.1021/acs.nanolett.9b00238.

(25) Nayak, P. K.; Mahesh, S.; Snaith, H. J.; Cahen, D. Photovoltaic Solar Cell Technologies: Analysing the State of the Art. *Nat. Rev. Mater.* **2019**, *4* (4), 269–285. https://doi.org/10.1038/s41578-019-0097-0.

(26) Bartesaghi, D.; Slavney, A. H.; Gélvez-Rueda, M. C.; Connor, B. A.; Grozema, F. C.; Karunadasa, H. I.; Savenije, T. J. Charge Carrier Dynamics in Cs 2 AgBiBr 6 Double Perovskite. *J. Phys. Chem. C* **2018**, *122* (9), 4809–4816. https://doi.org/10.1021/acs.jpcc.8b00572.

(27) Hutter, E. M.; Gélvez-Rueda, M. C.; Bartesaghi, D.; Grozema, F. C.; Savenije, T. J. Band-Like Charge Transport in Cs 2 AgBiBr 6 and Mixed Antimony–Bismuth Cs 2 AgBi 1– x Sb x Br 6 Halide Double Perovskites. *ACS Omega* **2018**, *3* (9), 11655–11662. https://doi.org/10.1021/acsomega.8b01705.

(28) Dang, Y.; Tong, G.; Song, W.; Liu, Z.; Qiu, L.; Ono, L. K.; Qi, Y. Interface Engineering Strategies towards Cs 2 AgBiBr 6 Single-Crystalline Photodetectors with Good Ohmic Contact Behaviours. *J. Mater. Chem. C* **2020**, *8* (1), 276–284. https://doi.org/10.1039/C9TC04780H.

(29) Gray, M. B.; McClure, E. T.; Woodward, P. M. Cs 2 AgBiBr 6−x Cl x Solid Solutions – Band Gap Engineering with Halide Double Perovskites. *J. Mater. Chem. C* **2019**, *7* (31), 9686–9689. https://doi.org/10.1039/C9TC02674F.

(30) Schmitz, A.; Schaberg, L. L.; Sirotinskaya, S.; Pantaler, M.; Lupascu, D. C.; Benson, N.; Bacher, G. Fine Structure of the Optical Absorption Resonance in Cs 2 AgBiBr 6 Double Perovskite Thin Films. *ACS Energy Lett.* **2020**, *5* (2), 559–565. https://doi.org/10.1021/acsenergylett.9b02781.

(31) Bekenstein, Y.; Dahl, J. C.; Huang, J.; Osowiecki, W. T.; Swabeck, J. K.; Chan, E. M.; Yang, P.; Alivisatos, A. P. The Making and Breaking of Lead-Free Double Perovskite Nanocrystals of Cesium Silver–Bismuth Halide Compositions. *Nano Lett.* **2018**, *18* (6), 3502–3508. https://doi.org/10.1021/acs.nanolett.8b00560.

(32) Oldenburg, K.; Vogler, A. Electronic Spectra and Photochemistry of Tin(II), Lead(II), Antimony(III), and Bismuth(III) Bromide Complexes in Solution. *Zeitschrift fur Naturforsch. - Sect. B J. Chem. Sci.* **1993**. https://doi.org/10.1515/znb-1993-1109.

(33) Smith, M. D.; Karunadasa, H. I. White-Light Emission from Layered Halide

Perovskites. *Acc. Chem. Res.* **2018**, *51* (3), 619–627. https://doi.org/10.1021/acs.accounts.7b00433.

(34) McCall, K. M.; Stoumpos, C. C.; Kostina, S. S.; Kanatzidis, M. G.; Wessels, B. W. Strong Electron–Phonon Coupling and Self-Trapped Excitons in the Defect Halide Perovskites A 3 M 2 I 9 (A = Cs, Rb; M = Bi, Sb). *Chem. Mater.* **2017**, *29* (9), 4129–4145. https://doi.org/10.1021/acs.chemmater.7b01184.

(35) Steele, J. A.; Puech, P.; Keshavarz, M.; Yang, R.; Banerjee, S.; Debroye, E.; Kim, C. W.; Yuan, H.; Heo, N. H.; Vanacken, J.; Walsh, A.; Hofkens, J.; Roeffaers, M. B. J. Giant Electron–Phonon Coupling and Deep Conduction Band Resonance in Metal Halide Double Perovskite. *ACS Nano* **2018**, *12* (8), 8081–8090. https://doi.org/10.1021/acsnano.8b02936.

(36) Ning, W.; Wang, F.; Wu, B.; Lu, J.; Yan, Z.; Liu, X.; Tao, Y.; Liu, J.-M.; Huang, W.; Fahlman, M.; Hultman, L.; Sum, T. C.; Gao, F. Long Electron-Hole Diffusion Length in High-Quality Lead-Free Double Perovskite Films. *Adv. Mater.* **2018**, *30* (20), 1706246. https://doi.org/10.1002/adma.201706246.

(37) Wang, M.; Zeng, P.; Bai, S.; Gu, J.; Li, F.; Yang, Z.; Liu, M. High-Quality Sequential-Vapor-Deposited Cs 2 AgBiBr 6 Thin Films for Lead-Free Perovskite Solar Cells. *Sol. RRL* **2018**, *2* (12), 1800217. https://doi.org/10.1002/solr.201800217.

(38) Shockley, W.; Queisser, H. J. Detailed Balance Limit of Efficiency of P-n Junction Solar Cells. *J. Appl. Phys.* **1961**, *32* (3), 510–519.

https://doi.org/10.1063/1.1736034.

(39) Kirchartz, T.; Rau, U. Detailed Balance and Reciprocity in Solar Cells. *Phys. Status Solidi Appl. Mater. Sci.* **2008**, *205* (12), 2737–2751. https://doi.org/10.1002/pssa.200880458.

(40) Liu, Z.; Krückemeier, L.; Krogmeier, B.; Klingebiel, B.; Márquez, J. A.; Levcenko, S.; Öz, S.; Mathur, S.; Rau, U.; Unold, T.; Kirchartz, T. Open-Circuit Voltages Exceeding 1.26 v in Planar Methylammonium Lead Iodide Perovskite Solar Cells. *ACS Energy Lett.* **2019**, *4* (1), 110–117. https://doi.org/10.1021/acsenergylett.8b01906.

(41) Mahesh, S.; Ball, J. M.; Oliver, R. D. J.; McMeekin, D. P.; Nayak, P.; Johnston, M. B.; Snaith, H. Revealing the Origin of Voltage Loss in Mixed-Halide Perovskite Solar Cells. *Energy Environ. Sci.* **2019**, *50* (10), 675. https://doi.org/10.1039/C9EE02162K.

(42) Wehrenfennig, C.; Liu, M.; Snaith, H. J.; Johnston, M. B.; Herz, L. M. Charge-Carrier Dynamics in Vapour-Deposited Films of the Organolead Halide Perovskite CH 3 NH 3 PbI 3−x Cl X. *Energy Environ. Sci.* **2014**, *7* (7), 2269–2275. https://doi.org/10.1039/C4EE01358A.

(43) Johnston, M. B.; Herz, L. M. Hybrid Perovskites for Photovoltaics: Charge-Carrier Recombination, Diffusion, and Radiative Efficiencies. *Acc. Chem. Res.* **2016**, *49* (1), 146–154. https://doi.org/10.1021/acs.accounts.5b00411.

(44) Kentsch, R.; Scholz, M.; Horn, J.; Schlettwein, D.; Oum, K.; Lenzer, T. Exciton

Dynamics and Electron–Phonon Coupling Affect the Photovoltaic Performance of the Cs 2 AgBiBr 6 Double Perovskite. *J. Phys. Chem. C* **2018**, *122* (45), 25940–25947. https://doi.org/10.1021/acs.jpcc.8b09911.

(45) Richter, J. M.; Abdi-Jalebi, M.; Sadhanala, A.; Tabachnyk, M.; Rivett, J. P. H.; Pazos-Outón, L. M.; Gödel, K. C.; Price, M.; Deschler, F.; Friend, R. H. Enhancing Photoluminescence Yields in Lead Halide Perovskites by Photon Recycling and Light Out-Coupling. *Nat. Commun.* **2016**, *7* (1), 13941. https://doi.org/10.1038/ncomms13941.

(46) Xiao, Z.; Meng, W.; Wang, J.; Yan, Y. Thermodynamic Stability and Defect Chemistry of Bismuth-Based Lead-Free Double Perovskites. *ChemSusChem* **2016**, *9* (18), 2628–2633. https://doi.org/10.1002/cssc.201600771.

(47) Zhang, Z.; Yang, G.; Zhou, C.; Chung, C.-C.; Hany, I. Optical and Electrical Properties of All-Inorganic Cs 2 AgBiBr 6 Double Perovskite Single Crystals. *RSC Adv.* **2019**, *9* (41), 23459–23464. https://doi.org/10.1039/C9RA04045E.

(48) Delor, M.; Slavney, A. H.; Wolf, N. R.; Filip, M. R.; Neaton, J. B.; Karunadasa, H. I.; Ginsberg, N. S. Carrier Diffusion Lengths Exceeding 1 Mm Despite Trap-Limited Transport in Halide Double Perovskites. *ACS Energy Lett.* **2020**, *5* (5), 1337–1345. https://doi.org/10.1021/acsenergylett.0c00414.

(49) Cavalcoli, D.; Cavallini, A. Surface Photovoltage Spectroscopy - Method and Applications. *Phys. status solidi* **2010**, *7* (5), 1293–1300. https://doi.org/10.1002/pssc.200983124.

7

Infrared Management in All-Perovskite Tandems

7.1 Overview

To move towards thermodynamically limiting efficiencies, tandem stacks have to simultaneously be electronically and optically optimised. While electronic optimisation to reduce open-circuit voltage and fill-factor loss has received much attention, optical optimisation is much neglected. While optimised optics are not crucial for single junction solar cells, the multitude of layers in tandems, coupled with the requirement of current matching, necessitates stringent control over cell optics. Here we use optical modelling to analyse for the first time, what is arguably the largest optical loss mechanism in all-perovskite tandems today: a large refractive index mismatch at the recombination layer. We quantify this loss and demonstrate that replacing ITO with an intermediate refractive index material,

such as Nb doped TiO_2, can significantly enhance light incoupling into the low bandgap cell, boosting the PCE by upto 1% absolute. We also show that, interestingly, index matching also has the unintended consequence of making cell performance less sensitive to thickness variation during manufacturing.

7.2 Introduction

All-perovskite tandems offer the possibility of solar cells with over 30% PCE[1], while simultaneously being compatible with low temperature processing, high throughput manufacturing, and lightweight and flexible substrates[2]. As has been explained in chapter 2, tandem cells can broadly be realised in two architectures: the 2-terminal and the 4-terminal. Despite the reduced engineering complexity of making 4-terminal tandems, the 2-terminal tandem is widely recognised to be the frontrunner for commercialisation, due to reduced balance of system costs and improved light in coupling.

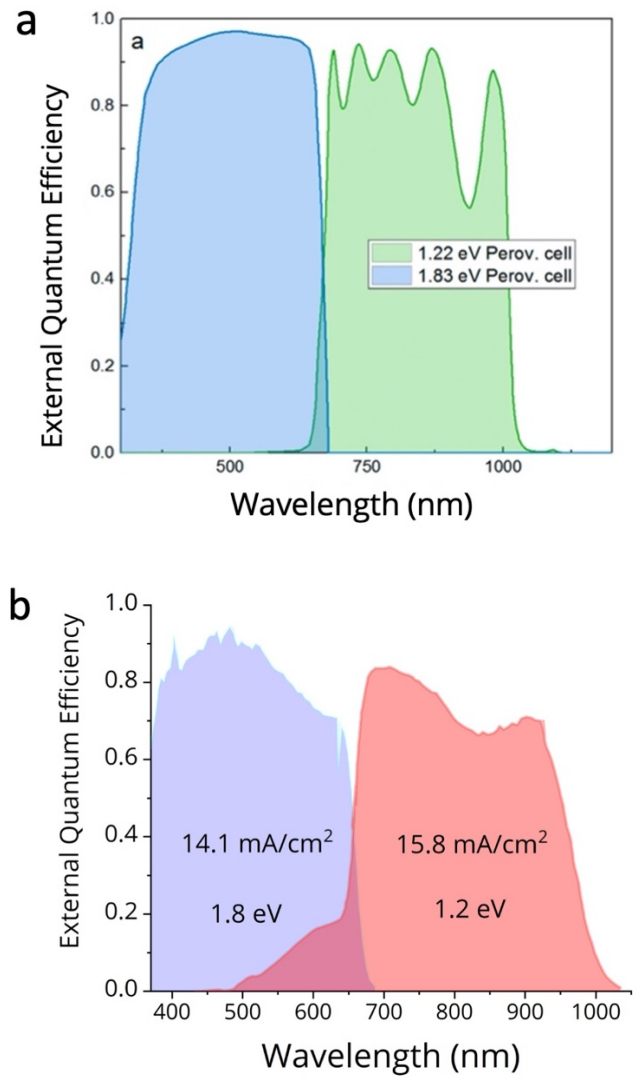

Figure 7.1 | All-perovskite tandems typically exhibit an EQE dip in the near infrared, arising from index mismatch. (**a**) EQE modelled for a thickness optimised all-perovskite tandem that uses 200 nm ITO as the recombination layer. Reproduced with permission from the work of Hörantner M.T. et al[1]. (**b**) EQE measured on a 1.2-1.8 eV all-perovskite tandem that uses 100 nm sputtered ITO as the recombination layer. Data extracted and replotted from the work of Eperon G.E. et al.[3]

In chapter 5, we have already explained that low-radiative efficiency— and not halide segregation—electronically limits these devices[4]. On the optical front too, tandems present significant challenges. For one, the PbSn perovskites do not exhibit absorption onsets as sharp as their neat Pb counterparts. Consequently, stunted optical response in the NIR limits photocurrent by as much as 3 mA/cm^2.

Tan H. and co-workers have shown that this limitation can be overcome with thick films (860 nm) that have large carrier diffusion lengths[5].

While single junction cells can usually be optimized by brute force experimentation, tandems, due to the multitude of layers, and the requirement of current matching, usually require complex optical modeling to maximize light absorption. Additionally, they are subject to current mismatch from the spatial and temporal variations in the solar resource. The presence of a large number of layers (>10) also causes current loss by means of parasitic absorption. For these reasons, multi-junctions demand a finer of control over optics than is necessary for single junctions. Here, we focus on an important optical loss mechanism that has so far escaped the attention of the community: reflective loss arising from refractive index mismatch at the recombination layer. This reflection has its signature in a significant dip in the NIR external quantum efficiency (figure 7.1). Even small current losses are significant in 2-terminal tandems, since current matching already results in a halving of the current. While this phenomenon has been studied for Si-perovskite tandems[6,7], the less-mature all-perovskite tandems have not yet received attention. Here we use optical modelling to show that replacing ITO with an intermediate index material, such as Nb doped TiO_2, can significantly enhance light in coupling into the rear cell, resulting in an absolute 1% boost in PCE. We also show that, unexpectedly, the performance of such index

matched cells is significantly less sensitive to the random variations in layer thicknesses during manufacturing.

7.3 Refractive Index Mismatch

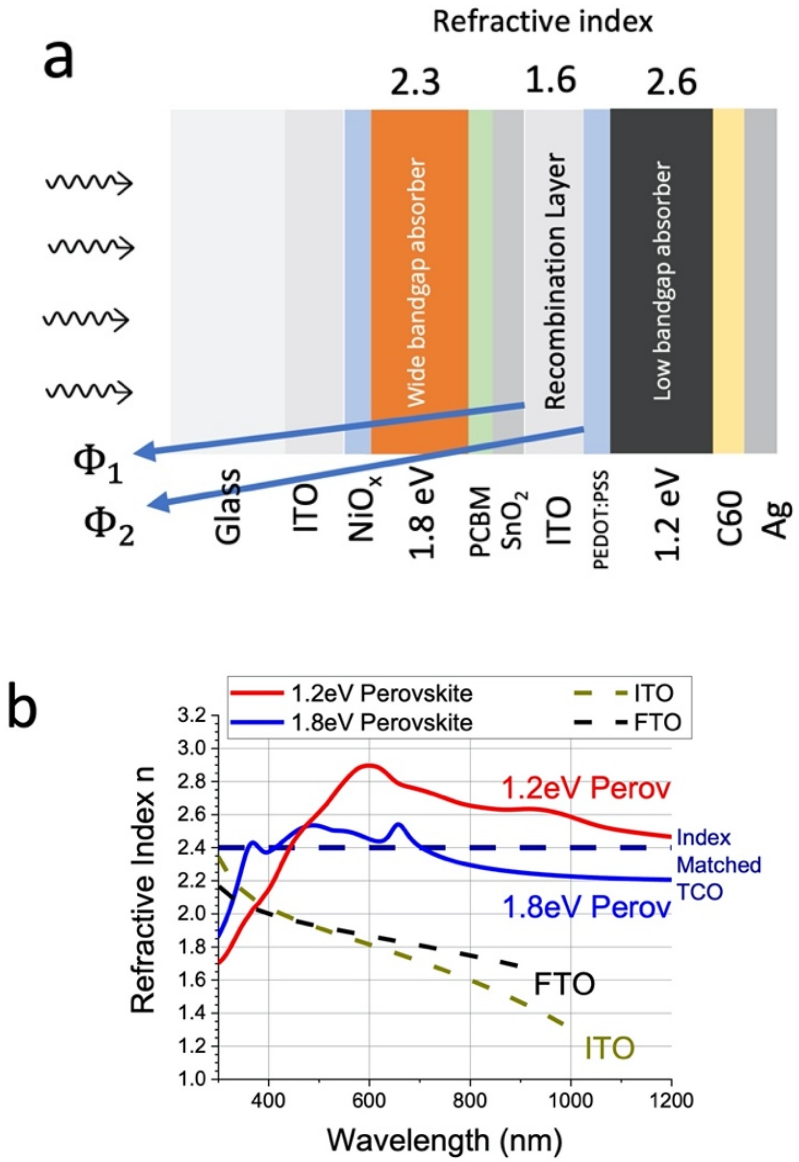

Figure 7.2 | (**a**) A typical all-perovskite tandem stack that exhibits a large refractive index mismatch at the recombination layer. All the calculations presented in this chapter are performed on this stack. Diagram not to scale. Arrows represent the reflection from the ITO interfaces. This particular stack is taken from the work of Eperon G.E.[8] (**b**) Refractive indices of

$FA_{0.83}Cs_{0.17}Pb_{0.5}Sn_{0.5}I_3$, and $FA_{0.83}Cs_{0.17}Pb(I_{0.6}Br_{0.4})_3$ (measured using ellipsometry), ITO[9] and FTO[10] (from literature). The large index mismatch is apparent.

It is well known empirically ("Moss Rule") that in semiconductors, refractive index n increases as bandgap E_g decreases[11]:

$$n^4 \propto \frac{1}{E_g} \qquad 7.1$$

Hence in a planar multi-junction cell, we can expect light to encounter sharp changes in refractive index as it successively moves through absorbers of varying bandgap. This index mismatch causes light to be reflected out of the stack, reducing the short-circuit current density. Every absorber in the stack, except one with the highest bandgap, is subject to this reflection loss.

So far, there have been two successful strategies for fabricating all-perovskite tandem cells. The first is physical vapor deposition (PVD) of the absorber perovskite, charge transport layers and the recombination layer[12]. Using this strategy, an extremely thin (5-20 nm) recombination layer can be deposited, making parasitic absorptions and reflections practically irrelevant. Another advantage of PVD is that it eliminates the issue of solvents damage during processing. PVD for perovskites PV is still nascent, however, and the best quality absorbers and transport layers to date are all solution processed. When solution processing is employed to make tandems, a thick metal oxide layer of indium tin oxide (ITO) is typically used as the recombination layer (see table 2.1 for a list). This has two functions: to act as a (weakly) conductive layer where charge can

recombine, and to act as a physical barrier to the solvent being used to process the overlying layers. This ITO layer, however, also induces a large refractive index mismatch with the adjacent perovskite layers. For instance, at 800 nm, light sees large refractive index changes as it moves from the 1.8 eV absorber (n=2.3) to the ITO (n=1.6) to the 1.2 eV absorber (n=2.6). This causes a significant fraction of the light to be reflected from both interfaces of the ITO, causing current loss in the low bandgap cell. The wide bandgap cell is unaffected. When the ITO layer is thin (< 20 nm), the optical impact is negligible. Horantner et al. suggest that reducing the thickness of the ITO layer to (near)-zero gives the best optical performance[1]. However, this is impractical as a thick solvent barrier is needed for the next perovskite layer to be processed. To a first approximation, we can estimate the ideal recombination layer refractive index n_0 using the standard equation for anti-reflective coatings:

$$n_0(800\,nm) = \sqrt{n_1 n_2} = \sqrt{2.3 \cdot 2.6} = 2.45 \qquad 7.2$$

For a more complete understanding that includes the spectral dependance of the refractive index, the optical effects of other layers and the impact of current mismatch, a full solar cell model is necessary.

7.4 Modelling the Impact of Index Mismatch

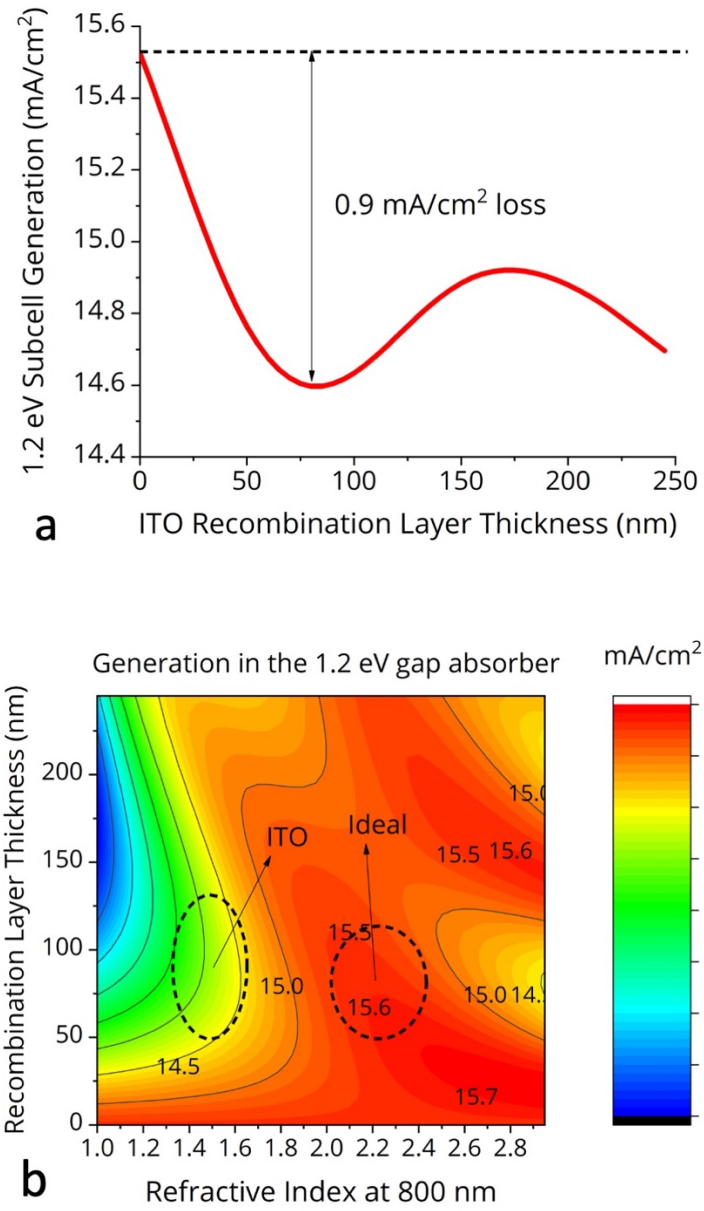

Figure 7.3 | (**a**) Variation in the generation of the PbSn based subcell as a function of the thickness of the ITO recombination layer. (**b**) Heat map of generation in the PbSn subcell as a function of recombination layer thickness.

We implemented a generalized transfer matrix based optical model[13], and a detailed-balance based device model[1,14] to model the impact of index-mismatch,

and estimate the efficiency boost arising from index-matching. The Transfer-Matrix method (TMM) is a recasting of Fresnel's equations to calculate electromagnetic wave propagation in any planar stratified medium, such as a solar cell stack. A brief description has been provided in chapter 3. TMM uses the optical constants and thicknesses of the layers to calculate the absorptance $A(\lambda)$, which is then treated as the EQE of the cell. We then used detailed balance (assuming the same state of the art $R_s, R_{sh}, n_{id}, EQE_{EL}$ as Horantner M. et al[1]) to calculate a JV curve, thus fully determining device performance (see chapter 3). All the modelling in this chapter is performed on a p-i-n tandem stack (figure 7.2a) based on the published work of Eperon G. et al[8]: Glass (2.2 mm)/ITO[9] (200 nm)/NiO_x (15 nm)/1.83 eV 1.83 eV FACs based mixed-halide perovskite /PCBM (10 nm)/SnO_2[15] (6 nm)/ITO[9]/PEDOT:PSS (20 nm)/1.22 eV FACs-based PbSn perovskite/C60[15] (40 nm)/Ag[16] (100 nm). The optical constants of the perovskites, PCBM, PEDOT:PSS were measured using ellipsometry; the data for the others is taken from the above cited literature.

To quantify the reflective loss arising from the index-mismatched ITO, we calculated the generation in the PbSn subcell as a function of ITO thickness (Fig 7.3a). The current exhibits the oscillatory behavior typical of interference: it is highest in the absence of the ITO, then drops by 0.9 mA/cm^2 to a trough as the thickness reaches 80 nm, and then partially recovers by 175 nm, only to drop again. Thus, the optimal thickness for an ITO interlayer falls around 150-200nm.

This is thicker than ideal from a manufacturing and processing perspective, due to the scarcity and cost of indium. The more practical thickness—60-100 nm falls exactly in the region that maximizes reflection. In short, the optics of ITO make it ill-suited to be a thick recombination layer.

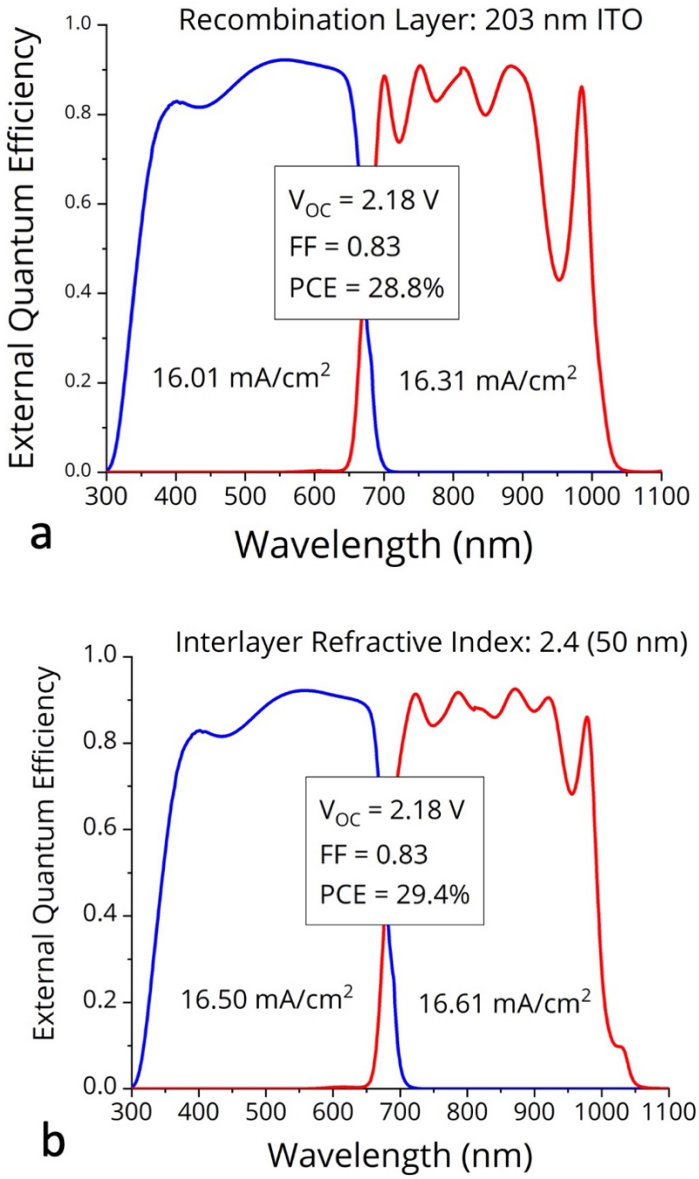

Figure 7.4 | When the recombination layer is index matched, the spectral response in the NIR improves significantly. (**a**) EQE and figures of merit calculated for a thickness optimized tandem with an ideal-thickness ITO recombination layer (203 nm). (**b**) EQE and figures of merit calculated for a tandem with a 50 nm thick idealized recombination layer of refractive index 2.4

(uniform across the spectrum). The recombination layer is assumed to have the same absorptance as ITO.

We have now established that ITO, optically, is not the optimal recombination layer candidate. What is optimal then? Since there is a range of desirable thicknesses (60-100 nm), there exists a range of refractive indices. In general, higher refractive indices are better, as they permit lower thicknesses, hence reducing parasitic absorption. The ideal interlayer has to minimize the total reflection over all wavelengths, while also taking the shape of the AM1.5 spectrum into account. To determine the range of ideal refractive indices, we calculated the bottom sub cell generation for a range of refractive indices and thicknesses (figure 7.3b). For simplicity, the refractive index was assumed to be constant across the spectrum, and the films were assumed to have the same extinction co-efficient as ITO. Our calculations (figure 7.3b) reveal that refractive index in range 2.0-2.5 (above 800 nm) maximises light in coupling, while simultaneously fulfilling the thickness requirement (60-100 nm). We calculated the gain in a thickness optimised, current matched device, revealing that substituting ITO with a 50 nm thick recombination layer of refractive index 2.4 results in a 0.8 mA/cm^2 boost in net photon absorption (figure 7.4). As the next section will show, a higher efficiency increase is obtained when the sub-cell bandgaps are also matched.

7.5 High Refractive Index Materials

Table 7.1 | Candidates for a high-refractive index recombination layer.

Material	Bandgap	Refractive Index (900 nm)
Nb: doped TiO_2[17]	3.07 eV	2.3
Ta doped TiO_2[18]	NA	NA
V doped TiO_2[18]	NA	NA
$SrTiO_3$[19–21]	3.25 eV	2.33
Cr_2O_3[22]	3.31 eV	2.5
$CuCrO_2$[22]	3.1	2.6
ZnS[23]	3.6 eV	2.30
ZrO_2[24]	>5 eV	2.12

As the previous section has shown, a recombination layer with a high-refractive index in the NIR ($n > 2.0$) is highly desirable for perovskite-perovskite tandems. Such a recombination layer would need to satisfy the following properties:

1. High refractive index ($n > 2.0$) in the range 650-1100 nm, i.e. where the low bandgap cell absorbs.

2. Low absorption co-efficient ($\alpha < 10^3 cm^{-1}$) in the same range. In other words, wide bandgap semiconductors ($E_g > 2.5$) are suitable.

3. Fairly low sheet resistance ($< 10\ k\Omega\ \mathrm{cm}$) to enable lossless recombination of electrons and holes.

In short, a class of materials that have requirements very similar to TCOs. The only difference being the resistivity, which can be several orders of magnitude higher as there is no long-range lateral conduction. Unfortunately, high-refractive index TCOs are rare due to the previously mentioned empirical observation ("Moss' rule"): high-bandgap semiconductors tend to have low refractive indices. However, some exceptional ceramics can be considered: TiO_2, $SrTiO_3$, $CuCrO_2$, ZnS, ZrO_2 (Table 7.1). Nitrides like GaN and AlN are also potential candidates. Of these materials, doped TiO_2 is the most promising high-index alternative to ITO and FTO. Specifically, when doped with Nb, TiO_2 has been shown to be electrically and optically similar to ITO[25–32]. Such high conductivities are only possible in the anatase phase, which needs high temperature annealing ($> 300\ °C$) to form. The low temperature processed rutile phase is 10^2-10^3 times less conductive[33]. However, this is perfectly acceptable for a recombination layer, since there is no long-range lateral conduction. In fact, low lateral conductivity is even advantageous since it minimises the risk of short-circuiting the device through the interlayer. Even a resistivity as high as $10\ k\Omega\ cm$ will only cause a negligible voltage drop of ~1 mV. Nb:TiO_2 films with a resistivity of $0.1\ \Omega\ cm$ have been achieved by room-temperature sputtering. Thus, as technology stands, Nb:TiO_2 is the most

promising candidate for realizing a high-refractive index recombination layer for all-perovskite tandems.

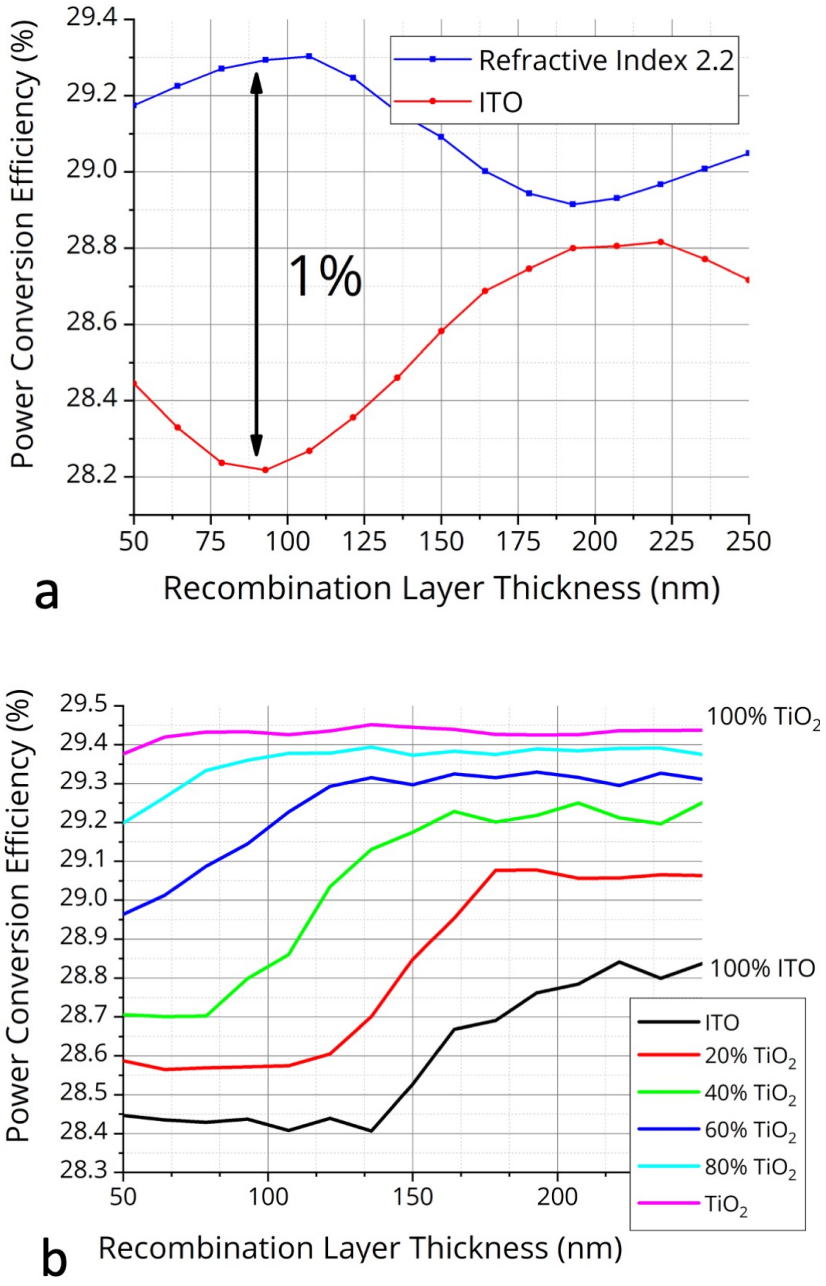

Figure 7.5 | (**a**) Power conversion efficiency as a function of thickness. Two materials are compared: ITO, and an idealized panchromatic $n = 2.2$ material with the same extinction co-efficient as ITO. The calculated efficiency has been obtained by optimizing the thickness and the top-cell bandgap. (**b**) Power conversion efficiency as a function of thickness for a number of Nb:TiO_2/ITO blend ratios. The calculated efficiency has been obtained by optimizing the thickness and the top-cell bandgap.

We modelled the performance of tandems that use Nb:TiO_2 as the recombination layer. As the optical constants of Nb:TiO_2 are still unreported, we make the fair assumption that they are identical to those of TiO_2[15] since the doping is small (<5%). In our previous assessment of the efficiency boost (figure 7.4), we only optimized the thicknesses of the absorber layers while modelling the tandem performance. However, there is yet another effect at work that needs to be considered. As bottom-cell in-coupling changes, the optimal bandgap for the top cell also varies. Since a higher-refractive index increases generation in the bottom cell, the top cell bandgap has to be slightly lowered for current matching. We include this effect by optimizing both the top-cell bandgap and the absorber thicknesses (figure 7.5a). With this effect included, we see that an idealized panchromatic $n = 2.2$ recombination layer gives an absolute efficiency boost of 1%, assuming that its extinction co-efficient is the same as that of ITO. This is a very significant improvement in a field where efficiencies now only move by decimal points. When the same assessment is made for Nb:TiO_2, a similar efficiency increase of over 1% absolute is seen (figure 7.5b). TiO_2 also offers the advantage of forming blends with ITO[34,35], where the high conductivity of ITO can potentially be combined with the superior optical properties of TiO_2. In principle, a small fraction of ITO should be sufficient as recombination layers do not need high conductivities.

7.6 Insensitivity to manufacturing variations

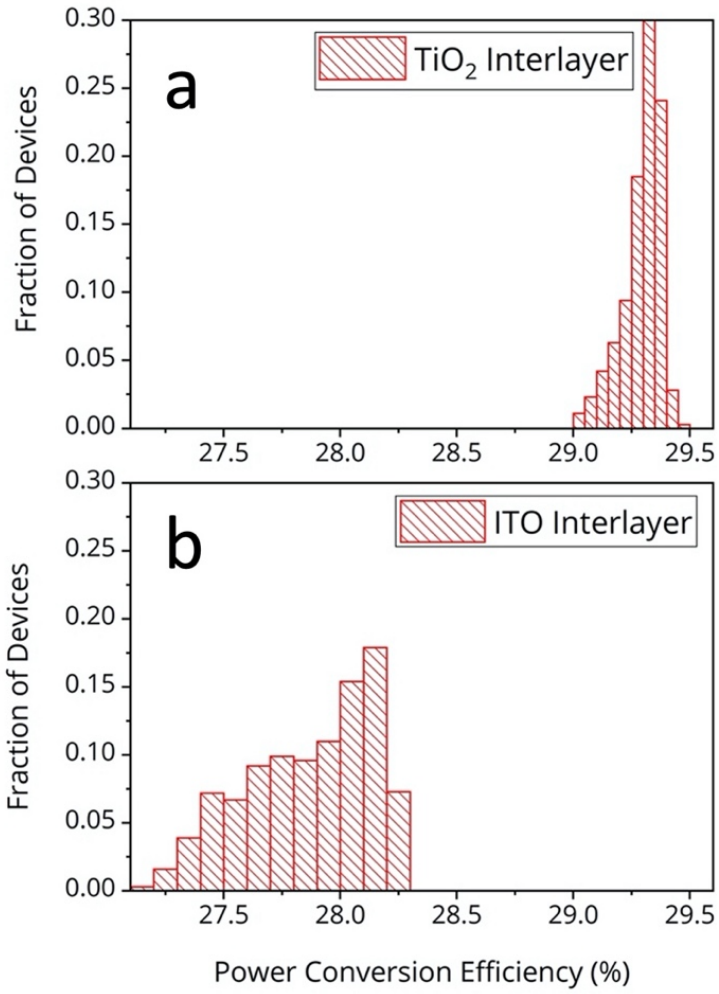

Figure 7.6 |Tandem PCE distribution obtained with 5% standard deviation in layer thicknesses (**a**) With TiO_2 as the recombination layer (**b**) With ITO as the recombination layer.

Tandem fabrication demands rigorous control over layer thicknesses. The large number of layers, combined with the requirement for current matching demands that optimum thicknesses be designed by simulation, preferably by calculating the annual energy yield[14], and preferably for the location under

consideration. In practice, this exact optimum cannot be achieved. Because of random variation in thickness during manufacturing, most real cells will sit displaced from the design efficiency. This can be an issue if the calculated optimum is “narrow”, i.e. the efficiency drops quickly with small changes in layer thicknesses. We desire a “shallow” optimum, where the efficiency is not sensitive to small thickness variations. We show that index-matched tandems are significantly less sensitive to such variation than mismatched cells. We simulated two batches of tandems, 1000 devices each, incorporating ITO and Nb:TiO_2 as the recombination layer respectively. The thicknesses of all the layers in the stack were distributed around the optimum with 5% standard deviation, a value in the same ballpark as the industry. The ITO-based tandem cells were designed for 28.3% efficiency, but the average over the 1000 cells is only 27.7%— a drop of 0.7% absolute. In contrast, index-matched cells with Nb:TiO_2 only drop by 0.3% absolute: from 29.5% to 29.2%. Thus, the effect of index-matching is more than just the previously calculated 1% absolute increase in PCE from increased in coupling — it is actually 1.5% in effect.

7.7 Conclusions

In summary, optical simulations of all-perovskite tandem cells indicate that refractive index mismatch at the ITO recombination layer results in a large reflective loss. Our simulations suggest that replacing the commonly used ITO

with a high refractive index alternative ($n\ (800\ nm) > 2.0$) can significantly reduce this loss and boost the PCE by over 1% absolute. We identify niobium doped TiO_2 as a promising material, since it has already been demonstrated to have suitable conductivity, transparency, and low temperature processability. We have also shown that the reduced reflective loss is concomitant with a decreased sensitivity to thickness variations during manufacturing, resulting, effectively, in a 1.5% absolute PCE boost.

7.8 References

(1) Hörantner, M. T.; Leijtens, T.; Ziffer, M. E.; Eperon, G. E.; Christoforo, M. G.; McGehee, M. D.; Snaith, H. J. The Potential of Multijunction Perovskite Solar Cells. *ACS Energy Lett.* **2017**, *2* (10), 2506–2513. https://doi.org/10.1021/acsenergylett.7b00647.

(2) Palmstrom, A. F.; Eperon, G. E.; Leijtens, T.; Prasanna, R.; Habisreutinger, S. N.; Nemeth, W.; Gaulding, E. A.; Dunfield, S. P.; Reese, M.; Nanayakkara, S.; Moot, T.; Werner, J.; Liu, J.; To, B.; Christensen, S. T.; McGehee, M. D.; van Hest, M. F. A. M.; Luther, J. M.; Berry, J. J.; Moore, D. T. Enabling Flexible All-Perovskite Tandem Solar Cells. *Joule* **2019**, *3* (9), 2193–2204. https://doi.org/10.1016/j.joule.2019.05.009.

(3) Eperon, G. E.; Leijtens, T.; Bush, K. A.; Prasanna, R.; Green, T.; Wang, J. T.-W.; McMeekin, D. P.; Volonakis, G.; Milot, R. L.; May, R.; Palmstrom, A.;

Slotcavage, D. J.; Belisle, R. A.; Patel, J. B.; Parrott, E. S.; Sutton, R. J.; Ma, W.; Moghadam, F.; Conings, B.; Babayigit, A.; Boyen, H.-G.; Bent, S.; Giustino, F.; Herz, L. M.; Johnston, M. B.; McGehee, M. D.; Snaith, H. J. Perovskite-Perovskite Tandem Photovoltaics with Optimized Band Gaps. *Science (80-.).* **2016**, *354* (6314), 861–865. https://doi.org/10.1126/science.aaf9717.

(4) Mahesh, S.; Ball, J. M.; Oliver, R. D. J.; McMeekin, D. P.; Nayak, P.; Johnston, M. B.; Snaith, H. Revealing the Origin of Voltage Loss in Mixed-Halide Perovskite Solar Cells. *Energy Environ. Sci.* **2019**, *50* (10), 675. https://doi.org/10.1039/C9EE02162K.

(5) Lin, R.; Xiao, K.; Qin, Z.; Han, Q.; Zhang, C.; Wei, M.; Saidaminov, M. I.; Gao, Y.; Xu, J.; Xiao, M.; Li, A.; Zhu, J.; Sargent, E. H.; Tan, H. Monolithic All-Perovskite Tandem Solar Cells with 24.8% Efficiency Exploiting Comproportionation to Suppress Sn(Ii) Oxidation in Precursor Ink. *Nat. Energy* **2019**, *4* (10), 864–873. https://doi.org/10.1038/s41560-019-0466-3.

(6) Mazzarella, L.; Lin, Y.; Kirner, S.; Morales-Vilches, A. B.; Korte, L.; Albrecht, S.; Crossland, E.; Stannowski, B.; Case, C.; Snaith, H. J.; Schlatmann, R. Infrared Light Management Using a Nanocrystalline Silicon Oxide Interlayer in Monolithic Perovskite/Silicon Heterojunction Tandem Solar Cells with Efficiency above 25%. *Adv. Energy Mater.* **2019**, *9* (14), 1803241. https://doi.org/10.1002/aenm.201803241.

(7) Lin, Y.-H.; Sakai, N.; Da, P.; Wu, J.; Sansom, H. C.; Ramadan, A. J.; Mahesh, S.;

Liu, J.; Oliver, R. D. J.; Lim, J.; Aspitarte, L.; Sharma, K.; Madhu, P. K.; Morales-Vilches, A. B.; Nayak, P. K.; Bai, S.; Gao, F.; Grovenor, C. R. M.; Johnston, M. B.; Labram, J. G.; Durrant, J. R.; Ball, J. M.; Wenger, B.; Stannowski, B.; Snaith, H. J. A Piperidinium Salt Stabilizes Efficient Metal-Halide Perovskite Solar Cells. *Science (80-.).* **2020**, *369* (6499), 96–102. https://doi.org/10.1126/science.aba1628.

(8) Eperon, G. E.; Leijtens, T.; Bush, K. A.; Green, T.; Wang, J. T.-W.; McMeekin, D. P.; Volonakis, G.; Milot, R. L.; Slotcavage, D. J.; Belisle, R.; Patel, J. B.; Parrott, E. S.; Sutton, R. J.; Ma, W.; Moghadam, F.; Conings, B.; Babayigit, A.; Boyen, H.; Giustino, F.; Herz, L. M.; Johnston, M. B.; McGehee, M. D.; Snaith, H. J. Perovskite-Perovskite Tandem Photovoltaics with Ideal Bandgaps. *ArXiv* **2016**, *9717* (October), 1–10. https://doi.org/10.1126/science.aaf9717.

(9) König, T. A. F.; Ledin, P. A.; Kerszulis, J.; Mahmoud, M. A.; El-Sayed, M. A.; Reynolds, J. R.; Tsukruk, V. V. Electrically Tunable Plasmonic Behavior of Nanocube–Polymer Nanomaterials Induced by a Redox-Active Electrochromic Polymer. *ACS Nano* **2014**, *8* (6), 6182–6192. https://doi.org/10.1021/nn501601e.

(10) Ball, J. M.; Stranks, S. D.; Hörantner, M. T.; Hüttner, S.; Zhang, W.; Crossland, E. J. W.; Ramirez, I.; Riede, M.; Johnston, M. B.; Friend, R. H.; Snaith, H. J. Optical Properties and Limiting Photocurrent of Thin-Film Perovskite Solar Cells. *Energy Environ. Sci.* **2015**, *8* (2), 602–609.

https://doi.org/10.1039/C4EE03224A.

(11) Hervé, P.; Vandamme, L. K. J. General Relation between Refractive Index and Energy Gap in Semiconductors. *Infrared Phys. Technol.* **1994**, *35* (4), 609–615. https://doi.org/10.1016/1350-4495(94)90026-4.

(12) Ávila, J.; Momblona, C.; Boix, P. P.; Sessolo, M.; Anaya, M.; Lozano, G.; Vandewal, K.; Míguez, H.; Bolink, H. J. High Voltage Vacuum-Deposited CH3NH3PbI3-CH3NH3PbI3 Tandem Solar Cells. *Energy Environ. Sci.* **2018**, *11* (11), 0–8. https://doi.org/10.1039/C8EE01936C.

(13) Centurioni, E. Generalized Matrix Method for Calculation of Internal Light Energy Flux in Mixed Coherent and Incoherent Multilayers. *Appl. Opt.* **2005**, *44* (35), 7532. https://doi.org/10.1364/AO.44.007532.

(14) Hörantner, M. T.; Snaith, H. J. Predicting and Optimising the Energy Yield of Perovskite-on-Silicon Tandem Solar Cells under Real World Conditions. *Energy Environ. Sci.* **2017**, *10* (9), 1983–1993. https://doi.org/10.1039/c7ee01232b.

(15) Ren, S. L.; Wang, Y.; Rao, A. M.; McRae, E.; Holden, J. M.; Hager, T.; Wang, K.; Lee, W.; Ni, H. F.; Selegue, J.; Eklund, P. C. Ellipsometric Determination of the Optical Constants of C 60 (Buckminsterfullerene) Films. *Appl. Phys. Lett.* **1991**, *59* (21), 2678–2680. https://doi.org/10.1063/1.105907.

(16) Johnson, P. B.; Christy, R. W. Optical Constants of the Noble Metals. *Phys. Rev. B* **1972**, *6* (12), 4370–4379. https://doi.org/10.1103/PhysRevB.6.4370.

(17) Lee, C.-C.; Li, M.-C.; Chen, S.-H.; Kuo, C.-C. Transparent Conductive Distributed Bragg Reflectors Composed of High and Low Refractive Index Transparent Conductive Films. *Jpn. J. Appl. Phys.* **2012**, *51*, 052602. https://doi.org/10.1143/JJAP.51.052602.

(18) Dixon, S. C.; Scanlon, D. O.; Carmalt, C. J.; Parkin, I. P. N-Type Doped Transparent Conducting Binary Oxides: An Overview. *J. Mater. Chem. C* **2016**, *4* (29), 6946–6961. https://doi.org/10.1039/C6TC01881E.

(19) Refractive Index of SrTiO3 https://refractiveindex.info/?shelf=main&book=SrTiO3&page=Dodge (accessed Nov 5, 2020).

(20) Cho, J. H.; Cho, H. J. Optical Transparency of Metallic La0.5Sr0.5TiO3+δ Thin Films. *Appl. Phys. Lett.* **2001**, *79* (10), 1426–1428. https://doi.org/10.1063/1.1402961.

(21) Guo, H.; Liu, L.; Fei, Y.; Xiang, W.; Lü, H.; Dai, S.; Zhou, Y.; Chen, Z. Optical Properties of p -Type In-Doped SrTiO3 Thin Films. *J. Appl. Phys.* **2003**, *94* (7), 4558–4562. https://doi.org/10.1063/1.1606510.

(22) Farrell, L.; Norton, E.; Smith, C. M.; Caffrey, D.; Shvets, I. V.; Fleischer, K. Synthesis of Nanocrystalline Cu Deficient CuCrO 2 – a High Figure of Merit p-Type Transparent Semiconductor. *J. Mater. Chem. C* **2016**, *4* (1), 126–134. https://doi.org/10.1039/C5TC03161C.

(23) Refractive Index of ZnS

https://refractiveindex.info/?shelf=main&book=ZnS&page=Querry.

(24) Refractive Index of ZrO2 https://refractiveindex.info/?shelf=main&book=ZrO2&page=Wood.

(25) Mandal, D.; Goswami, P. N.; Rath, A. K. Colossal Photo-Conductive Gain in Low Temperature Processed TiO_2 Films and Their Application in Quantum Dot Solar Cells. *Appl. Phys. Lett.* **2017**, *110* (12), 123902. https://doi.org/10.1063/1.4978766.

(26) Ben Jemaa, I.; Chaabouni, F.; Presmanes, L.; Thimont, Y.; Abaab, M.; Barnabe, A.; Tailhades, P. Structural, Optical and Electrical Investigations on Nb Doped TiO2radio-Frequency Sputtered Thin Films from a Powder Target. *J. Mater. Sci. Mater. Electron.* **2016**, *27* (12), 13242–13248. https://doi.org/10.1007/s10854-016-5471-8.

(27) Sato, Y.; Akizuki, H.; Kamiyama, T.; Shigesato, Y. Transparent Conductive Nb-Doped TiO2films Deposited by Direct-Current Magnetron Sputtering Using a TiO2 - Xtarget. *Thin Solid Films* **2008**, *516* (17), 5758–5762. https://doi.org/10.1016/j.tsf.2007.10.047.

(28) Dhar, A.; Alford, T. L. High Quality Transparent TiO2/Ag/TiO2 Composite Electrode Films Deposited on Flexible Substrate at Room Temperature by Sputtering. *APL Mater.* **2013**, *1* (1). https://doi.org/10.1063/1.4808438.

(29) Sato, Y.; Sanno, Y.; Tasaki, C.; Oka, N.; Kamiyama, T.; Shigesato, Y. Electrical and Optical Properties of Nb-Doped TiO2 Films Deposited by Dc Magnetron

Sputtering Using Slightly Reduced Nb-Doped TiO2−x Ceramic Targets. *J. Vac. Sci. Technol. A Vacuum, Surfaces, Film.* **2010**, *28* (4), 851–855. https://doi.org/10.1116/1.3358153.

(30) Safeen, K.; Micheli, V.; Bartali, R.; Gottardi, G.; Safeen, A.; Ullah, H.; Laidani, N. Synthesis of Conductive and Transparent Nb-Doped TiO2 Films: Role of the Target Material and Sputtering Gas Composition. *Mater. Sci. Semicond. Process.* **2017**, *66* (August), 74–80. https://doi.org/10.1016/j.mssp.2017.04.012.

(31) Ittkau, K. B.; Irchartz, T. K.; Au, U. R. Optical Design of Spectrally Selective Interlayers for Perovskite / Silicon Heterojunction Tandem Solar Cells. **2018**, *26* (18), 750–760. https://doi.org/10.1364/OE.26.00A750.

(32) Gillispie, M. A.; Van Hest, M. F. A. M.; Dabney, M. S.; Perkins, J. D.; Ginley, D. S. Rf Magnetron Sputter Deposition of Transparent Conducting Nb-Doped Ti O2 Films on SrTi O3. *J. Appl. Phys.* **2007**, *101* (3). https://doi.org/10.1063/1.2434005.

(33) Sahasrabudhe, G.; Krizan, J.; Bergman, S. L.; Cava, R. J.; Schwartz, J. Million-Fold Increase of the Conductivity in TiO 2 Rutile through 3% Niobium Incorporation. *Chem. Mater.* **2016**, *28* (11), 3630–3633. https://doi.org/10.1021/acs.chemmater.6b02031.

(34) Lim, J.-W.; Na, S.-I.; Kim, H.-K. Anatase TiO2 and ITO Co-Sputtered Films for an Indium-Saving Multicomponent Electrode in Organic Solar Cells. *Sol.*

Energy Mater. Sol. Cells **2012**, *98*, 409–416. https://doi.org/10.1016/j.solmat.2011.11.054.

(35) Lee, K.-S.; Lim, J.-W.; Kim, H.-K.; Alford, T. L.; Jabbour, G. E. Transparent Conductive Electrodes of Mixed TiO 2−x –Indium Tin Oxide for Organic Photovoltaics. *Appl. Phys. Lett.* **2012**, *100* (21), 213302. https://doi.org/10.1063/1.4707381.

8

Conclusions

The central aim of this thesis has been to understand some challenges peculiar to the creation of high efficiency (>30% PCE) perovskite-based multi-junction cells. Chapter 2 has laid out a detailed review of the state of the field, and the barriers to be overcome. Three chapters of this thesis have dealt with three important issues: a) development of high efficiency mixed-halide perovskites, b) development of new wide bandgap absorbers (in this case $Cs_2AgBiBr_6$) and c) recombination layer development. We now put our results in context and make some comments on the way forward.

Since its first report in 2015, halide segregation has widely been believed to be responsible for the poor open-circuit voltages obtained from bromide-rich mixed-halide perovskite solar cells. In chapter 5, we quantified, for the first time, the impact of halide-segregation upon the V_{OC} of mixed-halide solar cells. Our results unambiguously reveal that the effect of halide-segregation is, in fact, dwarfed by non-radiative recombination by four to five times! Contrary to popular belief (and research effort by the community), the performance of mixed-halide cells is primarily limited—not by halide segregation— but by the poor radiative

efficiency. Our work highlights the means to solve this issue: focus on reducing the initial defect density, and neglect halide segregation as an issue until improved radiative efficiency has been achieved. The goal should be to bring the radiative efficiency of the 1.8 eV gap perovskite on par with the ~1.6 eV gap perovskite (~10%). Understanding the solution chemistry of mixed-halide solutions is likely an important step towards increasing bulk radiative efficiency. Furthermore, it is imperative to develop transport layers tailored for the energetics of wide bandgap perovskites. As the PolyTPD and PEDOT:PSS heterojunctions are significantly quenching, the development of new hole transport layers with deep HOMO levels should also take priority.

In chapter 6, we explored the origin of photocurrent loss in the most promising double perovskite $Cs_2AgBiBr_6$. While the bandgap of this particular material is too large to be useful for PV, it serves as a convenient test bed for understanding the properties of a family that is likely to contain many more PV absorbers. Our investigations reveal that transport is strongly electron diffusion limited (d_e~30 nm) in this material. This is consistent with the large trap electron densities revealed by PDS and surface photovoltage measurements. We believe that this abundance of electron traps is the most significant materials issue limiting the performance of these cells, simultaneously affecting the $V_{OC,}$ and the J_{SC}. The origin of these traps should be investigated, both experimentally and

theoretically. Effort has to be invested on synthesising analogs with direct bandgaps in the range 1.7-2.0 eV.

While small libraries have been written on the matter of electronic loss mechanisms in perovskites, optical loss has not received as much attention. The reason for this is simple— there is not much complexity in the optics of single junction solar cells. Tandems, however, necessitate stringent control over cell optics. In chapter 7, we used optical modelling to quantify the largest optical loss in all-perovskite tandem cells: reflective loss from a refractive index mismatched recombination layer. We show that a thick ITO recombination layer induces severe index mismatch, which shows up as diminished spectral response in the NIR. Our work shows that the optically ideal recombination layer has a refractive index in the range 2.0-2.4 (at 800 nm). Our modelling indicates that such interlayers can boost tandem PCE by over one percentage point. We suggest a number of candidate materials, Nb doped TiO_2 being the most promising. Our work also shows that, surprisingly, the performance of index-matched cells is less sensitive to variations in layer thicknesses during manufacturing. Future work includes the experimental realisation of such an interlayer, and integration into a tandem solar cell.